NASA Contractor Report 185509

Implementing the Simple Biosphere Model (SiB) in a General Circulation Model: Methodologies and Results

N. Sato
Japanese Meteorological Agency
Tokyo, Japan

P. J. Sellers
University of Maryland
College Park, Maryland

D. A. Randall
Colorado State University
Fort Collins, Colorado

E. K. Schneider, J. Shukla, J. L. Kinter III, Y.-T. Hou, and E. Albertazzi
University of Maryland
College Park, Maryland

Prepared for
the National Aeronautics and Space Administration
under Grants NAGW-492 and NAGW-557

NASA
National Aeronautics and Space Administration
Office of Management
Scientific and Technical Information Division

1989

TABLE OF CONTENTS

ABSTRACT

The Simple Biosphere Model (SiB) of Sellers et al. (1986) was designed to simulate the interactions between the Earth's land surface and the atmosphere by treating the vegetation explicitly and realistically, thereby incorporating biophysical controls on the exchanges of radiation, momentum, sensible and latent heat between the two systems. This paper describes the steps taken to implement SiB in a modified version of the National Meteorological Center's spectral GCM. The coupled model (SiB–GCM) was used to produce summer and winter simulations. The same GCM was used with a conventional hydrological model (Ctl–GCM) to produce comparable 'control' summer and winter simulations.

It was found that SiB–GCM produced a more realistic partitioning of energy at the land surface than Ctl–GCM. Generally, SiB–GCM produced more sensible heat flux and less latent heat flux over vegetated land than did Ctl–GCM and this resulted in the development of a much deeper daytime planetary boundary layer and reduced precipitation rates over the continents in SiB–GCM. In the summer simulation, the 200 mb jet stream and the wind speed at 850 mb were slightly weakened in the SiB–GCM relative to the Ctl–GCM results and equivalent analyses made from observations.

1. INTRODUCTION

This report and the paper of Sato et al. (1989) describe a study in which a simple but biophysically based model of the terrestrial vegetation was implemented in a General Circulation Model (GCM) of the atmosphere. The motivation for the study was to assess the impact of implementing such a scheme on the simulated climate with particular reference to (i) observations where available and, (ii) a parallel simulation produced with an abiotic land surface model. The paper of Sato et al. (1989) reported on the results of the study: this report is complementary to the the paper in providing a detailed review of the technical aspects of the implementation and an expanded discussion of the reuslts.

Over the last decade, the scientific community has recognized that the interaction between the land surface and the atmosphere may play a significant role in the climate system; specifically, the fluxes of radiation, momentum and sensible and latent heat between the two systems may influence the atmospheric motion, temperature, humidity and precipitation fields which in turn feed back onto the spatial distribution of the sinks and sources of these fluxes on the land surface.

Until recently, the surface properties which regulate the exchange of radiation, momentum and heat between the land and the atmosphere have been regarded as separate items which may be independently prescribed as boundary conditions within a GCM. Although this approach is not very realistic, it lends itself to the investigation of land surface–atmosphere interactions by way of sensitivity studies conducted with GCM's. The three land surface properties which ultimately govern these interactions are the albedo (radiative transfer), surface roughness (momentum transfer) and the surface hydrological parameterization/prescription (sensible and latent heat transfer), all of which have been the subject of individual sensitivity studies.

First, the land surface albedo is known to vary from about 12% (tropical rain forest) to around 35% (Sahara desert) over the snowfree land, see Shuttleworth et al. (1984b) and Matthews (1984). Charney et al. (1977) executed a series of GCM sensitivity experiments centered on albedo changes in the Sahel which indicated that an increase in the albedo of the region would lead to a decrease in the surface evaporation rate and a reduction in the precipitation rate in the same area. This study has been followed by similar ones on the Sahel/Sahara region (Sud and Fennessy (1982) and Chervin (1979)) which produced the same result qualitatively if not quantitatively. Carson and Sangster (1981) performed a more radical experiment by comparing two simulation runs performed with a GCM wherein the global land surface albedo, α, was prescribed as 0.1 or 0.3. The higher albedo case was associated with a lowered precipitation rate over the land, (4.6 mm/day for $\alpha = 0.1$ and 3.4 mm/day for $\alpha = 0.3$).

The effect of changing surface roughness length (z_0) fields was investigated in a study by Sud and Smith (1985): The roughness length of the world's deserts was reduced from 45 cm to 0.2 mm which brought about changes in the fields of horizontal water vapor convergence and convective precipitation.

Not surprisingly, many sensitivity studies have been devoted to investigating the role of land surface hydrology in the exchange of energy between the surface and atmosphere. Walker and Rowntree (1977), Carson and Sangster (1981), Shukla and Mintz (1982), Warrilow (1986) and others reviewed in Mintz (1984) have performed experiments ranging from global prescriptions of totally wet versus totally dry land surfaces to alterations in regional soil moisture capacities. In almost all cases, reduced land surface evaporation rates led to reduced precipitation rates in the continental interiors.

All of the above experiments served to demonstrate that the specification of albedo, roughness and perhaps most importantly, the 'surface wetness' could have important impacts on atmospheric fields. It was pointed out by Dickinson (1984) that these experiments, though illustrative, were unrealistic, particularly with regard to the description of the land surface evapotranspiration process as conventionally specified in GCM's. Dickinson (1984) designed a land surface model which explicitly refers to the effects of vegetation which has since been used for a simulation study of the climatic impact of large scale deforestation of the Amazon Basin; see Dickinson and Henderson–Sellers (1988). Sellers et al. (1986) constructed the Simple Biosphere model (SiB) which incorporates much of the philosophy of the Dickinson (1984) model while differing in detail. Both of these models have undergone sensitivity studies which indicate that as well as being realistic, the recognition of the role of vegetation in GCM's should lead to more reasonable descriptions of the land surface–atmosphere fluxes. This paper reports on one such study, in which the conventional land surface hydrology model used in a research version of the National Meteorological Center (NMC) GCM was replaced by SiB. Changes in the simulated surface and atmospheric fields as a result of this implementation are discussed with reference to relevant observations where available.

2. DESCRIPTION OF THE MODEL AND EXPERIMENTAL DESIGN

The National Meteorological Center (NMC) spectral general circulation model (GCM) was originally designed and applied as a medium range forecast (MRF) model, see Sela (1980), but has recently been modified by us for use as a meteorological research tool. These modifications are reviewed below and include the implementation of a more efficient radiation scheme by Harshvardhan et al. (1987); the incorporation of a simple curve–fitted function in place of the full Monin–Obukhov scheme used to calculate surface transfer coefficients and resistances; inclusion of the Mellor and Yamada (1982) vertical diffusion scheme; and improvement of the time integration scheme used for the lower atmosphere and surface physics.

The model formulation of dynamics is described in Sela (1980) and Kinter et al. (1988) describe the physics, initialization procedures and boundary conditions. The model has a rhomboidal truncation at total wave number 40, Laplacian–square type horizontal diffusion to avoid spectral blocking and is discretized into 18 vertical levels of which the PBL may occupy five or six. It has a shallow convection scheme (Tiedtke et al. (1984) as well as a large–scale precipitation and cumulus convection scheme after Kuo (1965) which serves as a moist process parameterization. The model has three soil layers with prognostic temperatures at 2.5 cm, 10 cm, and 50 cm depth; the temperature at 500 cm is kept constant. The surface hydrology is represented by a bucket model (Manabe, 1969) wherein the wetness is defined as the soil moisture divided by three quarters of maximum field capacity which is taken to be 150 mm on all land surfaces. These model 'physics' were taken from the 1986 version of NMC medium range forecast model.

Some parameterizations were changed:

1. A more efficient radiation scheme was incorporated which allowed simulation of the diurnal cycle; see Harshvardhan et al. (1987). The long wave radiation scheme is based on that of Harshvardhan and Corsetti (1984) and the short wave (solar) radiation scheme is based on that of Lacis and Hansen (1974) as modified by Davies (1982). The solar radiation scheme was further modified to allow for partial cloudiness. The new long wave scheme has less spectral resolution than the pre–existing scheme of Fels and Schwarzkopf (1975), but it is not thought that this

simplification gives rise to serious errors. The short wave and long wave radiation tendencies are now calculated every hour and every three hours, respectively, which allows effective resolution of the diurnal cycle.

2. The description of the aerodynamic resistances (or surface drag coefficient) for momentum and sensible/latent heat transfer between the lowest model layer and the surface was based on the Monin–Obukhov similarity theory as used in the E2–physics package of the Geophysical Fluid Dynamics Laboratory (GFDL) model (Miyakoda and Sirutis, 1986). When the virtual temperature correction is neglected, the surface drag coefficient depends on only two nondimensional parameters, the Richardson number and z_r/z_0, where z_r is a reference height located within the lowest model layer and z_0 is the surface roughness length. A simple analytic function was developed that gives results close to those calculated with the original formulation (Appendix A). This function is used in order to avoid the costly iterations necessary for calculating the Monin–Obukhov length.

3. The level 2 second–order closure model of Mellor and Yamada, (1982) was implemented as a parameterization of vertical diffusion in the PBL. This has been used in the GFDL spectral model (Miyakoda and Sirutis, 1977) and the fine mesh grid model of the Japanese Meteorological Agency (Yamagishi, 1980). In this version of the scheme, the eddy transfer coefficient is a diagnostic function of Richardson number which makes it computationally expensive in operation.

4. The surface and PBL physics were coupled so that heat and mass exchanges between the surface and atmosphere satisfy energy and mass conservation laws (see Sec. 4). An implicit scheme with explicit coefficients was used with iteration to time–integrate the coupled system.

This modified version of the NMC GCM was used as the control model (Ctl–GCM) in this study.

The hydrological model in place in Ctl–GCM is the same as that used in the NMC and GFDL GCM's. The scheme consists of a conceptual bucket for each land point which is filled by precipitation and emptied by evaporation and runoff. The rate of evaporation is determined by the product of a potential evaporation rate; that is, the rate that would result from a saturated surface with the same roughness and surface temperature; and a wetness value, which is taken as a simple linear function of the level of water in the bucket. The scheme has the attraction of being conceptually simple, but cannot be considered a realistic description of the energy partition process as it occurs in nature. The most important omission in the bucket model is that of biophysical control of transpiration: vegetation can exert a considerable resistance on the transfer of water from soil to atmosphere and this can reduce the evapotranspiration rate to a level significantly below that calculated with the bucket formulation. Sellers (1987) discusses this and related shortcomings of the bucket model and concludes that it will almost always overestimate evaporation rates over the land. In this paper, we investigate the effect of replacing the conventional bucket hydrology model used in Ctl–GCM with the Simple Biosphere model (SiB) of Sellers et al. (1986).

SiB is described in Sellers et al. (1986) and is reviewed briefly in Sec. 3 of this paper; basically, it is a model which directly addresses the effect of vegetation on land surface–atmosphere interactions, by modeling those physiological and physical (biophysical) processes which influence radiation, momentum and heat transfer. This may be compared with the abiotic schemes currently used in most GCM's, see Sellers (1987). Here, we investigate the effect of replacing the conventional bucket hydrology model used

in Ctl–GCM with the Simple Biosphere model (SiB) of Sellers et al. (1986). SiB directly addresses the effect of vegetation on land surface–atmosphere interactions by modeling those physiological and biophysical processes which influence radiation, momentum, mass and heat transfer

Implementation of SiB necessitated a number of modifications to the control version of the GCM, as discussed in Section 3 of this paper. The complete Ctl–GCM combination was then used to produce 30–day summer and winter simulations which are compared to equivalent simulations produced by the Ctl–GCM, see Sec. 4. In both SiB–GCM and Ctl–GCM, the same boundary conditions for sea surface temperature (SST), sea ice distribution, initial snow amount and topography were used. The other land surface boundary conditions or parameters were treated differently in the two models.

Surface albedo in Ctl–GCM is interpolated from the seasonal climatology of Posey and Clapp (1964). In SiB–GCM, the albedo is calculated with a vegetation canopy radiation model based on the two stream approximation (Sellers, 1985). The albedo depends on vegetation type and state and the solar zenith angle (see Dorman and Sellers, 1989). Figure 1 shows the difference between the SiB–GCM and Ctl–GCM albedo fields for the June–July period. Over most of the continental areas except for north of 50° N the Posey and Clapp (1964) albedo field is unrealistically low for reasons discussed in Dorman and Sellers (1989). The high albedo to the north of 65° N in Ctl–GCM is appropriate for snow–covered conditions.

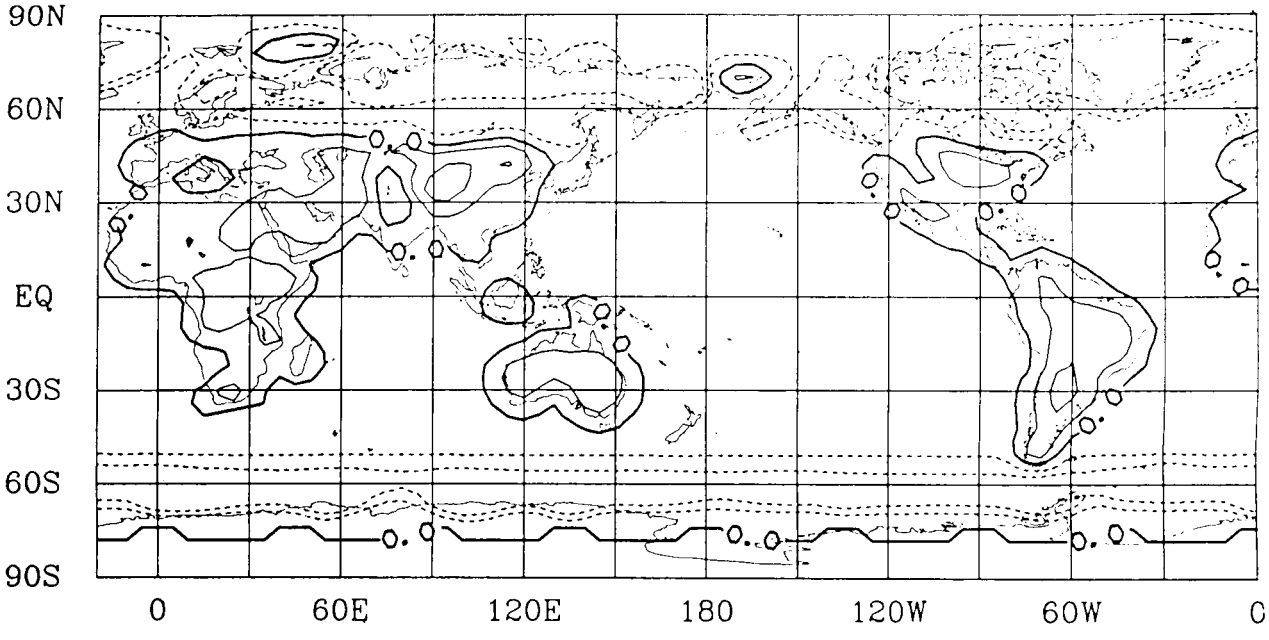

Figure 1: Difference map of the global albedo fields as generated by SiB–GCM and as prescribed for Ctl–GCM from the data of Posey and Clapp (1964). The fields are averages for the June–July Period. The solid contours indicate regions where SiB–GCM generates higher albedo values, the broken contours indicate where Ctl–GCM has higher albedo values. In all cases, the contour interval is 0.05.

Surface roughness length, z_0, is time invariant in Ctl–GCM while in SiB–GCM it depends on the vegetation type and month of the year (see Dorman and Sellers, 1989). The major differences between the two models are to be found in the deserts of China and Mongolia: the roughness lengths there are around 30 cm in Ctl–GCM and 1 cm in SiB–GCM which may be compared to values of 1 cm reported by Matthews (1984).

Up to now, the normal practice in Ctl–GCM has been to update the global soil moisture field at daily intervals during a simulation, thus effectively maintaining the wetness at or near its 'climatological' value at every grid point. This procedure was retained for the Ctl–GCM runs discussed in this paper, but a test was executed in which Ctl–GCM calculated the time–evolution of the soil moisture. It was found that there were only small differences between the wetnesses and heat flux fields produced by those two versions of the Ctl–GCM (see later sections). In SiB–GCM, soil moisture was predicted throughout all simulations.

The soil moisture and temperature initializations are reviewed in Appendices D and E respectively. As discussed in Sellers et al. (1986), the initialization of the soil moisture field is particularly problematical as it has a relatively long 'memory'; the soil column in mid latitude zones is capable of storing several hundred mm of water which translates to one or two months worth of evapotranspiration and runoff. In Appendix D, we describe the technique for initializing the SiB–GCM soil moisture field so as to make it equivalent to the Ctl–GCM initial field; equivalent, that is, in that a given SiB–GCM grid point is assumed to have been exposed to more–or–less the same climatic history as its Ctl–GCM counterpart up until the start of the simulation run. This technique allows us to transform the Ctl–GCM initial soil moisture fields into equivalent SiB–GCM fields. (The former were prepared by Willmott et al. (1985) using an hydrological budget method forced by observations of precipitation and air temperature.) The accuracy of these initial fields is questionable, a fact which is all the more disquieting as (a) it is certain that soil moisture initialization has a profound effect on the ensuing time–series of surface heat flux fields and (b) the simulation runs discussed in this paper are comparatively short. The obvious solution to the problem is to run both GCM's for several years to generate self–consistent soil moisture climatologies, an option that was not available to us during this study due to constraints on computer time.

A final comment on the effects of the soil moisture initialization: within the upper range of soil wetness values; that is, greater than about 0.5, both models' responses are almost completely insensitive to the soil wetness, see Sellers and Dorman (1987). It is only when the soil moisture content drops below these values that we expect an impact on the calculated evapotranspiration rate. It will be shown in later discussion that the greatest differences between the land surface evaporation rates calculated by the two models occurred in zones with relatively high soil moisture contents.

The two GCMs, Ctl–GCM and SiB–GCM, were integrated for 50 days from 00 UTC June 15, 1986, and 30 days from 00 UTC December 15, 1985. The simulated fields were compared to investigate the impact of including a biophysically–based surface parameterization in a GCM. Particular attention has been paid to the differences between the land surface hydrology and energy budgets produced by the two models.

Two additional 30–day summer case experiments were made: A SiB–GCM run with a reduced soil moisture initialization in North America and a Ctl–GCM run in which the time–evolution of the soil moisture was calculated rather than prescribed from climatology.

Following the completion of all the experiments, four coding errors were found; one in Ctl–GCM, one in SiB–GCM and two common to both models. In Ctl–GCM, the surface sensible heat flux was estimated by integrating the time rate of change in virtual temperature (rather than actual temperature) over the atmospheric column. This diagnostic error leads to errors in the Ctl–GCM sensible heat flux fields on the order of 1%. In SiB–GCM, the moisture contribution to the time–tendency of the virtual temperature due to vertical diffusion was treated incorrectly which again is thought to lead to errors on the order of 1%. Third, eddy diffusivities in SiB–GCM were four times as large as equivalent values obtained with the original Mellor–Yamada (1982) code. Last, in implementing the Mellor and Yamada (1982) scheme, the interlayer Richardson numbers were multiplied by a factor of two (relative to the original scheme) which leads to more rapid transitions from stable to unstable transfer conditions within the atmospheric column. This last error is common to both GCMs, but is not thought to have a severe impact on the simulations as for most of the time the transfer coefficients are operating on the 'plateau' regions (i.e., stable or unstable conditions) where the eddy coefficients are not sensitive to the value of the Richardson number.

3. OVERVIEW OF THE SIMPLE BIOSPHERE MODEL (SiB)

Here we briefly describe the philosophy, structure, atmospheric boundary conditions and prognostic variables of SiB. This is followed by a description of the implementation of SiB into the GCM and a discussion of the anticipated impact of SiB on the calculation of the surface heat, moisture and energy budgets.

3.1 Model Philosophy

In most GCMs, including the original NMC GCM and Ctl–GCM, the fluxes of radiation, heat (sensible and latent) and momentum across the land surface–atmosphere boundary are conceptualized as largely separate processes, so that a given grid point has an independently specified albedo, an independently specified roughness length and an independently formulated dependence of evapotranspiration on soil moisture. This last generally takes the form of the bucket model described in the preceding section.

The interactions between the land surface and the atmosphere which are of direct climatological significance on time scales of seconds to years are discussed in Sellers et al. (1986). They may be briefly summarized as follows:

(i) **Radiation Absorption:** The spectral properties of leaves and multiple reflections between them make vegetative canopies highly absorbent in the visible (photosynthetically active radiation – PAR) wavelength interval ($0.4 - 0.72$ μm) and moderately reflective in the near–infrared region ($0.72 - 4.0$ μm). In contrast, bare ground generally exhibits a relatively flat variation in reflectivity over the interval of $0.4 - 4.0$ μm.

(ii) **Biophysical Control of Evapotranspiration:** Higher plants regulate the amount of gas exchange (and hence water loss) between their saturated interior tissues and the external air by means of valve–like structures on the leaf surface (stomates). These appear to respond to the environmental conditions of PAR flux density, temperature, humidity and leaf water potential so as to maximize the ratio of CO_2 influx to water vapor flux (see Farquhar and Sharkey, 1982) or to conserve moisture in times of water stress. Besides the active physiological control of evapotranspiration, plants also influence the rate at which free water on the land surface is returned to

the atmosphere: vegetative canopies intercept precipitation which can be directly re–evaporated to produce relatively high but short–lived releases of latent heat into the atmosphere.

(iii) **Momentum Transfer**: Vegetative canopies usually present a rough, porous surface to the near–surface airflow. The resultant turbulence enhances the transport of sensible and latent heat away from the surface while exerting a drag force which may be significantly larger than that produced by bare ground.

(iv) **Soil Moisture Availability**: The depth and density of the vegetation root systems and the physical properties of the soil determine the amount of soil moisture available for evapotranspiration.

(v) **'Insulation'**: The soil surface under a dense vegetation canopy intercepts less radiation and may also be aerodynamically sheltered. As a result, the energy available to the covered soil is small and the component terms of the soil energy budget (evaporation, sensible heat flux and ground heat flux) are correspondingly reduced.

In designing the SiB model, the philosophy was to model the vegetation itself and thereby calculate the radiation, momentum, heat and mass transfer properties of the surface in a consistent way. The morphological and physiological characteristics of the vegetation community at a grid point are used to derive the coefficients which govern the fluxes between the surface and the atmosphere. All of these fluxes depend upon the state of the vegetated surface and the atmospheric boundary conditions.

In SiB, the world's vegetation communities are classified into twelve types or biomes, see Fig. 2. Detailed descriptions of the methods used to transform the morphological and physiological characteristics of a given vegetation community into the model parameters are given in Sellers et al. (1986) and the data sets and methodologies used to define the global distribution of vegetation types and attributes in SiB–GCM are reviewed in Dorman and Sellers (1989).

3.2 Model Structure.

In SiB, vegetation is divided into two morphological groups: Trees or shrubs which constitute the upper story or canopy vegetation, and the ground cover which consists of grasses and other herbaceous plants. Either, both or neither of these vegetation covers may be present in a given grid area. The upper story vegetation consists of perennial plants with persistent roots assigned to a fixed depth taken to be the bottom of the second soil layer. The ground cover is made up of annual plants and may have a time–varying root depth. There is a upper, thin soil layer (soil layer 1), from which there can be a significant rate of withdrawal of water by direct evaporation into the air when the pores of the soil are at or near saturation. Beneath the root zone (soil layer 2), there is an underlying recharge layer (soil layer 3) where the transfer of water is governed only by gravitational drainage and hydraulic diffusion. The parameters required for each vegetation type in SiB are listed in Table 1 of Sellers et al. (1986). Values for many of the parameters are given in Dorman and Sellers (1989).

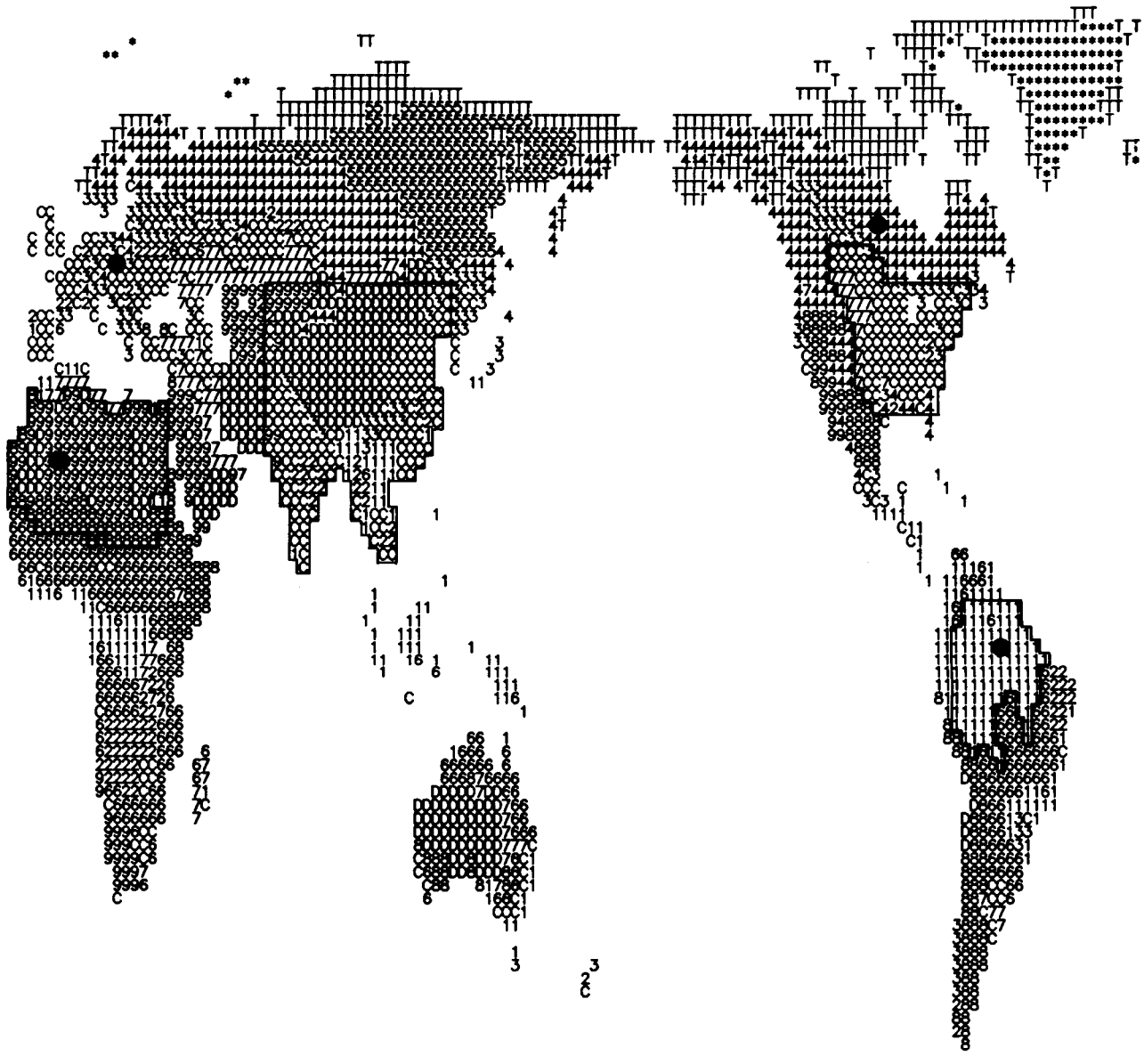

Figure 2: Distribution of SiB vegetation types on the 128 x 102 Gaussian grid used in the NMC GCM.

1—broadleaf evergreen
2—broadleaf deciduous
3—mixed broadleaf deciduous and needleleaf evergreen
4—needleleaf evergreen
5—needleleaf deciduous
6—grass and broadleaf deciduous shrubs
7—grass
8—broadleaf deciduous, shrub, growth singly, in patches or groups
9—broadleaf deciduous, shrub, growth singly, or in patches (semi—desert)
T—tundra
D—desert
C—cultivated land represented by wheat
*—glacier

The sites used for the diurnal variation studies in Sec. 4.1 are marked with solid dots. Energy and moisture budget analyses were made for the four areas encircled by solid lines, see Sec. 4.2.

3.3 Atmospheric Boundary Conditions for SiB

The upper boundary conditions by SiB are as follows:

Air temperature, vapor pressure and wind speed of the lowest model layer; T_r, e_r, u_r.

Solar zenith angle, μ.

Five components of the incident radiation; F(o)

$F_{s,b(o)}$,	Visible or PAR (< 0.72 μm) direct beam radiation,
$F_{s,d(o)}$,	Visible or PAR (< 0.72 μm) diffuse radiation,
$F_{n,b(o)}$,	Near Infrared ($0.72 - 4.0$ μm) direct beam radiation,
$F_{n,d(o)}$,	Near Infrared ($0.72 - 4.0$ μm) diffuse radiation,
$F_{t,d(o)}$,	Thermal Infrared ($8.0 - 12.0$ μm) diffuse radiation,

Large scale and convective precipitation rates; PL, PC.

3.4 Prognostic physical state variables of SiB and their governing equations

SiB has eight prognostic physical–state variables: three temperatures (one for the canopy vegetation, T_c, one for both the ground cover and the soil surface, T_{gs}, and a deep soil temperature, T_d); two interception water stores (one for the canopy, M_c, and one for the ground cover, M_g); and three soil moisture stores (W_1, W_2, and W_3). The subscripts $_c$ and $_g$ refer to canopy and ground cover vegetation, respectively, and $_s$ refers to the soil surface. The combined subscript $_{gs}$ refers to the ground (ground cover vegetation and soil) and $_d$ refers to the deep soil. The subscripts $_1$, $_2$, and $_3$ refer to soil layers.

The governing equations for the three temperatures, T_c, T_{gs}, and T_d are

$$C_c \dot{T}_c = Rn_c - H_c - \lambda E_c, \tag{1}$$

$$A \dot{T}_{gs} = Rn_{gs} - H_{gs} - \lambda E_{gs} - \frac{2\pi A}{\tau}(T_{gs} - T_d), \tag{2}$$

and

$$A \dot{T}_d = \frac{2(Rn_{gs} - H_{gs} - \lambda E_{gs})}{\sqrt{365\pi}}, \tag{3}$$

where

T_c, T_{gs}, T_d	=	temperature, K
Rn_c, Rn_{gs}	=	absorbed net radiation, W/m^2
H_c, H_{gs}	=	sensible heat flux, W/m^2
E_c, E_{gs}	=	evapotranspiration rate, kg/m^2/s
C_c	=	canopy heat capacity, J/m^2/K
λ	=	latent heat of vaporization, J/kg
τ	=	day length, s
A	=	effective heat capacity of soil, J/m^2/K.

The dot superscript $(\cdot)$ represents partial differentiation with respect to time.

In Eqs. (2) and (3), the original 'slab' model used to describe soil heat flux in SiB has been replaced by the force–restore formulation of Deardorff (1977). E_c, the evapo–transpiration from the canopy, has two components: i) E_{wc}, evaporation of water from the wetted fraction of the canopy (canopy interception loss), and ii) E_{dc}, transpiration of soil water extracted by the root system and lost from the dry fraction of the canopy.

E_{gs}, the evapotranspiration from the ground cover and the surface soil layer has three components: i) E_{wg} and ii) E_{dg} which correspond to E_{wc} and E_{dc} for the ground cover, and iii) E_s, direct evaporation of water from the surface soil layer.

The governing equations for the two interception water stores are

$$\dot{M}_c = P_c - D_c - E_{wc}/\rho_w, \tag{4}$$

and

$$\dot{M}_g = P_g - D_g - E_{wg}/\rho_w \tag{5}$$

where

M_c, M_g = water stored on the leaves, m
P_c, P_g = rate of precipitation interception, m/s
D_c, D_g = water drainage rate, m/s
E_{wc}, E_{wg} = rate of evaporation of water from the wet portions of the leaves, kg/m^2/s
ρ_w = density of water, kg/m^3

The governing equations for the three soil moisture stores are

$$\dot{W}_1 = \frac{1}{\delta_s D_1}\left[P_1 - Q_{1,2} - \frac{1}{\rho_w}(E_s + E_{dc,1} + E_{dg,1})\right] \tag{6}$$

and

$$\dot{W}_2 = \frac{1}{\delta_s D_2}\left[Q_{1,2} - Q_{2,3} - \frac{1}{\rho_w}(E_{dc,2} + E_{dg,2})\right] \tag{7}$$

and

$$\dot{W}_3 = \frac{1}{\delta_s D_3}\left[Q_{2,3} - Q_3\right] \tag{8}$$

where

W_1, W_2, W_3 = soil moisture wetness in the three soil layers
= δ_i/δ_s
δ_i = volumetric soil moisture in layer $_i$, m^3/m^3
δ_s = value of δ_i at saturation, m^3/m^3
D_i = thickness of ith soil layer, m
$Q_{i,i+1}$ = flow between $_i$ and $_{i+1}$ soil layer, m/s
Q_3 = gravitational drainage from recharge soil moisture store, m/s
$E_{dc,i}$, $E_{dg,i}$ = canopy, ground cover abstraction of soil moisture by transpiration from the ith soil layer, kg/m^2/s
P_1 = infiltration of precipitation into the upper soil moisture store, m/s
= minimum (P_o, K_s)
= O, when $W_1 = 1$
K_s = hydraulic conductivity of saturated soil, m/s
P_o = effective precipitation rate on soil surface, m/s
= $P - (P_c + P_g) + (D_c + D_g)$
P = Precipitation rate above the canopy, m/s

The precipitation excess, $(P_o - P_1)$, joins the gravitational outflow from the lowest soil moisture store, Q_3, to produce runoff, Q_r,

$$Q_r = P_o - P_1 + Q_3 \tag{9}$$

Equations (1) through (8) represent the governing equations for SiB and may be used in conjunction with time series of meteorological data to simulate the energy balance of a given site.

3.5. Implementation of SiB into the NMC Spectral Model

Our experience to date has shown that it is necessary to adapt the implementation of SiB into the individual GCM in question. As first implemented in the Goddard Laboratory for Atmospheres (GLA) Fourth–order GCM, all of the prognostic variables except for T_c and T_{gs} were time–integrated with a forward differencing scheme. The two 'fast' variables T_c and T_{gs} (which have relatively rapid time rates of change due to the large ratio of the flux terms (Rn, H, λE) to the heat conduction/storage terms (scaled by C_c and A) were integrated by a backward implicit scheme which assumes that T_r, e_r and u_r are constant through the time step. This scheme produced no numerical ill–effects as in the GLA GCM, the lowest model layer is very thick (~100 mb) which makes T_r and e_r relatively insensitive to the addition of sensible and latent heat fluxes over short ($\leq$ 1800 secs) time steps. The backward differencing technique used to solve (1) and (2) therefore involved taking partial derivatives of the right hand side of (1) and (2) with respect to T_c and T_{gs} and solving for ΔT_c and ΔT_{gs}, the net changes in T_c and T_{gs} over a time step.

Implementation of SiB into the University of California at Los Angeles/Goddard Laboratory for Atmospheres (UCLA/GLA) model of Randall et al. (1985) could not be achieved so simply. The UCLA/GLA model has a planetary boundary layer (PBL) formulation in which the PBL height, π_B, may vary from a few millibars (~ 10 m) to over 180 mb (~ 1.5 km). The time rates of change of the PBL potential temperature, θ_B, and the PBL mixing ratio, are highly variable, being large when the PBL is shallow, and small when the PBL is deep. The formulations governing π_B, θ_B, and q_B are complex in themselves as they involve surface heating terms, internal PBL dynamics and entrainment terms.

A scheme was developed which ensures the solution of (1) and (2) with equations for the time rate of change of the PBL height, potential temperature and mixing ratio without numerical problems. Basically the variables θ_B and q_B are added to the 'fast' variable set and appropriate time derivatives of T_{gs}, T_c, θ_B and q_B are calculated at the beginning of each time step. (π_B is advanced using a forward differencing scheme). These equations are then solved using a simple backward differencing scheme. This implementation (in the UCLA/GLA model) was used as the basis for the SiB implementation in the modified version of the NMC model.

In the NMC model, the Mellor and Yamada (1982) vertical diffusion model (level 2) was incorporated. In this parameterization, there are no explicit prognostic variables that describe the state of the PBL: the whole atmosphere, including the PBL, is discretized into layers and the state variables such as temperature, specific humidity and wind velocity are defined and predicted on each level; specifically, temperature and wind are defined at all of the model's 18 levels while specific humidity is defined at the 12 lowest levels. These atmospheric variables were coupled with the SiB prognostic variables, T_c and T_{gs}, so

that energy and mass are conserved and an implicit scheme was used to integrate the system stably in time. The other (slowly–varying) SiB variables were integrated with a forward scheme.

The tendencies for the time rate of change of the temperature, θ_1, and specific humidity, q_1, of the lowest atmospheric layer resulting from the transfer of heat fluxes from the surface are

$$M_1^T \dot{\theta}_1 = F_1^T + \frac{g\,H}{C_p \Delta p_1} \tag{10}$$

and

$$M_1^Q \dot{q}_1 = F_1^Q + \frac{gE}{\Delta p_1}. \tag{11}$$

$M_1^T = F_1^T$

$M_1^Q = F_1^Q$

C_p = specific heat of air, J/kg/K
g = acceleration due to gravity, m/s^2
H = total surface sensible heat flux, W/m^2
E = total surface evaporation rate, kg/m^2/s
Δp_1 = lowest atmospheric layer thickness, mb

In order to integrate the coupled system stably in time, the equations were made implicit with explicit coefficients.

$$\left[M_1^T - \frac{g}{C_p \Delta p_1}\frac{\partial H}{\partial \theta_1}\right]\dot{\theta}_1 - \frac{g}{C_p \Delta p_1}\frac{\partial H}{\partial T_c}\dot{T}_c - \frac{g}{C_p \Delta p_1}\frac{\partial H}{\partial T_{gs}}\dot{T}_{gs} = F_1^T + \frac{g}{C_p \Delta p_1} H \tag{12}$$

$$\left[M_1^Q - \frac{g}{\Delta p_1}\frac{\partial E}{\partial q_1}\right]\dot{q}_1 - \frac{g}{\Delta p_1} - \frac{\partial E}{\partial T_c}\dot{T}_c - \frac{g}{\Delta p_1}\frac{\partial E}{\partial T_{gs}}\dot{T}_{gs} = F_1^Q + \frac{g}{\Delta p_1} E \tag{13}$$

$$\left[C_c + \frac{\partial H_c}{\partial T_c} + \frac{\partial \lambda E_c}{\partial T_c}\right]\dot{T}_c + \left[\frac{\partial H_c}{\partial T_{gs}} + \frac{\partial \lambda E_c}{\partial T_{gs}}\right]\dot{T}_{gs} + \frac{\partial H_c}{\partial \theta_1}\dot{\theta}_1 + \frac{\partial E_c}{\partial q_1}\dot{q}_1 = Rn_c - H_c - \lambda E_c \tag{14}$$

$$\left[A + \frac{\partial H_{gs}}{\partial T_{gs}} + \frac{\partial \lambda E_{gs}}{\partial T_{gs}}\right]\dot{T}_{gs} + \left[\frac{\partial H_{gs}}{\partial T_c} + \frac{\partial \lambda E_{gs}}{\partial T_c}\right]\dot{T}_c + \frac{\partial H_{gs}}{\partial \theta_1}\dot{\theta}_1 + \frac{\partial E_{gs}}{\partial q_1}\dot{q}_1 = Rn_{gs} - H_{gs} - E_{gs}\frac{2\pi A}{\tau}(T_{gs} - T_d) \tag{15}$$

In Eqs. (14) and (15) no time derivatives of the surface net radiation terms, Rn_c and Rn_{gs}, were calculated as these are small compared to the other terms. Flux derivatives like $\frac{\partial H}{\partial T_c}$ were evaluated at time level $t-\Delta t$ and once the system was integrated, T_c, T_{gs}, θ_1, q_1 at time level $t+\Delta t$ were used to compute the new values of the non–neutral aerodynamic transfer coefficients. The four equations were then used to integrate T_c, T_{gs}, θ_1, q_1 again. The time tendencies for the first layer were obtained by dividing $\theta_1^{t+\Delta t} - \theta_1^{t+\Delta t}$ and $q^{t+\Delta t} - q^{t-\Delta t}$ by $2\Delta_t$. Time tendencies of potential temperature and specific humidity at other levels were computed by solving the matrices of the diffusion equations successively from the bottom to the top of the atmosphere (Appendix B). These tendencies were added to the tendencies due to advection and other physical processes to give the total tendency for each prognostic variable.

In treating the vertical diffusion of momentum, an implicit noniterative time integration scheme with explicit coefficients was used. The surface drag coefficient was evaluated using T_c, T_{gs}, θ_1, q_1 at time level $t+\Delta t$ after the first integration of Eqs. (12) to (15).

Ctl–GCM uses the same basic time integration scheme. In Ctl–GCM, the atmospheric variables (temperature at 18 levels and specific humidity at 12 levels) were coupled with the ground surface temperature and soil temperatures at 10 cm and 50 cm depth. The system was integrated using the same implicit time integration scheme with explicit transfer coefficients. Iterations were made using a modified Newton–Raphson method to insure against numerical oscillations.

As currently implemented, SiB has a significant impact on the computer time required for a simulation; SiB–GCM is typically 20 percent more expensive (computationally) than Ctl–GCM. However, it should be noted that as yet no great effort has been dedicated to making the code more efficient.

3.6 Anticipated impact of implementing SiB

The impact of implementing SiB into the GCM can be anticipated by comparing the surface parameterizations of SiB–GCM and Ctl–GCM.

First, there are some differences between the albedo field calculated by SiB–GCM and that prescribed in Ctl–GCM, see Fig. 1. Generally, the SiB–GCM albedos are significantly higher over vegetated regions, leading to reductions in the surface net radiation of around 5% in SiB–GCM relative to Ctl–GCM.

Second, there are some differences between the two roughness length fields, but these are not thought to contribute greatly to the differences between the performances of the two models except for the extreme cases referred to in a previous section (China, Mongolia). This is because the aerodynamic resistance is inversely related to the logarithm of the roughness length and so the turbulent heat flux calculations are relatively insensitive to fairly large changes in the absolute value of this parameter, see Sellers and Dorman (1987).

Third and most importantly, Ctl–GCM and SiB–GCM calculate the partition of energy at the surface in very different ways. The effect of this can be simply illustrated by comparing the energy budgets calculated by the two surface parameterizations for a densely vegetated area. If time–invariant forcing (T_r, e_r, u_r, $F(o)$) is assumed and the radiation budgets for the two models are taken as approximately equal, heat storage terms

may be neglected and equilibrium surface fluxes and surface temperatures may be calculated with the two parameterizations. Under these conditions, the total energy budgets may be written as

$$R_n = H_B + \lambda E_B \quad (16a)$$

$$R_n = H_S + \lambda E_S \quad (16b)$$

R_n = net radiation, W/m^2
H = sensible heat flux, W/m^2
E = evaporation rate, $kg/m^2/s$
λ = latent heat of vaporization, J/kg

The subscripts B and S refer to the 'bucket' and SiB parameterizations, respectively.

The sensible heat fluxes calculated by the two models are different due to the different equilibrium surface temperatures.

$$H_B = \frac{(T_B - T_r)}{r_a} \rho C_p \quad (17a)$$

$$H_S = \frac{(T_S - T_r)}{r_a} \rho C_p \quad (17b)$$

$T_{S,B}$ = surface temperature for SiB, bucket parameterizations, respectively K.
ρ, c_p = density, specific heat of air, respectively; kg/m^3, J/kg/K.
r_a = aerodynamic resistance between surface and lowest model layer, s/m
= $1/(C_H u_r)$
C_H = heat transfer coefficient.

For Ctl–GCM, the evaporation rate is given by the so–called 'Beta–function'.

$$\lambda E_B = \beta \frac{(e*(T_B) - e_r)}{r_a} \frac{\rho c_p}{\gamma} \quad (18a)$$

$e*(T)$ = saturated vapor pressure at temperature T, kPa
γ = psychrometric constant, kPa/K.
= 0.066 kPa/K at 15° C.
β = $\frac{W}{0.75\ W_{max}}$, $0 \leq \beta \leq 1$
W = soil moisture content, mm
W_{max} = Maximum value of W,
= 150 mm

In SiB, the calculation of evapotranspiration is fairly complex, involving treatments for two layers of vegetation and the evaporative contribution from the bare soil. However, for a dense vegetation canopy, like a tropical forest, the evapotranspiration rate can be approximated by

$$\lambda E_S = \left[\frac{e*(T_S) - e_r}{r_a + r_c}\right] \frac{\rho C_p}{\gamma} \qquad (18b)$$

r_c = bulk stomatal (canopy) resistance, s/m

The essential term in Eq. (18b) is r_c, the bulk stomatal or canopy resistance of the dry vegetation.

Equations (16), (17), and (18) can be combined and the surface temperatures, T_S and T_B, eliminated using the linear approximation for saturated vapor pressure as a function of temperature as shown in Monteith (1973) to yield

$$\lambda E_B = \frac{\Delta R_n + \rho C_p \, \delta e / r_a}{\Delta + \gamma/\beta} \qquad (19a)$$

$$\lambda E_S = \frac{\Delta R_n + \rho C_p \, \delta e / ra}{\Delta + \gamma\left[\frac{r_a + r_c}{r_a}\right]} \qquad (19b)$$

δe = vapor pressure deficit, kP_a
= $e*(T_r) - e_r$
Δ = slope of saturated vapor pressure versus temperature curve at temperature T_r, kP_a/K
= 0.11 kP_a/K at 15° C

Equation (19b) is simply the Penman–Monteith evapotranspiration equation, see Monteith (1973). For the same meteorological (T_r, e_r, u_r) and radiative (R_n) forcings, the ratio of the calculated evapotranspiration rates is then given by

$$\frac{E_B}{E_S} = \frac{\Delta + \gamma\left[\frac{r_a + r_c}{r_a}\right]}{\Delta + \gamma/\beta} \qquad (20)$$

For a tropical forest site, r_a is typically 10 s/m and, if soil moisture is not limiting, $\beta = 1$ and $r_c \simeq 100$ s/m, see Shuttleworth et al (1984, a,b), which yields a value of $E_B/E_S = 4.75$! Furthermore, to obtain $E_B/E_S = 1$, β must be reduced to 0.091 which implies a soil wetness of $W = 0.07$, clearly below the range of reasonable 'tuning' for a humid region.

The above analysis is extreme as it assumes that these is no feedback from the surface evaporation rate on the atmospheric forcing. In Ctl–GCM, the huge latent heat fluxes calculated in the first few timesteps should bring about an unrealistically cold, stable and humid PBL which then reduces subsequent evaporation rates to less extreme values. Nonetheless, we should expect to see marked differences between the surface heat fluxes calculated by the two models with associated differences in their near surface climates.

4. COMPARISON OF SIMULATIONS AS PRODUCED BY CONTROL AND SiB VERSIONS OF THE NMC GCM.

In this section, the simulations generated by the SiB–GCM and Ctl–GCM runs are compared with each other and with observations over a range of spatial scales.

First, analyses of surface and near–surface processes for representative grid points within each model (see Fig. 2) were compared with equivalent field measurements. In particular, the 30–day means of the simulated hourly net radiation, sensible heat and latent heat fluxes for a tropical forest, a coniferous forest and an agricultural site are compared with observations (see Sec. 4.1).

Second, the simulated time–series of the energy and moisture budgets of four large regions: the Amazon Basin, central and eastern United States, southern Asia and the Sahara (see Fig. 2) – are discussed with reference to observations where available (Sec. 4.2).

Third, the global fields of latent heat flux (evapotranspiration), sensible heat flux and precipitation generated by SiB–GCM and Ctl–GCM are compared (Sec. 5.3).

Fourth and last, the impacts of the two land surface parameterization schemes on the large scale atmospheric circulation are discussed (Sec. 4.4).

4.1 Diurnal variation of surface and near–surface processes.

Time series of fluxes and other variables for several grid points over the globe were examined to see how the implementation of SiB affects the diurnal variation of surface and PBL processes. The first 30 days of the SiB–GCM and Ctl–GCM runs were analyzed for this study; 30 rather than 50 days were used as the surface energy budget changed rapidly and in a spatially heterogeneous way in the last 20 days of the Ctl–GCM run, see later sections.

4.1.1 Tropical rain forest, Amazon Basin

Figures 3 through 9 show 30–day means of the simulated diurnal variation of various physical parameters at a tropical forest grid point near Manaus in the Amazon basin (59° W, 3° S) for the period June 15–July 14. Some equivalent observations of Shuttleworth et al. (1984a,b, and private comm.) are also presented for comparison.

The difference between the albedos used by the two models may be seen in Fig. 3. In SiB–GCM the albedo is computed using a two stream approximation model (Sellers, 1985) which calculates the dependency of the albedo on the solar zenith angle. The minimum albedo at noon, (11.5%), and the daily mean albedo (12.6%) as calculated by SiB–GCM agree well with the observations made over the Amazon forest (Shuttleworth, 1984b); 11.0% and 12.5% respectively. The albedo used in Ctl–GCM (Posey and Clapp, 1964) is a climatological one and has a seasonal variation. It is unrealistically small for reasons discussed in Dorman and Sellers (1989).

Because the albedos are different, there is a slight difference between the net radiation values calculated by SiB–GCM and Ctl–GCM (Figs. 4a,b); but the peak observed net radiation is 50–100 W/m^2 less than both of the simulated values. However, the observed net radiation is always significantly smaller than the sum of the observed latent and sensible heat fluxes which suggests that there may be some errors in the observed heat fluxes and/or net radiation values. Additionally, it is likely that the fixed zonal mean climatological cloudiness used in both GCM's leads to errors in the simulations.

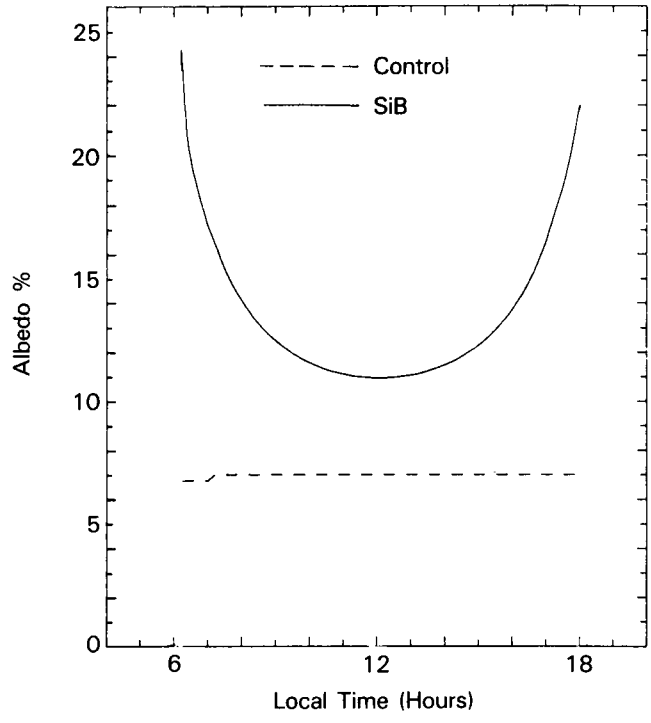

Figure 3: 30—day mean (June 15 — July 14) surface albedo at a tropical forest grid area near Manaus (59° W, 3° S) as simulated by SiB—GCM (solid line) and as given by Posey and Clapp (1964) for Ctl—GCM (dashed line). The period June 15 — July 14 is used for all the 30—day summer means referred to below.

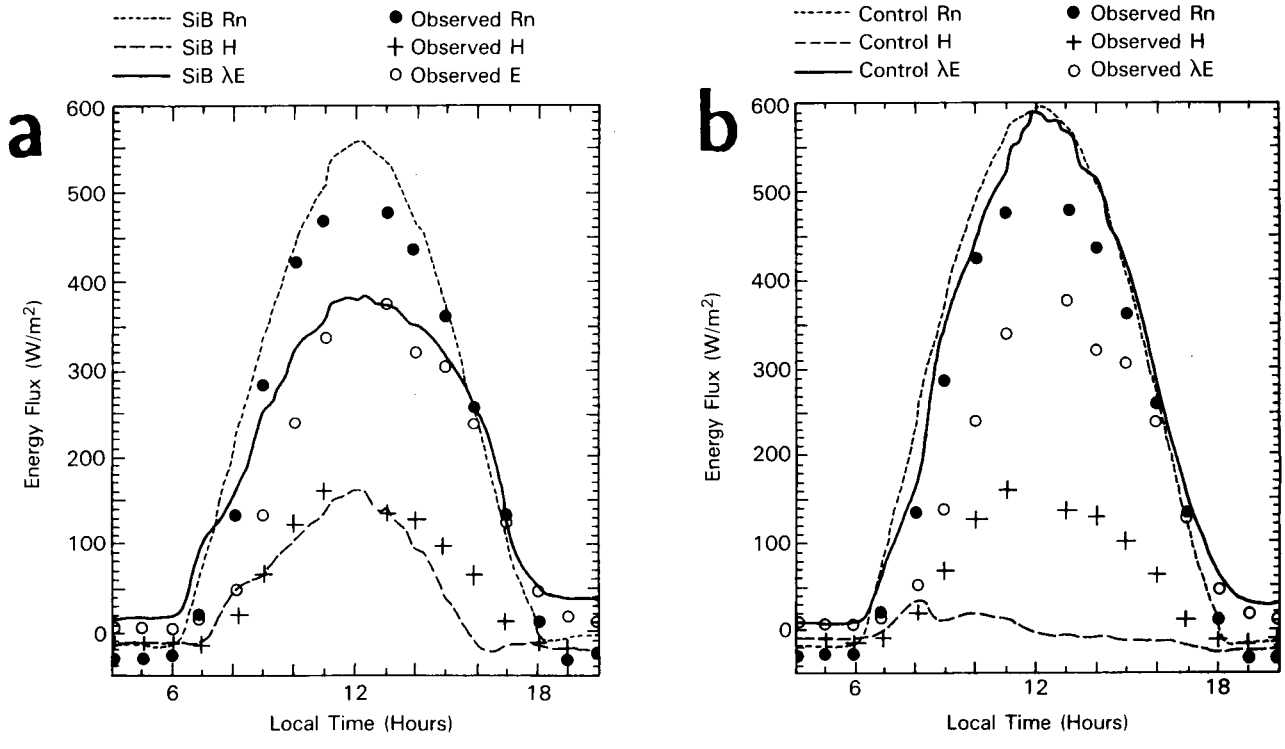

Figure 4: 30—day surface energy balance for the tropical forest grid point near Manaus as simulated by SiB and as observed by Shuttleworth et al. (1984a). The lines on the figure represent simulation, the points (circles and crosses) represent the means of observations taken over the period June 15, 1984 — July 14, 1984 at a site 30 km from Manaus, Brazil. a) SiB—GCM b) Ctl—GCM

The heat flux into the soil is not shown in Figs. 4a and 4b. Typically, this term is calculated to be around 20 W/m^2 during the day and –20 W/m^2 at night. The daily mean value is very small and is an insignificant part of the surface energy budget in both models.

Figures 4a and 4b dramatically illustrate the improvement of the simulated surface energy budget due to the implementation of SiB–GCM. The simulations may be directly compared with the observations: 30 days (June 15 – July 14, 1984) of the Shuttleworth et al. (1984a) data set were averaged to produce the observed hourly fluxes shown in Figs. 4a and 4b. In SiB–GCM the maximum values of latent heat flux, 380 W/m^2, and sensible heat flux, 170 W/m^2, agree fairly well with these observations. In Ctl–GCM (Fig. 4b), however, almost all of the net radiation is used for evaporation while the sensible heat flux is almost zero.

This unrealistic partitioning of net radiation in Ctl–GCM is a direct consequence of using the bucket model parameterization of surface evaporation. In the bucket model, the atmosphere is directly connected to the surface by the aerodynamic resistance which is relatively small when the surface layer is neutral or unstable, see Eq. (18a). In SiB–GCM, the transpired water also has to traverse the stomatal resistance which is typically one order of magnitude larger than aerodynamic resistance over the Amazon forest, see Eq. (18b). (In both SiB–GCM and Ctl–GCM, sensible heat fluxes are only regulated by the aerodynamic resistances). The morning and midday values of the aerodynamic resistance, r_a, are around 10 s/m in both SiB–GCM and Ctl–GCM, but the stomatal resistance, r_c, plus leaf boundary layer resistance, r_b, in SiB–GCM never drops below 100 s/m. According to Shuttleworth et al. (1984a), daytime values of the aerodynamic

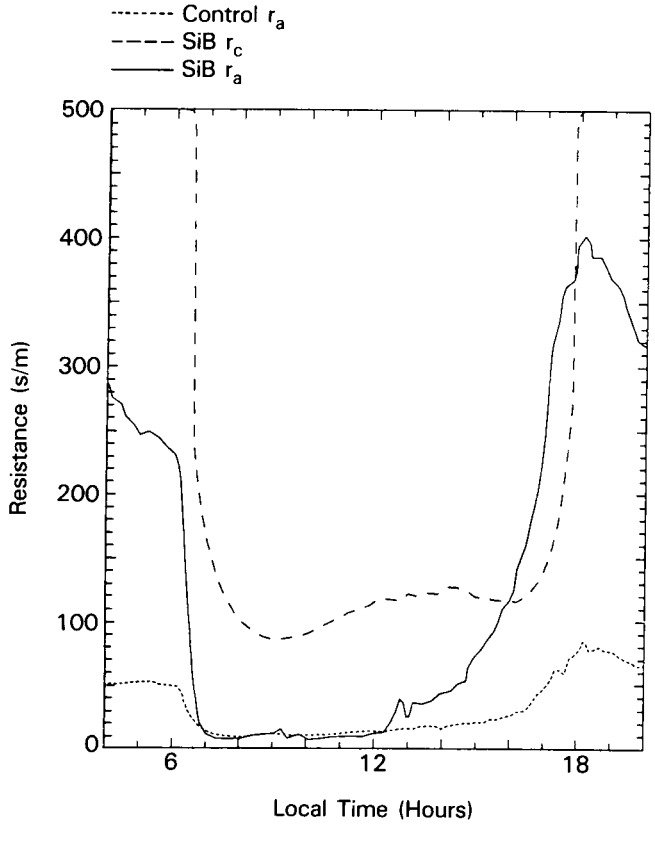

Figure 5: 30–day mean (June 15 – July 14) surface (stomatal) and aerodynamic resistances at Manaus simulated by SiB–GCM and Ctl–GCM. r_a is aerodynamic resistance; r_c is surface (stomatal) resistance for the forest canopy in SiB. There is no equivalent to r_c in Ctl–GCM.

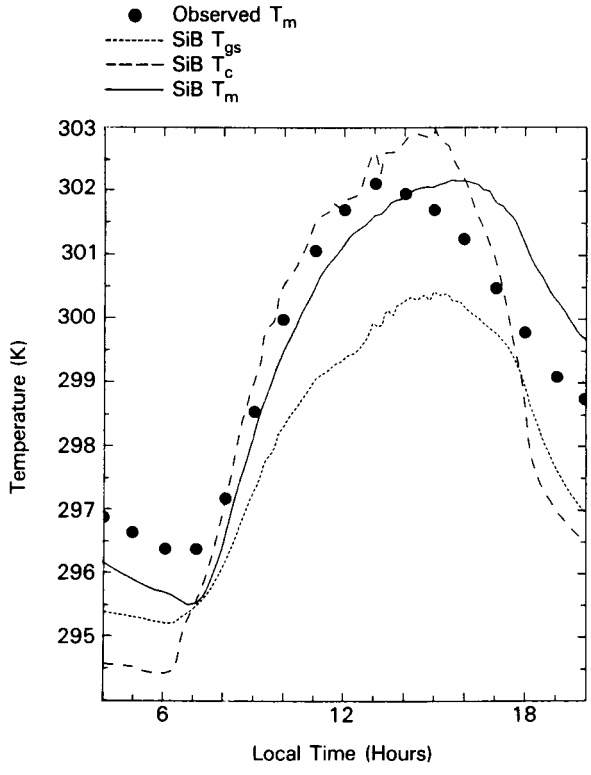

Figure 6a: 30–day (June 15 — July 14) mean surface and soil temperatures at Manaus simulated by SiB–GCM. The solid line is for the temperature at the lowest model atmospheric level, T_m (σ = 0.995) the coarse dashed line for the canopy temperature, T_c, and the dotted line is for the ground surface/cover temperature, T_{gs}. The series of solid dots represent the 30–day mean hourly air temperatures 45 m above ground (10 m above canopy top) as observed by Shuttleworth et al. (1984a) at Manaus for the period June 15, 1984 — July 14, 1984.

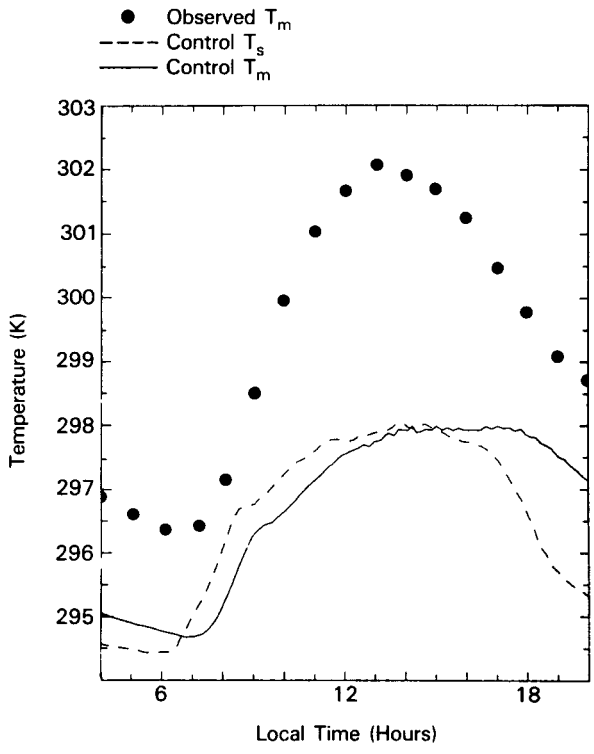

Figure 6b: 30–day (June 15 — July 14) mean surface and soil temperature at Manaus simulated by Ctl–GCM. The solid line is for the temperature at the lowest model level (σ = 0.995), T_m, and the dashed line line is for the ground surface temperature, T_s. The series of solid dots represent 30–day mean hourly air temperatures at 45 m above ground (10 m above canopy top) as observed by Shuttleworth et al. (1984a) at Manaus for the period June 15, 1984 — July 14, 1984.

resistance, r_a, estimated from eddy correlation data, frequently dropped to around 10 s/m and the mean minimum value of the canopy resistance for the tropical forest was estimated to be around 130 s/m from the flux observations. The SiB–GCM simulations of r_a and r_b + r_c concur with these observations. Additionally, a 'bump' in the diurnal course of the stomatal resistance, centered on 1100–1200 local time, may also be seen in Fig. 5. This feature corresponds to the midday depression in stomatal conductance and photosynthesis as observed in Oak shrub by Tenhunen et al. (1984) and is caused by the vegetations' response to the elevated temperatures and raised vapor pressure deficit in the canopy air space at this time of day. The reproduction of this feature indicates that the SiB–GCM is realistically simulating the coupled system of biological and near–surface meteorological processes.

Because of stomatal resistance, SiB–GCM generates more sensible heat than Ctl–GCM in most vegetated areas. This is associated with higher surface temperatures and a larger diurnal range in SiB–GCM. Figure 6a shows the SiB canopy, ground surface and the air temperature at the lowest GCM level. Figure 6b shows corresponding results for Ctl–GCM: ground surface temperature and the air temperature of the lowest atmospheric level are shown. The monthly mean air temperature 44.6 m above ground (average canopy top height is 35 m) as observed by Shuttleworth et al. (1984a,b) is shown in both figures. The observed temperature reaches 302 K with a diurnal range of about 6 K: the equivalent simulated values from SiB–GCM, 302 K and 6.5 K respectively, are comparable to the observed values and are more realistic than the values calculated by Ctl–GCM (298 K and 3 K).

The large sensible heat flux generated by SiB–GCM also helps the PBL to grow deeper and make the transport of heat, moisture and momentum flux in the PBL more efficient. Figures 7a and 7b show the calculated diurnal variation of potential temperature for the five lowest GCM levels (σ = 0.9950, 0.9815, 0.9605, 0.9205, 0.8565) in SiB–GCM and Ctl–GCM, respectively. With SiB–GCM the simulated PBL grows up to level 4 (i.e., the PBL depth is about 80 mb) and sometimes up to level 5 (150 mb). On the other hand in the Ctl–GCM simulations, PBL growth is capped at the third level which means that the PBL depth does not exceed 20 mb in this area. Martin et al. (1988) observed the PBL

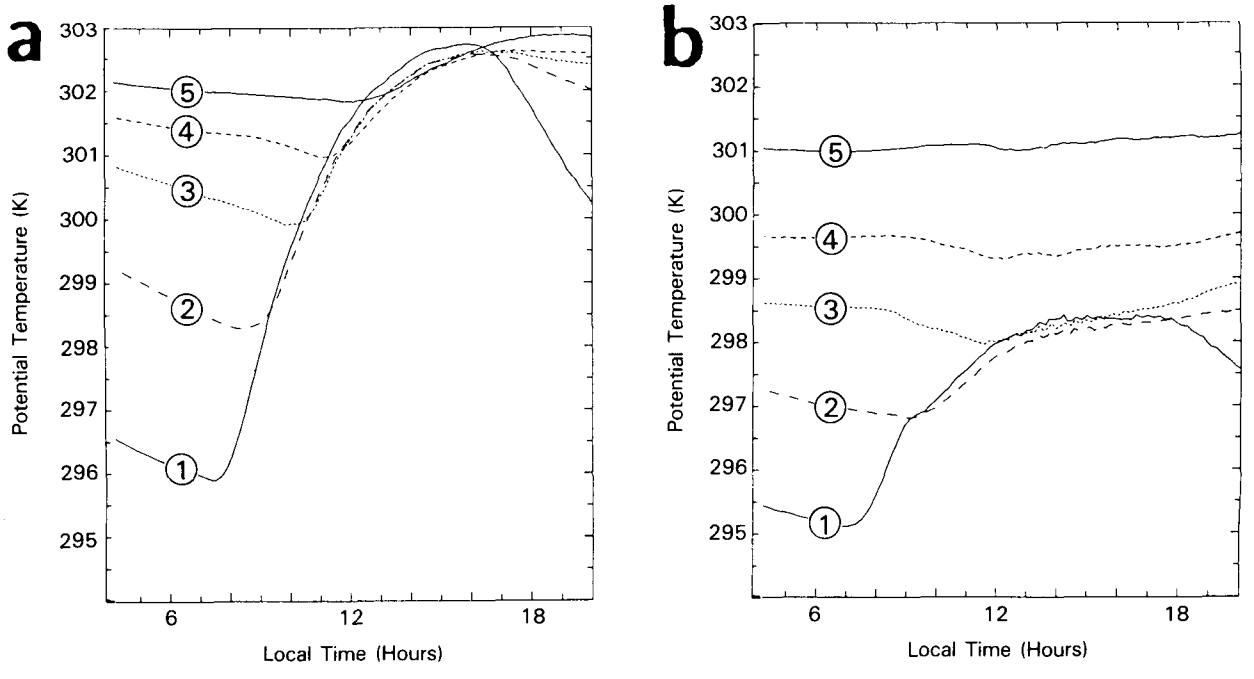

Figure 7: Simulated 30–day (June 15 — July 14) mean hourly potential temperatures for the lowest five model levels (σ — 0.9950, 0.9815, 0.9605, 0.9205, 0.8565) at Manaus. a) SiB–GCM b) Ctl–GCM

structure over the Amazonian rain forest near Manaus for the three week period, July 15 – August 7, 1985, during which the PBL depth grew to about 170 mb (1600 m) on fine days and 80 to 90 mb (800 m) on cloudy days. On the average, the maximum PBL depth was about 130 mb (1200 m) which concurs with the PBL growth simulation by SiB–GCM.

The more unstable daytime conditions associated with the SiB–GCM simulation give rise to shear stresses which are roughly double those generated by Ctl–GCM, see Fig. 8; the 30–day mean maximum daily shear stresses are 0.28 and 0.17 Pa, respectively. These figures may be compared with the friction velocity measurements reported in Shuttleworth et al. (1984a), which are equivalent to shear stress values ranging from 0.01 Pa (nighttime, dawn, dusk) to over 0.5 Pa (midday, unstable conditions). These higher shear stresses are probably associated with moderately large sensible heat fluxes, consistent with the SiB–GCM calculation.

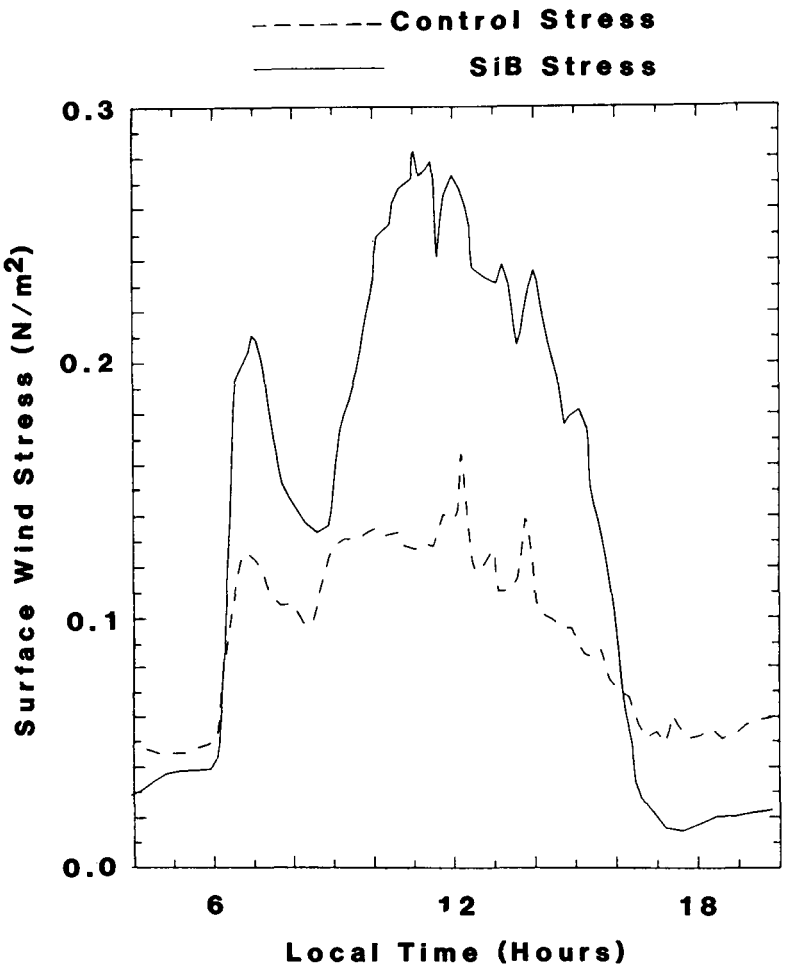

Figure 8: 30–day (June 15 – July 14) mean hourly surface wind stress at Manaus simulated by SiB–GCM (solid line) and Ctl–GCM (dashed line) for the June–July period.

Kousky (1980) reported a strong diurnal pattern of precipitation in north–east Brazil. The time of maximum precipitation differed greatly depending on the region. It is interesting to see if the GCM's generate any kind of diurnal variation in precipitation. Figure 9 shows the simulated diurnal variation of hourly precipitation rate and the observations of Shuttleworth et al. (1984a). In both simulations, precipitation is mostly convective with a strong diurnal variation. The simulated peak is in the afternoon in both cases which is not inconsistent with the observations.

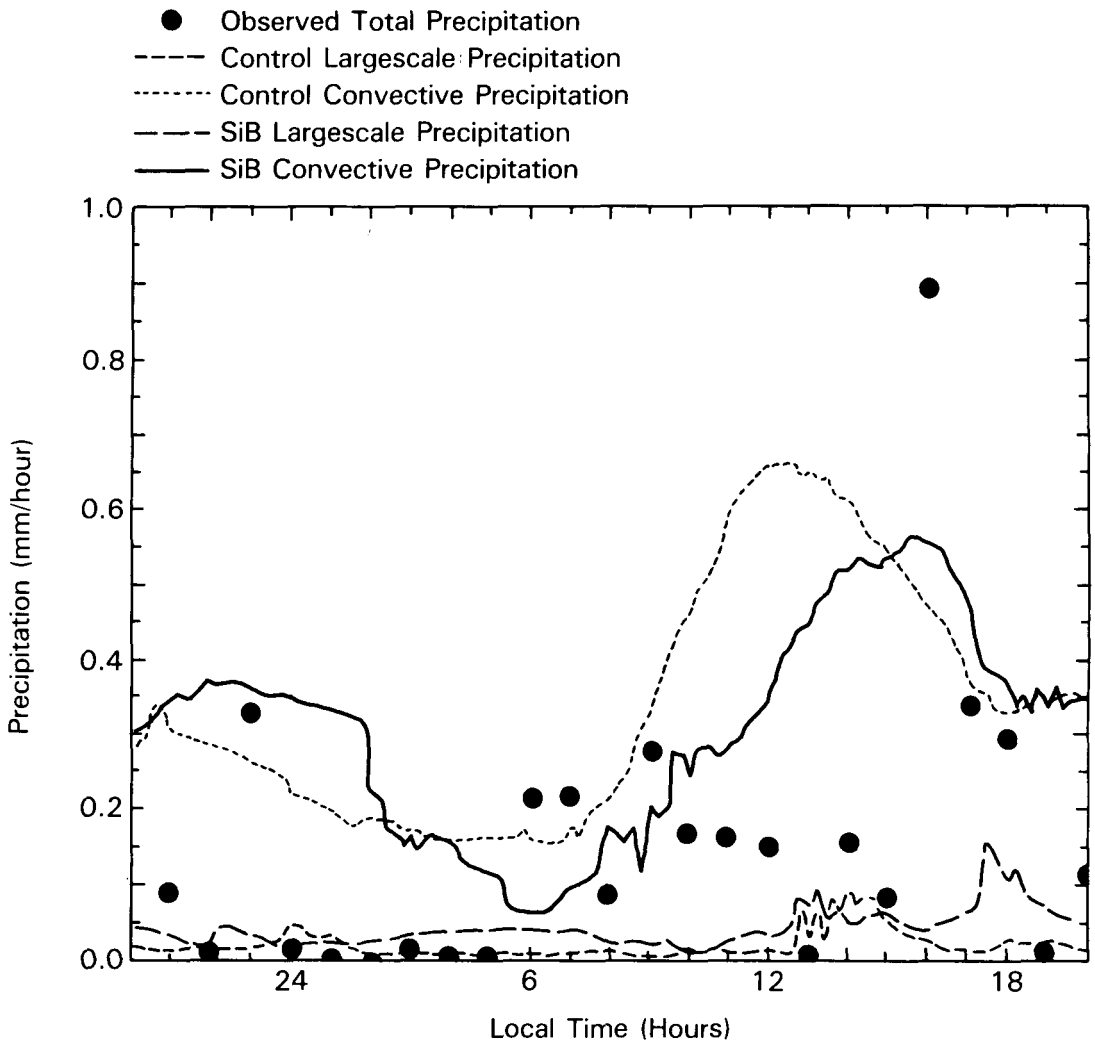

Figure 9: Diurnal variation of the 30–day (June 15 – July 14) mean precipitation simulated for Manaus by the two GCMs for the June–July period. The solid line is for convective precipitation in SiB–GCM, the coarse dashed line is for large–scale precipitation in SiB–GCM, the dotted line is for convective precipitation in Ctl–GCM and the fine dashed line is for large–scale precipitation in Ctl–GCM. The solid dots are for equivalent observations by Shuttleworth et al. (1984a).

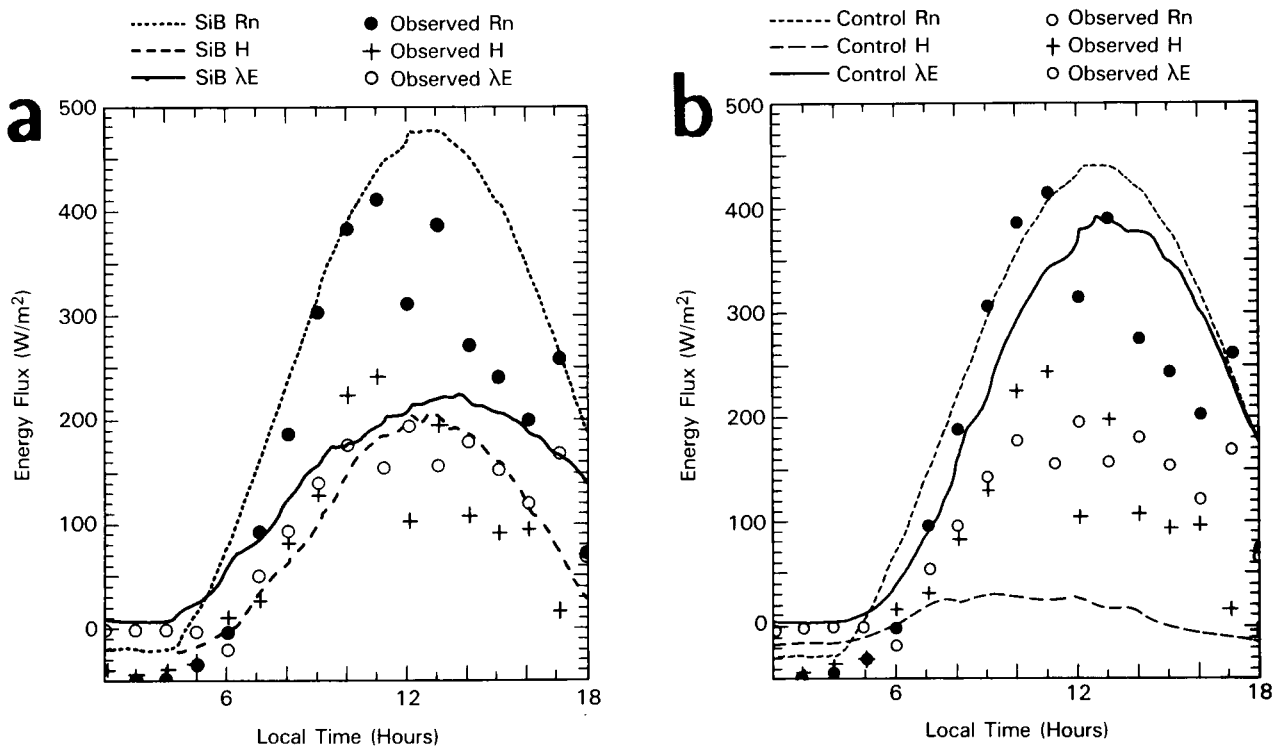

Figure 10: 30–day (June 15 – July 14) mean surface energy balance for an evergreen coniferous forest grid area (98° W, 55° N) in central Canada as simulated by SiB–GCM. The points marked on the figure are for equivalent quantities as measured by McNaughton and Black (1973) over a Douglas fir forest in British Columbia on July 20, 1970. a) SiB–GCM b) Ctl–GCM

4.1.2 Coniferous Forest

Figure 10a (10b) shows the SiB–GCM (Ctl–GCM) simulations of latent and sensible heat flux for a grid point in Canada (98° W, 55° N); this point is represented as evergreen coniferous forest in SiB–GCM. As before, the means for the first 30 days (June 15 – July 14) of the Northern Hemisphere summer simulation are shown. Estimated fluxes for one day at a coniferous forest site in Western Canada calculated from observations by McNaughton and Black (1973) are shown in both figures. On five other days in July (1970) the observed net radiation, latent and sensible heat fluxes were larger but the Bowen ratio was always around one during the day. The simulated Bowen ratio in SiB–GCM is also very close to unity during the day whereas in Ctl–GCM it is almost zero.

4.1.3 Cultivated Area, Central Europe

Figure 11a (11b) shows the latent and sensible heat fluxes for a grid point at (17° E, 49° N), a cultivated area in Central Europe, as simulated by SiB–GCM (Ctl–GCM). Observed fluxes recorded over a barley field at Ruthe in West Germany on June 20 – 22,

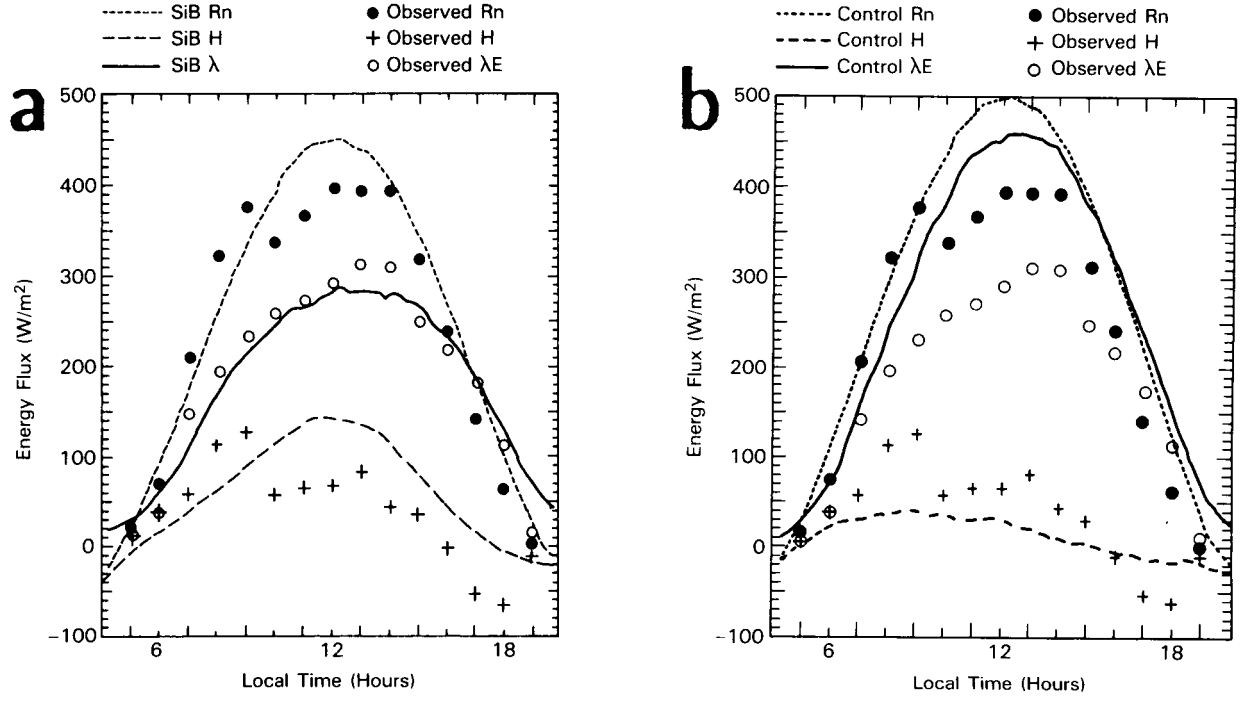

Figure 11: 30–day (June 14 – July 15) mean surface energy balance for a cultivated grid area (17° E, 49° N) in central Europe. The points marked on the figure are for equivalent quantities as measured by van der Ploeg et al. (1980) over a barley field on 22 June 1977. a) SiB–GCM b) Ctl–GCM

1979 are also shown (van der Ploeg et al., 1980). As in the case of the Amazon rain forest and the evergreen coniferous forest in Canada, Ctl–GCM generates far too much latent heat flux whereas the time series of latent heat flux in SiB–GCM compares well with observations. Figure 12 shows the surface albedo simulated by SiB–GCM and the prescribed Posey and Clapp (1964) (Ctl–GCM) albedo for the region; observations from a wheat field 50 km from Ruthe, West Germany are also shown. It appears that SiB–GCM generates a realistic albedo while the Ctl–GCM value is too low and does not vary with time.

4.1.4 Sahara Desert

The diurnal variation of ground surface temperature at a Saharan grid point (0° E, 23° N) is shown in Fig. 13. SiB–GCM has a higher surface albedo which contributes to the lower maximum ground surface temperature compared to Ctl–GCM.

Susskind (pers. comm.) retrieved daytime (14:30 LT) and nighttime (2:30 LT) ground surface temperatures from satellite data. The estimated daytime and nighttime temperatures around (0° E, 23° N) for July, 1979 were 324 K and 296 K, respectively, which

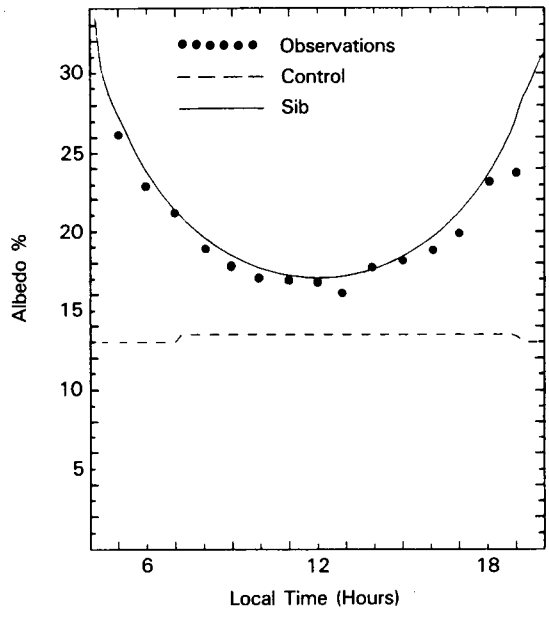

Figure 12: 30—day (June 15 — July 14) mean surface albedo at the West German grid point as simulated by SiB—GCM (solid line) and Ctl—GCM (dashed line). The crosses represent observed fluxes for a wheat field at Volkenrude, West Germany as reported in van der Ploeg et al. (1980) for 20—21 June, 1979.

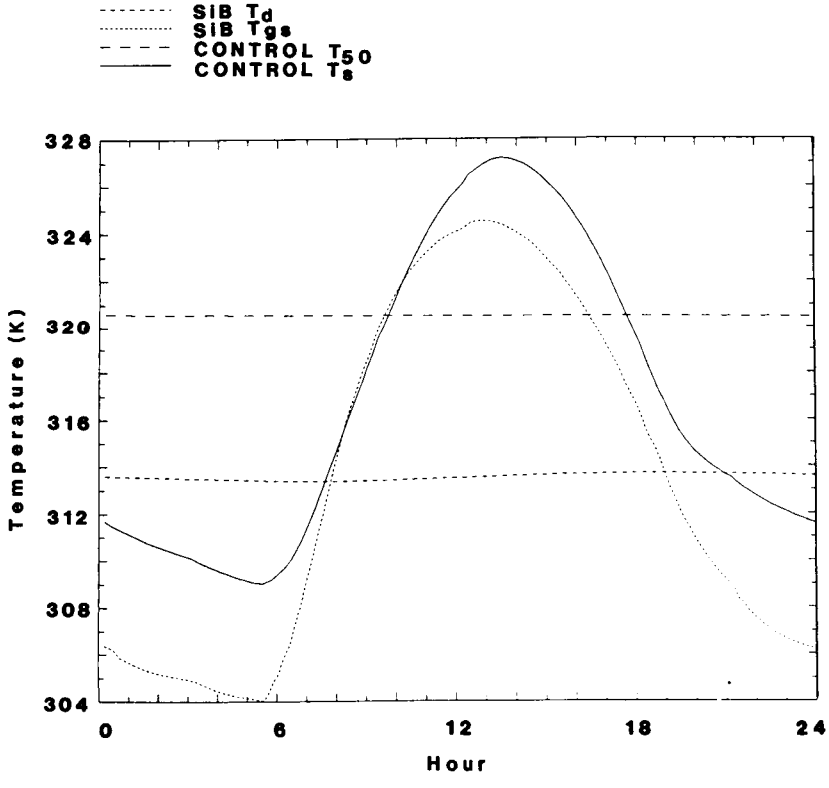

Figure 13: 30—day (June 15 — July 14) means of the diurnal variation of the ground surface temperature for a grid point in the Sahara Desert (0° E, 23° N) as calculated by SiB—GCM and Ctl—GCM. T_d and T_{gs} are the SiB ground surface and deep soil temperatures, respectively. T_{50} and T_s are the deep soil (50 cm) and surface temperatures for the control model (Ctl—GCM), respectively.

gives a diurnal range of 28 K. These may be compared with the equivalent simulated daytime ground surface temperatures of 326.5 K in Ctl–GCM and 323 K in SiB–GCM. The nighttime temperatures, 310 K in Ctl–GCM and 305 K in SiB–GCM, seem to be too high compared with observations even when uncertainties in the retrieval procedure are taken into account. One possible explanation is that the fixed zonal mean clouds in the GCMs reduces the amount of nocturnal cooling over the deserts. Excessive downward sensible heat flux from the atmosphere to the surface or heat conducted from the deep soil layer may also contribute to the higher nighttime ground surface temperatures.

4.2 Time tendency of regional mean energy and moisture budgets.

Area–averaged budget analyses were made for 50 days (June 15 – August 4) of summer simulations by both GCMs to find out how the regional energy and moisture budgets changed during the course of the numerical simulations. Four continental regions were selected: the Amazon Basin, Central and Eastern U.S.A., Asia, and the Sahara desert (Fig. 2).

In SiB–GCM, the Amazon basin is uniformly covered by tropical rain forest; the Central and Eastern U.S. consists mainly of cultivated land, grassland and some mixed forest; the Asian region consists of heterogeneous land cover including tropical rain forest, cultivated land and desert; and the Sahara desert consists of sand with a very sparse shrub cover.

4.2.1 Energy Budget

The daily mean surface energy budget of SiB–GCM (Ctl–GCM) for the Amazon Basin is shown in Fig. 14a (14b) and is summarized in Table 1. The assumption of a fixed zonal mean climatological cloudiness and ozone distribution results in very similar surface insolations for the two models. This mean value, 210 W/m^2, is close to, but a little larger than the July climatological value, 195 W/m^2, as given by Budyko (1974), but these comparisons should not be extended too far in view of the prescribed cloudiness used in the GCMs. There is some difference between the net solar radiation fluxes calculated by the two GCMs because of the different albedos used; 12% in SiB–GCM and 7.7% (Posey and Clapp, 1964) in Ctl–GCM. This albedo difference results in a 10 W/m^2 or a 5% difference in the net radiation.

The striking improvement of SiB–GCM over Ctl–GCM is shown in the partition of net radiation into latent and sensible heat fluxes. In the Ctl–GCM simulation, almost all of the net radiation is used for evaporation and the sensible heat flux is negligible. In SiB–GCM, 84% of the net radiation goes to latent heat flux which gives a Bowen ratio of 0.21. This difference results from the different formulations used to calculate evapotranspiration in the two GCMs, see Sec. 3.6.

The latent heat fluxes, 130 W/m^2 (SiB–GCM) and 162 W/m^2 (Ctl–GCM), correspond to 4.5 mm/day (SiB–GCM) and 5.5 mm/day (Ctl–GCM) of evapotranspiration. Salati (1987) summarized published estimates of the mean annual evapotranspiration rate for the entire Amazon Basin to give a figure in the range of 3.1 to 4.0 mm/day. If we take the uncertainty of this estimate and seasonal variation into consideration, the evaporation rate given by the SiB–GCM, 4.5 mm/day, is in better agreement with the estimates obtained from observations than Ctl–GCM.

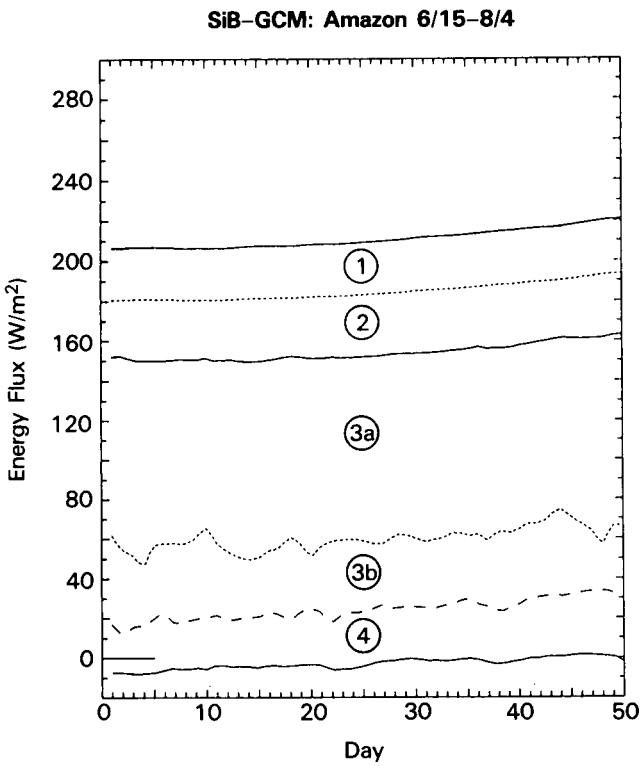

Figure 14a: The daily mean surface energy budget calculated by SiB–GCM for the Amazon Basin area shown in Fig. 2 for a 50–day summer simulation run. Each energy *band* represents:

1–solar radiation reflected by the surface
2–net loss by longwave radiation
3a–latent heat flux by transpiration and bare soil evaporation
3b–latent heat flux by interception loss
3a+3b–total latent heat flux
4–sensible heat flux

The top solid line represents the total downward solar radiation flux, the second dotted line represents the net downward solar radiation, the third solid line represents the net downward radiation and the bottom solid line represents heat transferred to soil by conduction. If this lowest line is negative, the heat transfer is from the soil to the air.

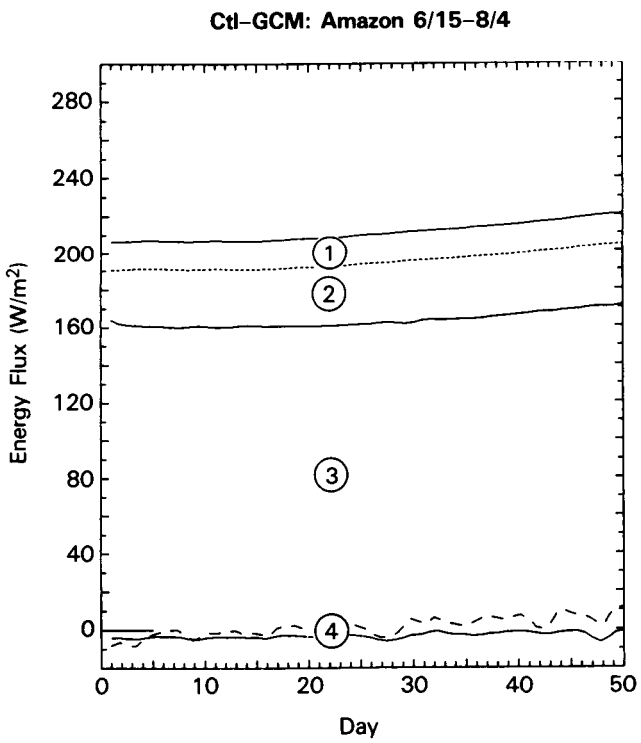

Figure 14b: The daily mean surface energy budget calculated by Ctl–GCM for the Amazon Basin for a 50–day summer (June 15 – July 14) simulation run. Each energy *band* represents:

1–solar radiation reflected by the surface
2–net loss by longwave radiation
3–latent heat flux
4–sensible heat flux

the meaning of each line is the same as in Fig. 14a.

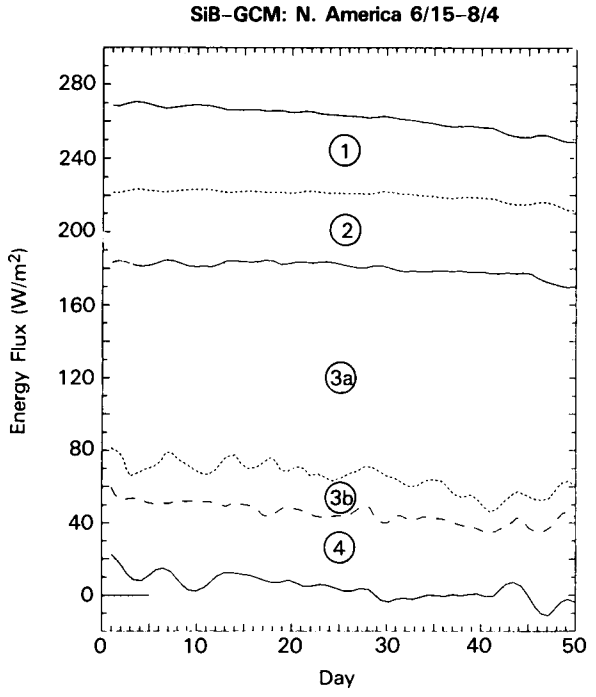

Figure 14c: The same as Fig. 14a except for central and eastern U.S.

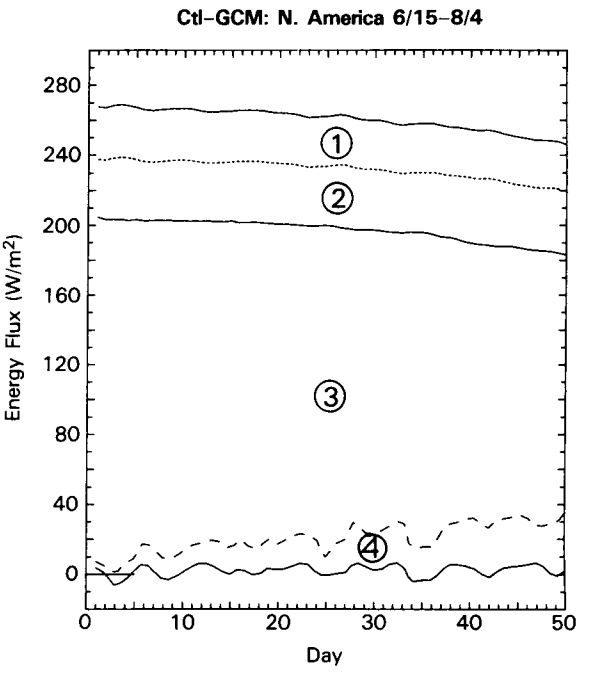

Figure 14d: The same as Fig. 14b except for central and eastern U.S.

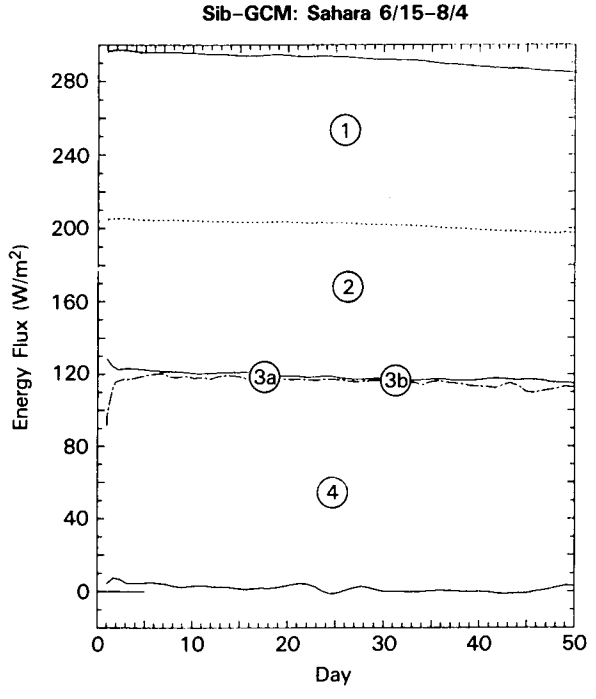

Figure 14e: The same as Fig. 14a except for the Sahara Desert.

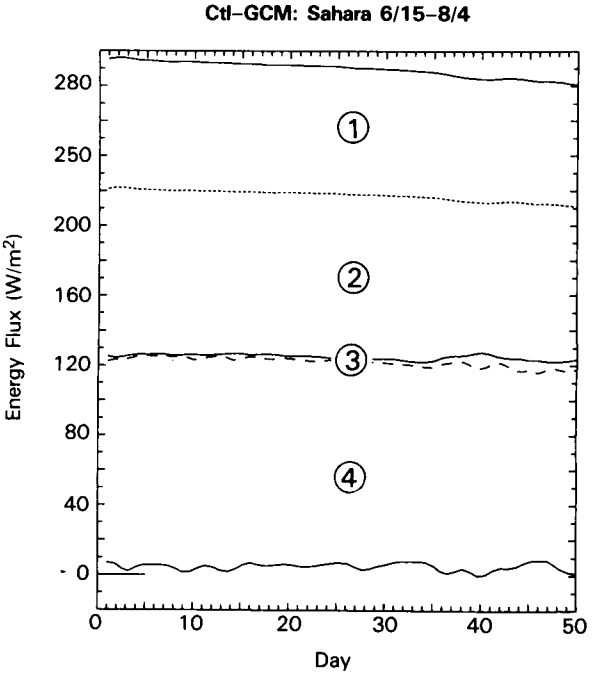

Figure 14f: The same as Fig. 14b except for the Sahara Desert.

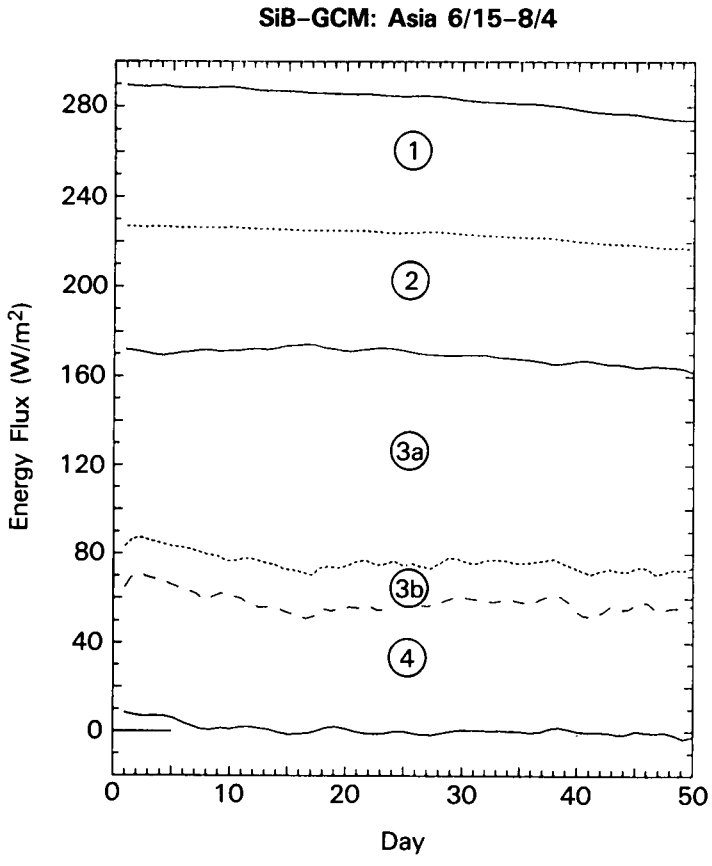

Figure 14g: The same as Fig. 14a except for Asia.

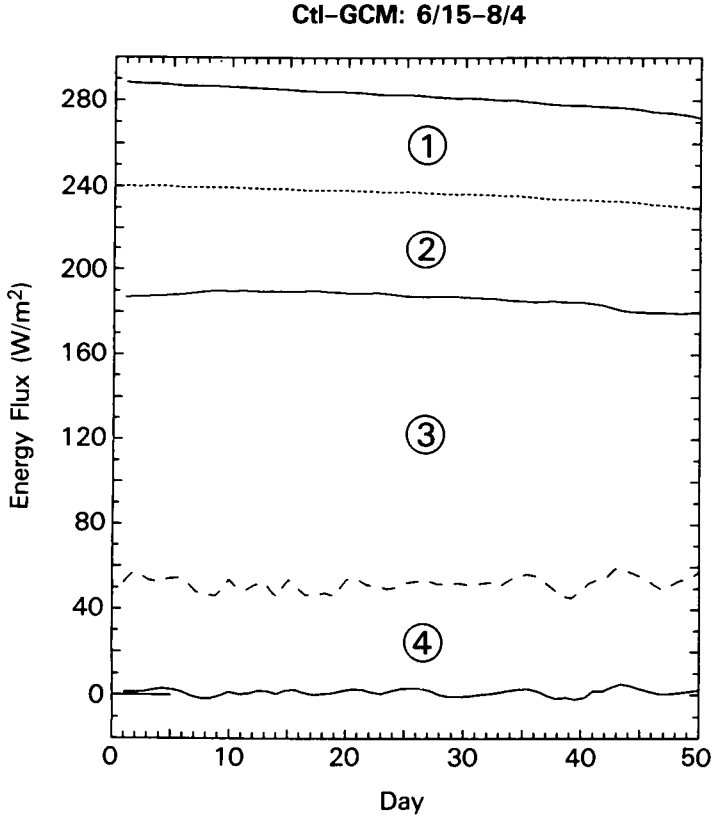

Figure 14h: The same as Fig. 14b except for Asia.

Table 1 The mean surface energy budget as calculated by **(a)** Ctl–GCM, and **(b)** SiB–GCM for the four regions outlined in Fig. 1: Amazon Basin, Central and Eastern United States, Sahara Desert and Asia. The means are for the 50–day (June 15 – August 4) summer simulations in all cases. The symbols used in the columns represent the following fluxes (W/m^2).

S	=	Insolation
$(1-\alpha)S$	=	net short wave (absorbed by the surface).
L_n	=	net longwave (absorbed by the surface).
R_n	=	net radiation, available energy.
λE_T	=	Transpired latent heat flux (SiB only).
λE_I	=	interception loss plus soil evaporation latent heat flux (SiB only).
λE	=	Total latent heat flux (sum of λE_T and λE_I in SiB).
H	=	sensible heat flux.
G	=	ground heat flux

(a) Mean (50–day) surface energy budget calculated by Ctl–GCM.

REGION	S	$(1-\alpha)S$	L_n	R_n	λE_T	λE_I	λE	H	G
Amazon	211.1	194.8	–31.5	163.3	—	—	161.8	4.6	–3.1
Central & Eastern U.S.	260.2	231.8	–34.9	196.9	—	—	176.4	18.4	2.1
Sahara Desert	289.6	217.4	–92.4	125.0	—	—	3.1	117.1	4.8
Asia	281.9	236.6	–50.1	186.5	—	—	134.5	50.9	1.1

(b) Mean (50–day) surface energy budget calculated by SiB–GCM.

REGION	S	$(1-\alpha)S$	L_n	R_n	λE_T	λE_I	λE	H	G
Amazon	210.9	184.7	–30.6	154.1	94.2	35.7	129.9	27.2	–3.0
Central & Eastern U.S.	261.8	220.2	–39.9	180.3	114.9	20.1	135.0	41.1	4.2
Sahara Desert	292.2	202.0	–83.1	118.9	3.36	.04	3.4	113.8	1.7
Asia	283.5	223.4	–54.0	169.4	93.2	18.0	111.2	57.4	0.8

The time series of interception loss for the Amazon as calculated by SiB–GCM is shown in Fig. 14a and in Table 1. The time–averaged value, 36 W/m^2, represents 28% of the total evapotranspiration. Shuttleworth et al. (1984a) reported an equivalent value of 30% for their measurements taken at a site outside Manaus. An annual mean value of 35% was reported in Salati (1987) for a small basin (25 km^2) 60 km north of Manaus. Salati (1987) also mentions the report of Franken et al. (1982) which gives a value of 33% for a one–year period at another site 40 km from Manaus. In general then, the interception loss rate calculated by SiB–GCM seems to be realistic when compared to the observations. This must be partly due to the formulation used to account for the hydrological effects associated with the non–uniform spatial distribution of convective rainfall (Appendix C).

Figures 14c and 14d show the daily mean surface energy budget for the central and eastern U.S. region. The calculated downward solar radiation at the surface is around 260 W/m^2 which is a bit less than the climatological value of 275 W/m^2 given by Budyko (1974) and Sellers (1965). The small difference in net radiation, 20 W/m^2, comes partly from the higher albedo in SiB–GCM versus Ctl–GCM, 16% vs 11%, and partly from the increased net longwave radiation flux associated with the higher surface temperature and drier PBL in SiB–GCM. As in the case of the Amazon Basin, the marked difference between the SiB–GCM and Ctl–GCM results is to be found in the partition of the net radiation into sensible and latent heat fluxes: The Bowen ratio is 0.3 in SiB–GCM and 0.1 in Ctl–GCM.

In Ctl–GCM, there is an increase in the sensible heat flux and a decrease in the latent heat flux toward the end of the 50–day summer simulation which is a result of a progressive reduction in the prescribed climatological soil moisture content. Figure 16b shows how the Ctl–GCM soil moisture was decreased from 0.88 to 0.45 over the 50 days. In the parallel SiB–GCM run, the equivalent (prognostic) soil wetness (Fig. 16a) decreased very slowly, changing from 0.70 to 0.65 in 50 days. The main reason for this relatively slow change in soil moisture is that SiB has a greater soil moisture capacity than the bucket model: the total depth of the moisture carrying zones is typically 1490 mm, porosity is 0.46 and the initial soil wetness is 0.7. These values combine to give 480 mm as an initial soil moisture content for SiB–GCM of which some 300 mm is available for evapotranspiration. This is twice the maximum soil water holding capacity (150 mm) of the UCLA/GLA GCM of Randall et al. (1985) and the GFDL GCM as described by Miyakoda and Sirutis (1986).

Figures 14e and 14f show the daily mean energy budget for the Sahara Desert. The total insolation in both GCM's decreases from 295 W/m^2 to 280 W/m^2 over the course of the 50–day run due to the decrease in the solar inclination. The net solar radiation is 217 W/m^2 in Ctl–GCM and 202 W/m^2 in SiB–GCM. The 15 W/m^2 difference is due to the difference in surface albedo which is 31% in SiB–GCM and 25% in Ctl–GCM. However, this difference in the net solar radiation is approximately compensated by differences in the net terrestrial radiation loss so the resulting net radiation is almost the same; 125 W/m^2 in Ctl–GCM and 119 W/m^2 in SiB–GCM. It is interesting to note that the net radiation in this region comprises only 42% of the incoming solar radiation as opposed to 70–80% for the Amazon basin and U.S.; this is due to the high surface albedo and low atmospheric humidity in the desert regions. Both models give very low evapotranspiration rates in this area so almost all of the net radiation is returned to the atmosphere as sensible heat flux.

Figures 14g and 14h show the daily mean energy budget for the Asian region indicated in Fig. 2. Because this region consists mainly of desert with relatively little vegetated land, the conspicuous change of surface energy partition encountered in the

Amazon Basin and in Central and Eastern U.S.A. is not seen so clearly here, but there is some increase in the Bowen ratio in SiB–GCM.

4.2.2 Hydrological Cycle

The simulated hydrological balance of the Amazon basin is shown in Figs. 15a and 15b. The precipitation rate is 6 mm/day in SiB–GCM and 7 mm/day in Ctl–GCM. From the climatological precipitation chart (Fig. F2d of Jaeger, 1976) we see that the northern half of the Amazon basin is wet and the southern half is dry in summer. If an area average is taken, we get 4–5 mm/day for the climatological rainfall rate in June–July for the entire Amazon Basin. Compared with this observed value, both GCM's, especially Ctl–GCM, give more precipitation. The 1 mm/day decrease in the SiB–GCM versus the Ctl–GCM precipitation rate corresponds to the reduction in the SiB–GCM evaporation rate. The same situation holds in North America and Asia. In these regions, the rainfall over land seems to be directly affected by the regional evapotranspiration rate.

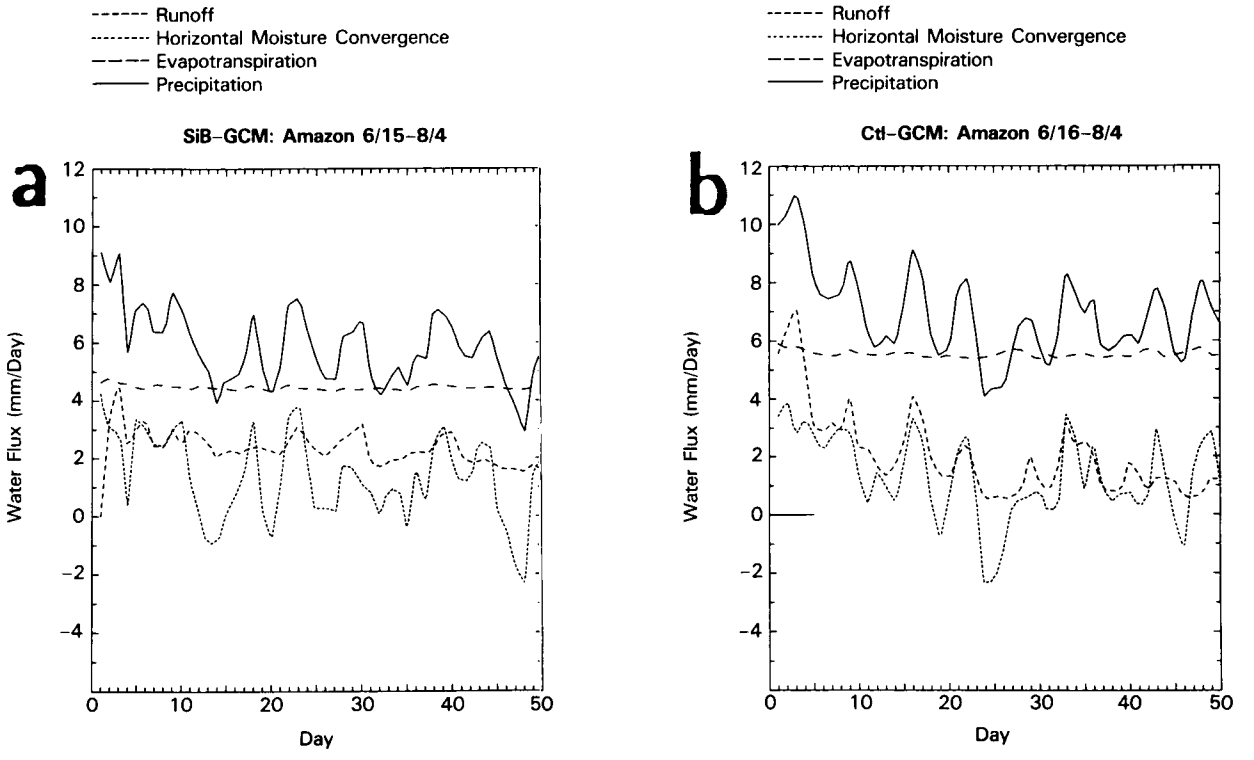

Figure 15: The daily mean moisture budget calculated by SiB–GCM in the Amazon Basin for the 50–day summer (June 15 — July 14) simulation run. The solid line is for precipitation, the coarse dashed line is for evaporation, the fine dashed line is for runoff and the dotted line is for the atmospheric horizontal moisture convergence. All values are in mm/day.
a) SiB–GCM b) Ctl–GCM

From Figs. 15a and 15b, we see that the precipitation exceeds evaporation by 1.5 mm/day on the average, with the difference made up by large scale horizontal moisture convergence. This advected moisture contributes about 25% (SiB–GCM) and 20% (Ctl–GCM) to the total rainfall in the region.

The runoff rate in SiB–GCM is 2.5 mm/day on the average. This amount exceeds the difference between the rainfall rate and evaporation rate by 1 mm/day and implies that the total soil moisture content in SiB is steadily decreasing (see Fig. 16a). Oltman et al. (1964) estimated the annual mean outflow from the Amazon basin to be about 2.5 mm/day from observations of the Amazon river velocity profile and stage. There is a fairly considerable annual variation in this quantity, but the June to August period appears to bracket this mean value while showing a steadily decreasing outflow rate. This decrease in the outflow is consistent with a fall in the average soil moisture content for the basin as calculated by SiB.

In Ctl–GCM, runoff is generated by the difference between rainfall and evaporation when the soil is saturated. When soil moisture was predicted (see below) it decreased significantly, but because soil moisture in this main Ctl–GCM run was interpolated from monthly climatology, the soil wetness in the Amazon basin was almost always at the saturated value, see Fig. 15b.

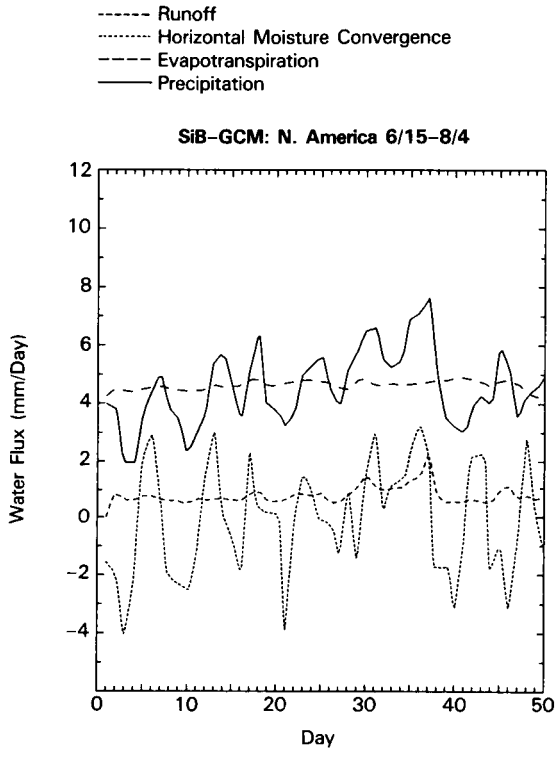

Figure 15c: The same as Fig. 15a except for central and eastern U.S.

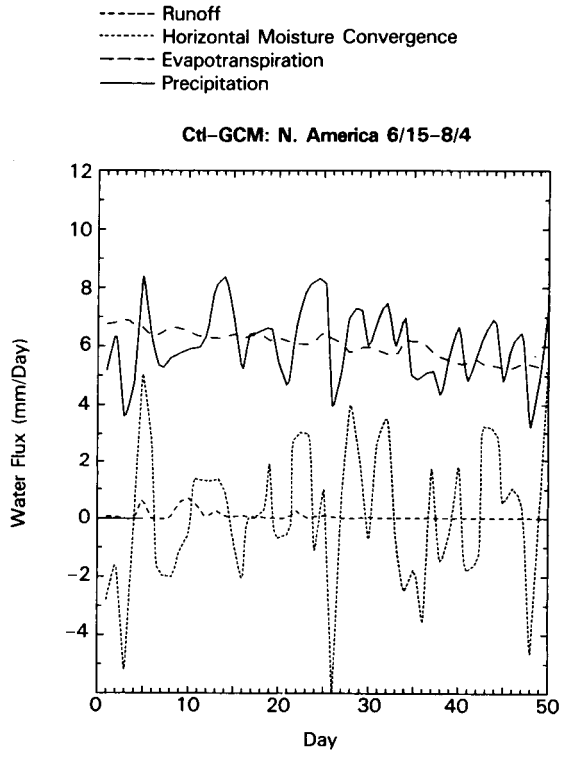

Figure 15d: The same as Fig. 15b except for central and eastern U.S.

The calculated moistures budget for the U.S. region are presented in Figs. 15c and 15d. In SiB–GCM (Ctl–GCM) the calculated precipitation rate is 4.7 mm/day (6.2 mm/day) and the evaporation rate is 4.5 mm/day (6.0 mm/day). In both cases, the time–mean of the horizontal convergence of moisture by the large scale atmospheric circulation is very small. This is supported by the analysis of Rasmusson (1968) who computed the horizontal moisture convergence over the same Central and Eastern U.S. region for each month of the year from 5 years of radiosonde data. He estimated the surface evaporation rates to be 2.7 mm/day and 3.1 mm/day in June and July, respectively, whereas the horizontal moisture convergences were very small for the same period. The evapotranspiration rate obtained from the simulations exceeds the estimates of Rasmusson (1968) by 50% in SiB–GCM and by 100% in Ctl–GCM. (The corresponding evapotranspiration rate of 4.5 mm/day in SiB–GCM seems close to the values observed for a forest without soil moisture stress: 5 mm/day is given by Swift (1975) as the June–July mean for a deciduous forest in the southern Appalachians and 4 mm/day is given by Luxmoore (1983) as the July–September mean for a deciduous forest in the Eastern U.S.).

From the hydrological analyses of the Amazon and North American regions, we note that the higher precipitation rates over land in Ctl–GCM were associated with higher evapotranspiration rates over the same area and not from an increase in horizontal moisture convergence. This leads us to suggest that the precipitation over these regions is in large part controlled by the transpiration there. In order to check this hypothesis, another SiB–GCM experiment was performed with a reduced initial soil moisture content.

A 30–day SiB–GCM run was performed using the same initial conditions as the 50–day summer SiB–GCM run except that in North America the initial soil wetness was set to 0.45 wherever it exceeded this value. Figure 15g shows the moisture budget for the central and eastern U.S. region as calculated for this run. Once again, the time–averaged horizontal moisture convergence is almost zero and the reduced evapotranspiration rate, down from the 4.5 mm/day of the original 50–day SiB–GCM run to less than 3.5 mm/day in this reduced soil moisture case, is reflected in a corresponding 1 mm/day decrease in the time–averaged precipitation rate. This result strongly supports the hypothesis that the evapotranspiration and rainfall rates are tightly coupled in this region during the summer months.

Returning to the original summer run, the runoff generated for the U.S. region by the SiB–GCM is 1 mm/day and is not in equilibrium with the precipitation rate minus the evaporation rate. As in the case of the Amazon Basin the runoff is caused by the drainage from the recharge zone of the SiB soil moisture model.

The moisture budget for Asia for the summer run is shown in Figs. 15e and 15f. The precipitation rate in SiB–GCM (Ctl–GCM) is 7.2 mm/day (8.5 mm/day), evapo–transpiration 3.8 mm/day (4.7 mm/day), horizontal moisture convergence 3.4 mm/day (3.8 mm/day) and runoff 3.0 mm/day (1.1 mm/day). The decrease in precipitation (1.3 mm/day) in SiB–GCM compared with that in Ctl–GCM comes partly from a decrease in the evapotranspiration rate (0.9 mm/day) and partly from a decrease in the horizontal moisture convergence (0.4 mm/day). The main characteristic to note for this region is that horizontal convergence is calculated to be a significant contributor to the precipitation in both GCM's for this region.

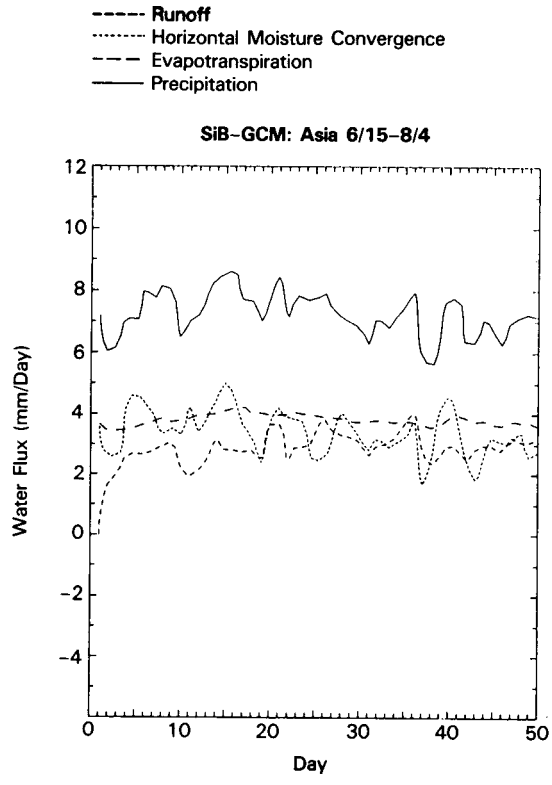

Figure 15e: The same as Fig. 15a except for Asia.

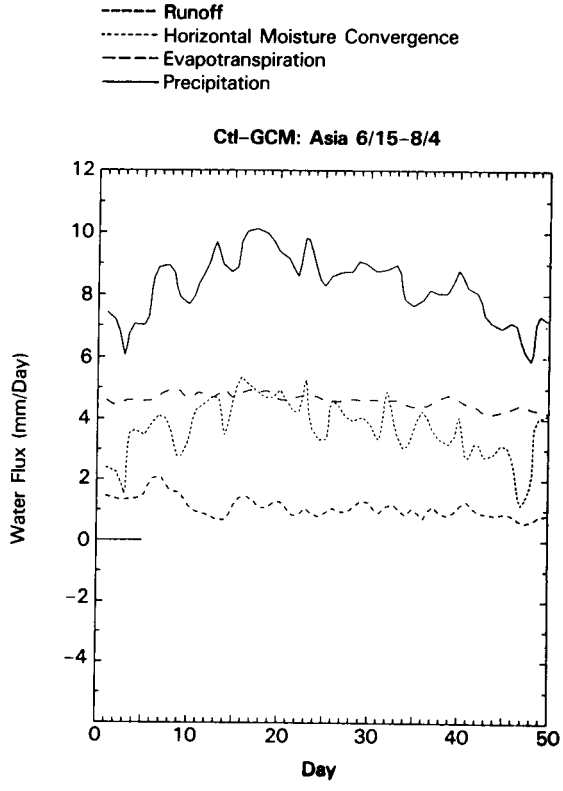

Figure 15f: The same as Fig. 15b except for Asia.

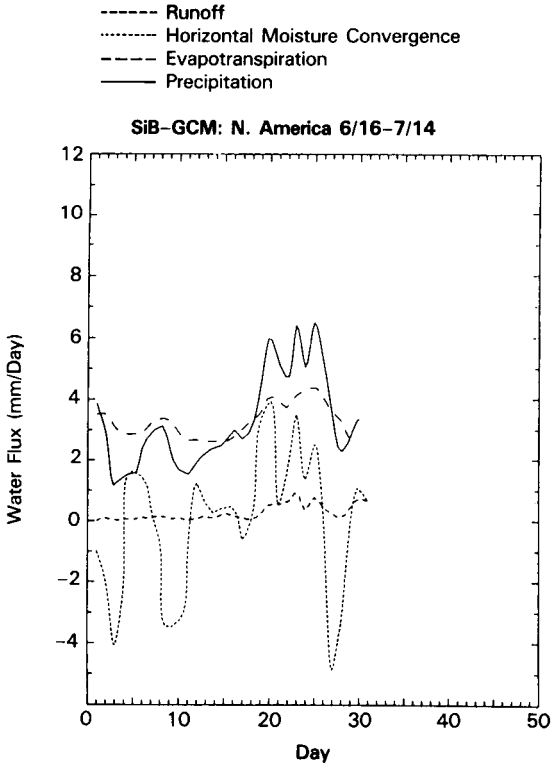

Figure 15g: The daily mean moisture budget as calculated by SiB–GCM for 30 days (June 15 – July 14) in the eastern and central U.S. where the initial soil wetness was limited to a maximum of 0.45. Other conditions and symbols are the same as for the 50–day summer SiB–GCM simulation (Fig. 15a).

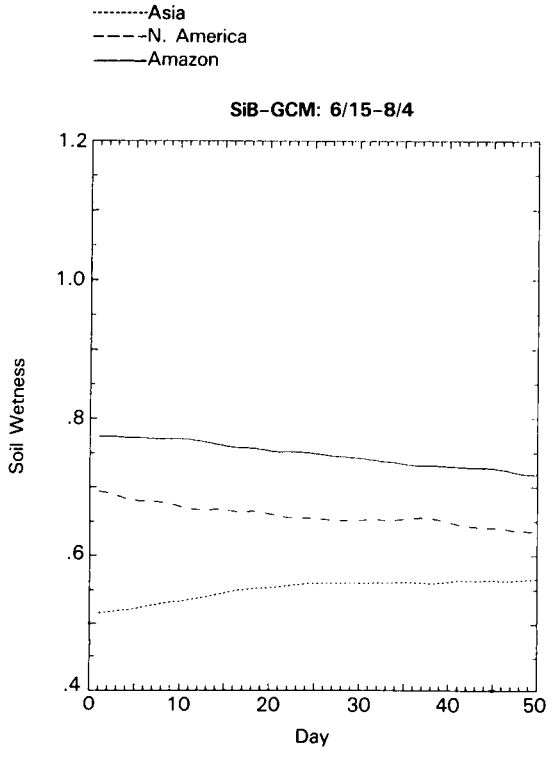

Figure 16a: The evolution of the soil wetness calculated by SiB–GCM during a 50–day summer (June 15 – August 4) simulation run. The depth–weighted average of the wetnesses of the surface zone, root zone, and recharge zone was taken. The solid line is for the Amazon basin, the dashed line is for the central and eastern U.S. region and the dotted line is for the Asia region; see Fig. 2.

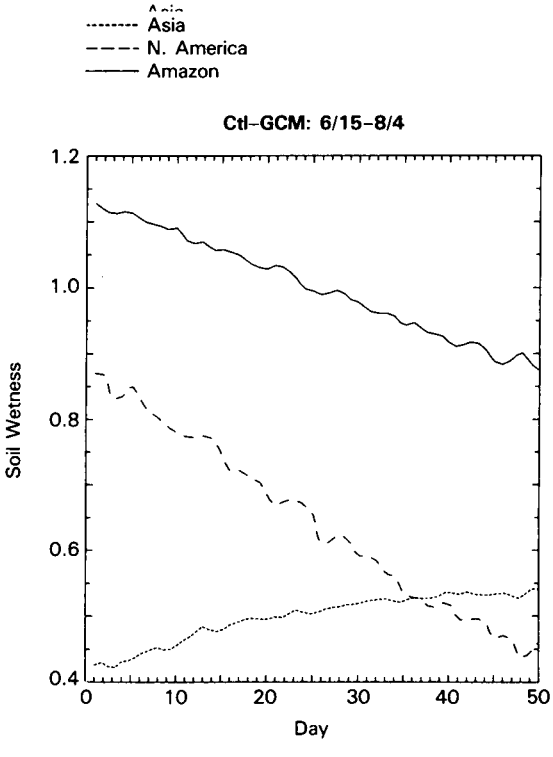

Figure 16b: The same as Fig. 16a except for Ctl–GCM. Here the time–evolution of soil wetness follows the prescribed climatology of Willmott et al. (1985). The soil wetness in Ctl–GCM is derived by dividing soil moistures by 150*0.75 mm, three quarters of field capacity. Soil wetnesses exceeding 1.0 are set to 1.0 in the GCM.

Because runoff is less than precipitation minus evaporation in SiB–GCM, the soil moisture in the region increases slowly from 0.45 to 0.50 during the run (Fig. 16a). At the same time the climatological soil moisture prescribed in Ctl–GCM increases from 0.43 to 0.54 (Fig. 16b).

Lastly, it will be remembered that a decision was made early in the study to continuously update the soil moisture content in Ctl–GCM in line with the climatological estimates of Willmott et al. (1985). An additional 30–day Ctl–GCM run was performed in which the soil moisture was predicted and updated by the model. Figure 16c shows the predicted time evolution of soil moisture which may be directly compared with Fig. 16b. It may be seen that the predicted soil moisture decreases more rapidly in the Amazon region, but more slowly in the central and eastern U.S. as compared with the imposed climatology.

In Figs. 16b and 16c, the differences between the simulated and climatological time–series of soil moisture are due to regional differences in the precipitation–evaporation ratios as simulated by Ctl–GCM and calculated by Willmott et al. (1986). However, the difference in the wetness values associated with the prognostic and climatological soil moisture fields was comparatively small and so the difference between the global fields of evapotranspiration and sensible heat flux produced by the two Ctl–GCM runs was slight; at day 30, the version with the predicted soil moisture gave rise to a sensible heat flux of only 10 W/m^2 less over the U.S. than that obtained with the climatological soil moisture field. There was virtually no difference in the heat flux fields calculated for the Amazon by the two Ctl–GCM runs at this time.

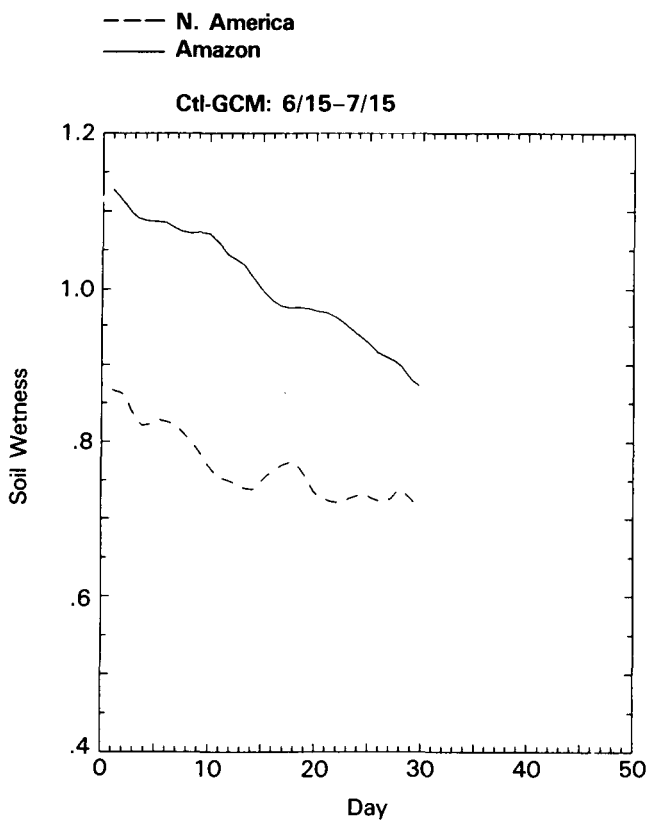

Figure 16c: 30–day (June 15 – July 14) time–series of soil moisture *predicted* by the Ctl–GCM for a summer circulation. This soil moisture evolution may be compared directly with the prescribed climatology shown in Fig. 16b.

4.2.3 Soil Heat Conduction and Temperature

Figure 17a (17b) shows the area–averaged ground surface temperature and deep soil temperature (soil temperature at 50 cm depth) in SiB–GCM (Ctl–GCM) for the four regions. In Ctl–GCM, the displayed surface temperature was derived from the daily mean upward longwave radiation flux at the surface; it was found that this did not differ much from the daily mean of the surface temperature. The deep soil temperature in SiB–GCM shows some initial adjustment due to uncertainties in its initialization; however, analysis of the surface energy budget showed that the daily mean heat conduction into or out of the soil was usually less than 10 W/m² and so was not critical to the surface energy budget.

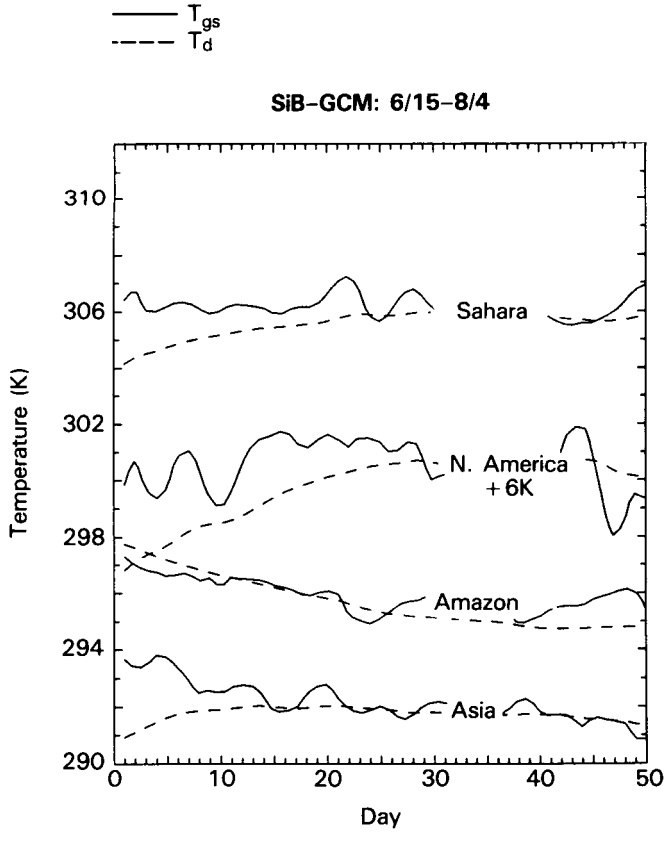

Figure 17a: The deep soil temperature, T_d, at 00 GMT and daily mean surface temperature, T_s, for a 50–day (June 14 – August 4) period summer simulation run by SiB–GCM. The daily mean surface temperature was derived from the daily mean upward longwave flux at the surface and so is a weighted mean of the canopy and ground temperature. The top pair of lines are for the Sahara Desert, the second pair for central and eastern U.S., the third pair are for the Amazon and the bottom pair are for Asia. 6 K was added to the temperatures for central and eastern U.S. for easier display.

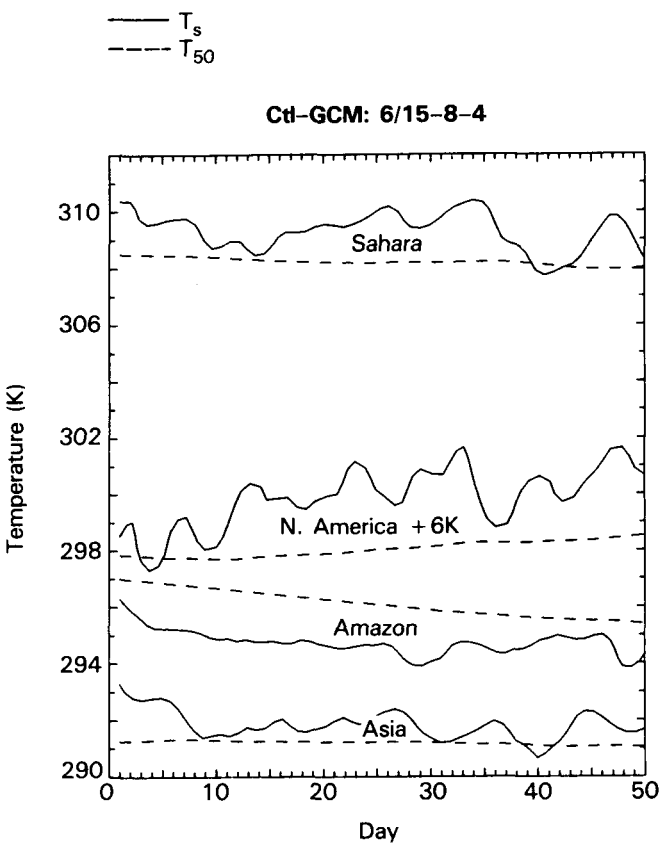

Figure 17b: The same as Fig. 17a, but for Ctl–GCM. The deep soil temperature, T_{50}, is at 50 cm depth.

4.3 Global Surface Field

4.3.1 Summer Case

The surface latent heat flux for the first 30 days in the summer simulation by SiB–GCM (Ctl–GCM) is shown in Fig. 18a (18b) and the difference in Fig. 18c. Except for the deserts, the latent heat flux in Ctl–GCM over the continents is usually more than 150 W/m^2 and sometimes exceeds 200 W/m^2 in parts of North America and South Asia. In SiB–GCM, latent heat fluxes of more than 150 W/m^2 are observed only in South Asia. The difference map shows that SiB–GCM gives 25–50 W/m^2 (1–2 mm/day) less evapo–transpiration over most vegetated land.

We compared the latent heat flux calculated with SiB–GCM with the global map of climatological latent heat flux for June as estimated by Budyko (1974). Budyko's estimates were found to be less than the simulated value over all land surfaces; for example, his estimated latent heat fluxes in the Amazon basin and central/eastern U.S. are 80 W/m^2 and 60 W/m^2, respectively, which are much less than the observed values of 90–120 W/m^2 and 90 W/m^2 for the respective regions cited in the previous subsection. The global map of surface net radiation (Budyko, 1974) shows values which were typically one half of the downward solar radiation over the land surface. The simulations from both GCM's suggest that this only happens over deserts where the surface albedo is high and the

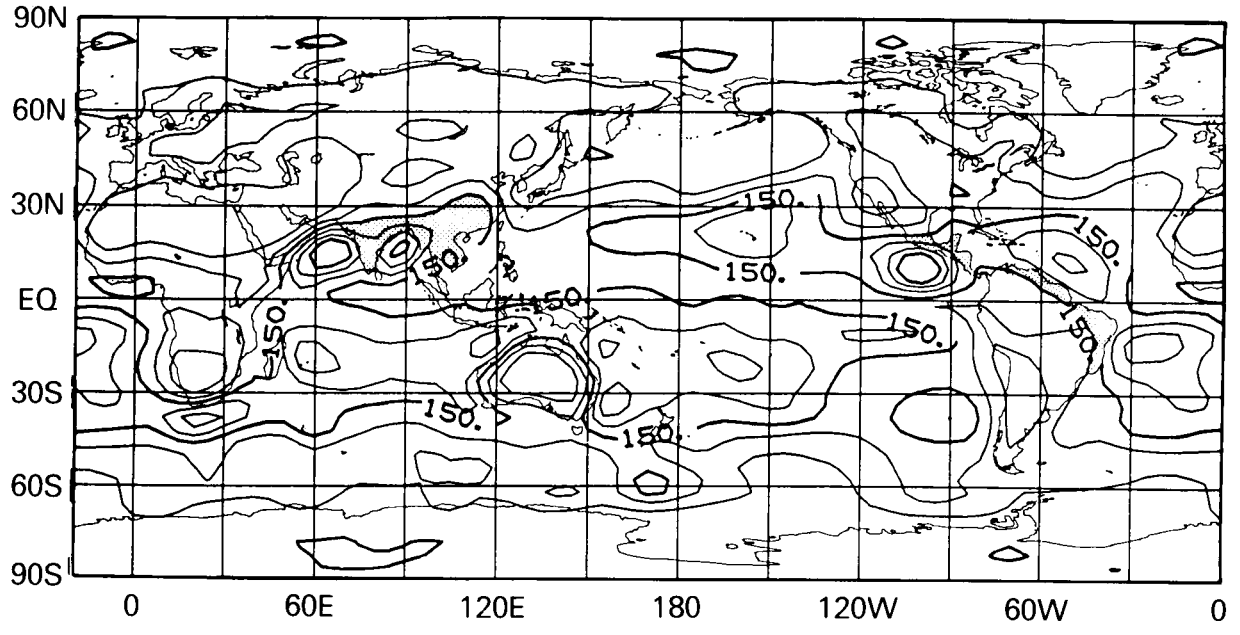

Figure 18a: Global field of mean surface latent heat flux in the SiB–GCM summer simulation for the first 30–day period (June 15 – July 14). The contour interval is 50 W/m^2. Land areas with mean latent heat fluxes in excess of 150 W/m^2 have been shaded.

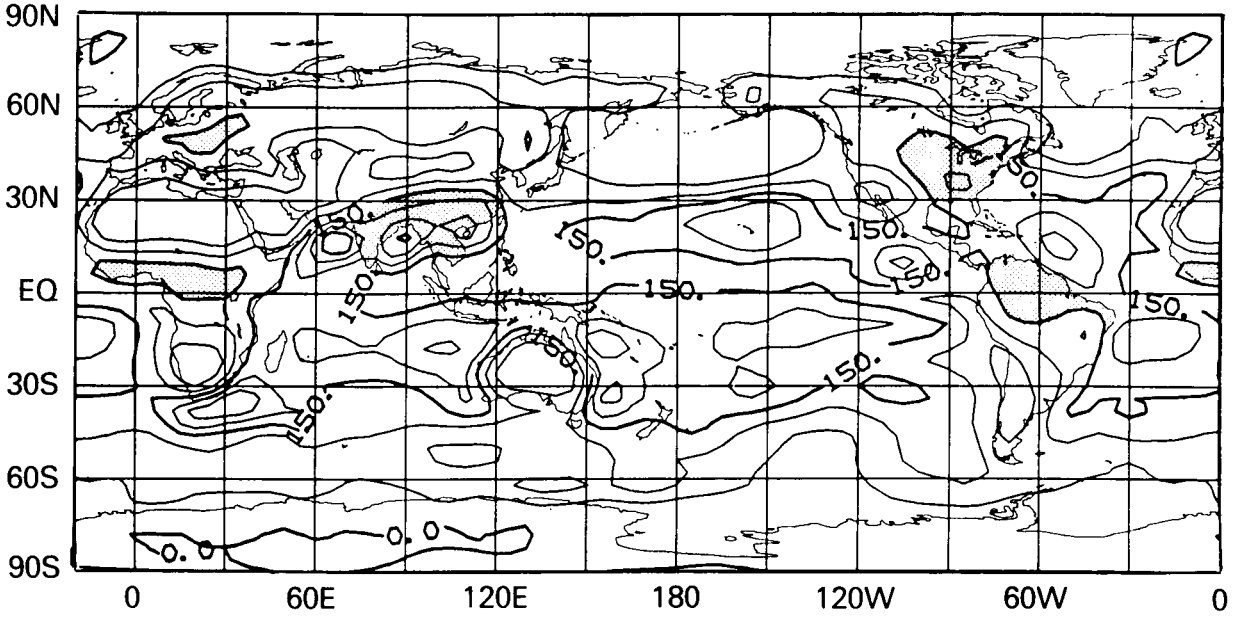

Figure 18b: The same as Fig. 18a except for Ctl–GCM.

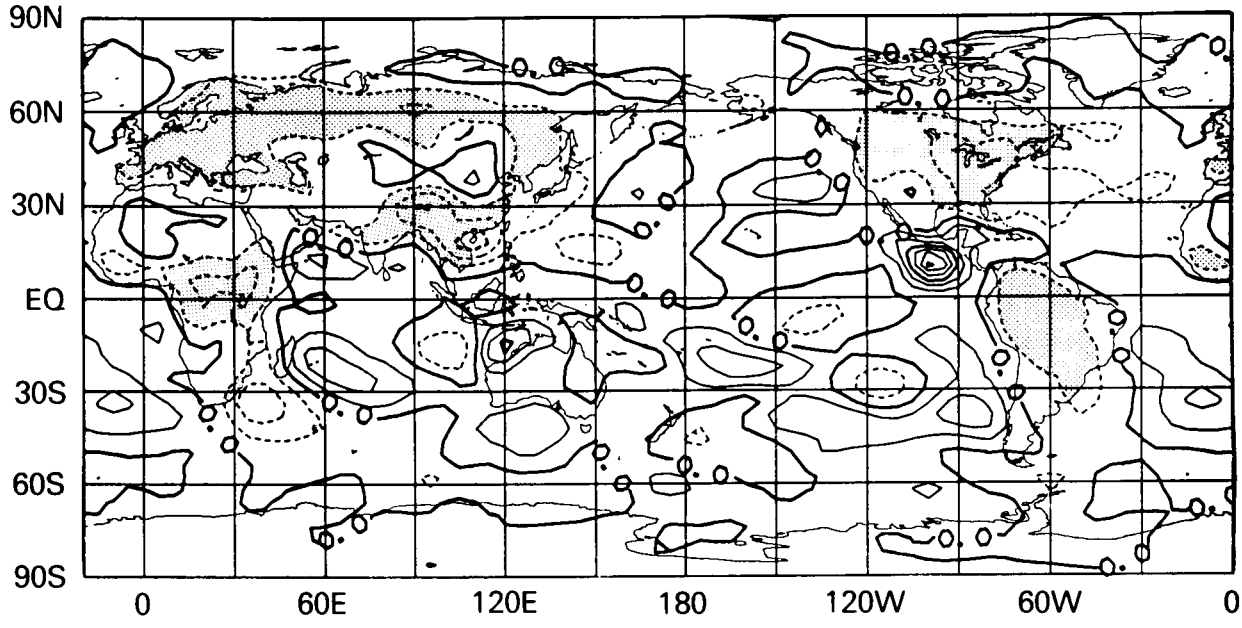

Figure 18c: The difference between the 30–day (June 15 – July 14) mean latent heat fluxes of the summer simulations: SiB–GCM minus Ctl–GCM The contour interval is 25 W/m^2. The land areas where Ctl–GCM produces > 25 W/m^2 of latent heat flux compared to SiB–GCM have been shaded.

atmospheric humidity is low. Table 1 shows that over the Sahara desert, about 58% of the incoming solar radiation is lost by reflection and longwave emission and the remaining 42% is available for sensible and latent heat fluxes. Over densely vegetated regions like the Amazon basin, only about 30% is lost (see Figs. 14a and 14b). Although the net loss of surface energy by terrestrial radiation is dependent on the amount and height of the prescribed cloud in both the climatological estimation (Budyko, 1974) and the GCMs, Budyko's value does seem to severely underestimate the net radiation and consequently the latent and sensible heat fluxes.

Figure 19a (19b) shows the mean daily precipitation rate simulated by SiB–GCM (Ctl–GCM) and Fig. 19c the difference between them. For comparison, a climatological field for the June–July period (Jaeger, 1976) is presented in Fig. 19d. Generally, the simulated precipitation pattern agrees well with the climatology, but the Ctl–GCM field is marked by excessive precipitation in North America and northern Eurasia. The difference map clearly illustrates the reduction of precipitation over vegetated land in SiB–GCM. There is a northward shift of the monsoon rainbelt in Asia in SiB–GCM relative to Ctl–GCM.

The surface sensible heat flux for the first 30 days in the summer simulation by SiB–GCM (Ctl–GCM) is shown in Figs. 20a and 20b with the difference shown in Fig. 20c. Except for the arid zones, the time–averaged sensible heat flux in Ctl–GCM is very small over land and even negative over the tropical forests while in SiB–GCM, the time–averaged sensible heat flux is more than 25 W/m^2 almost everywhere over the vegetated land. The negative value observed in the defference field in northern China is a result of the higher albedo and wetter soil in SiB–GCM, the wetter soil being due to the northward shift of the rainbelt in China in SiB–GCM.

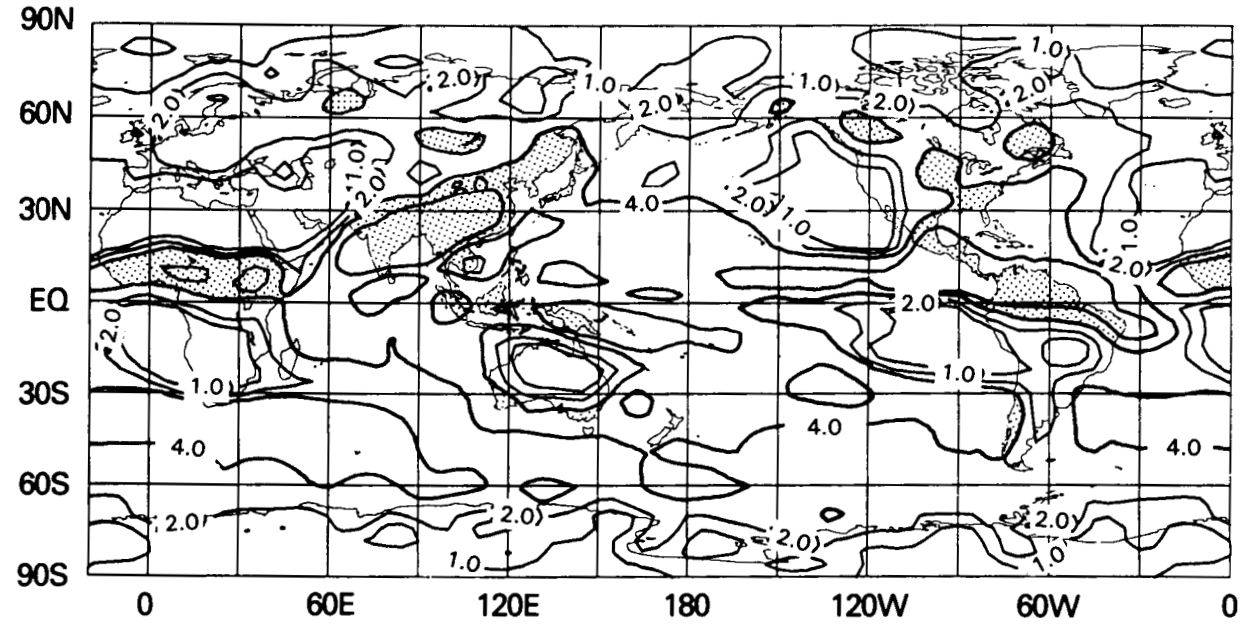

Figure 19a: Mean daily total (convective & large scale) precipitation in the SiB–GCM summer simulations for the first 30–day (June 15 – July 14) period. The contour intervals are 1.0, 2.0, 4.0 and 8.0 mm/day. Areas with rainfall rates greater than 4.0 mm/day have been shaded.

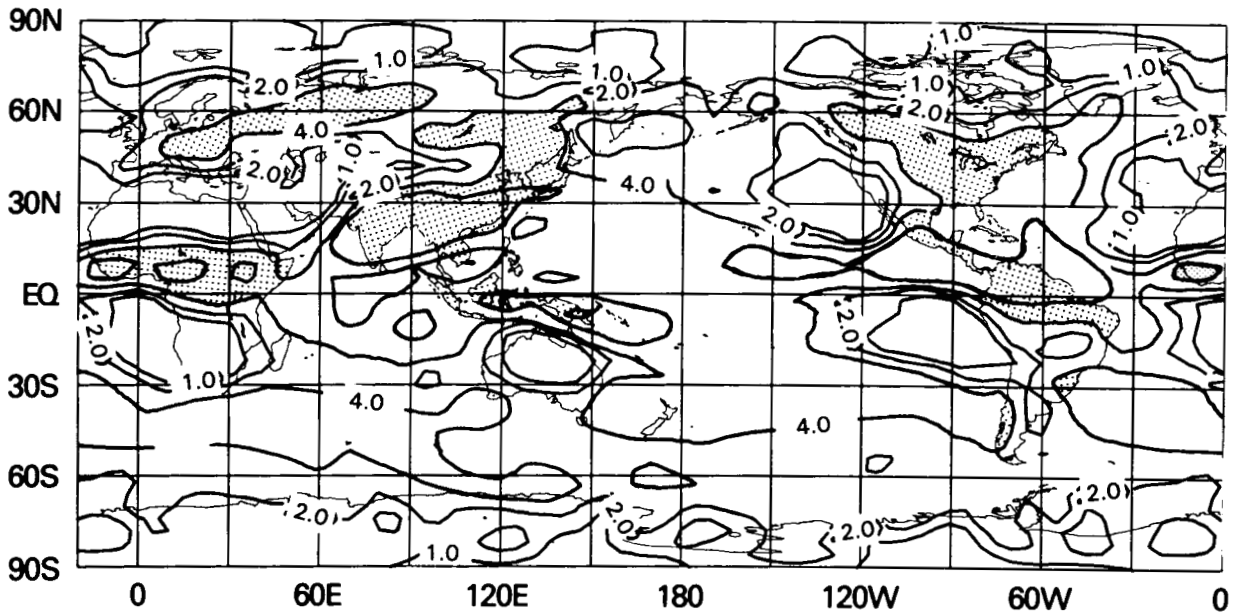

Figure 19b: The same as Fig. 19a except for Ctl–GCM.

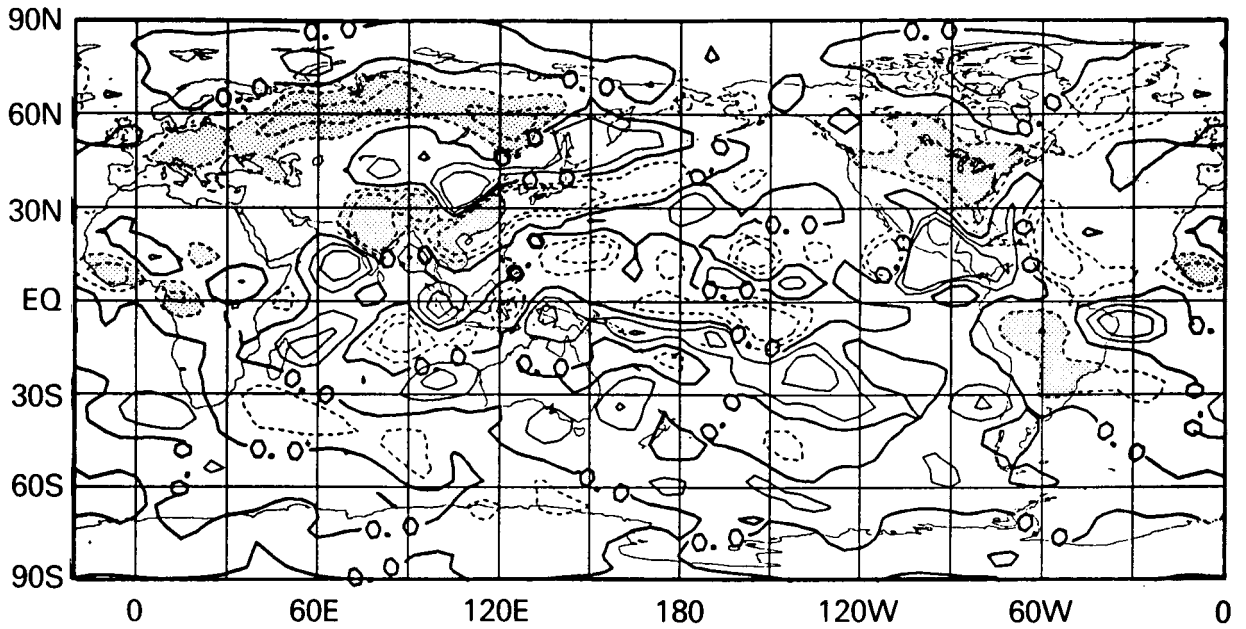

Figure 19c: The difference between the 30–day (June 15 – July 14) mean daily precipitation for the summer simulations: SiB–GCM minus Ctl–GCM. The contour interval is 1 mm/day. The land areas where Ctl–GCM produces > 1 mm/day of precipitation compared to SiB–GCM have been shaded.

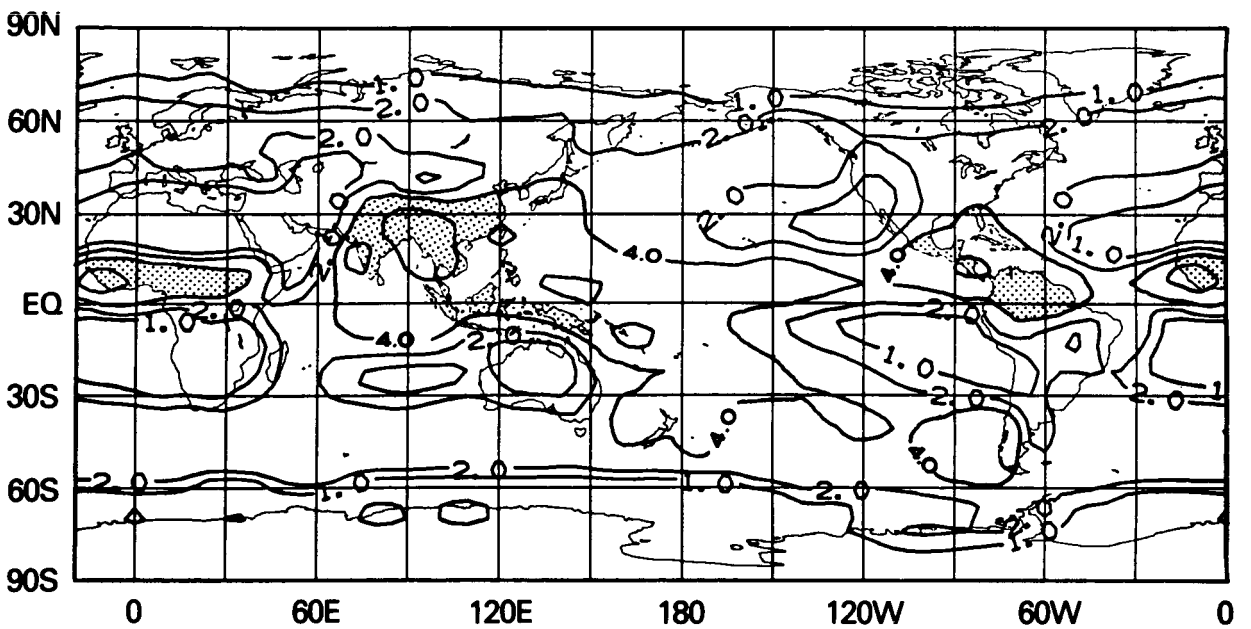

Figure 19d: Mean observed daily precipitation for June–July from Jaeger (1976).

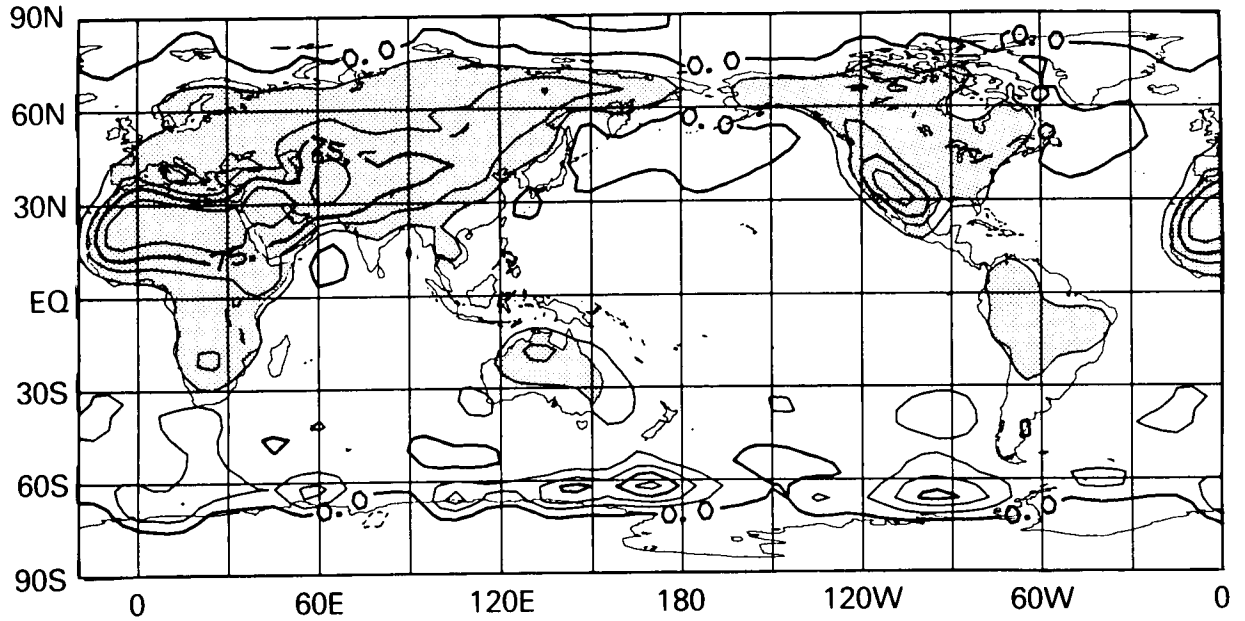

Figure 20a: Global field of the mean surface sensible heat flux in the SiB–GCM summer simulation for the first 30–day period (June 15 – July 14). The contour interval is 25 W/m^2. Land areas with mean sensible heat fluxes in excess of 25 W/m^2 have been shaded.

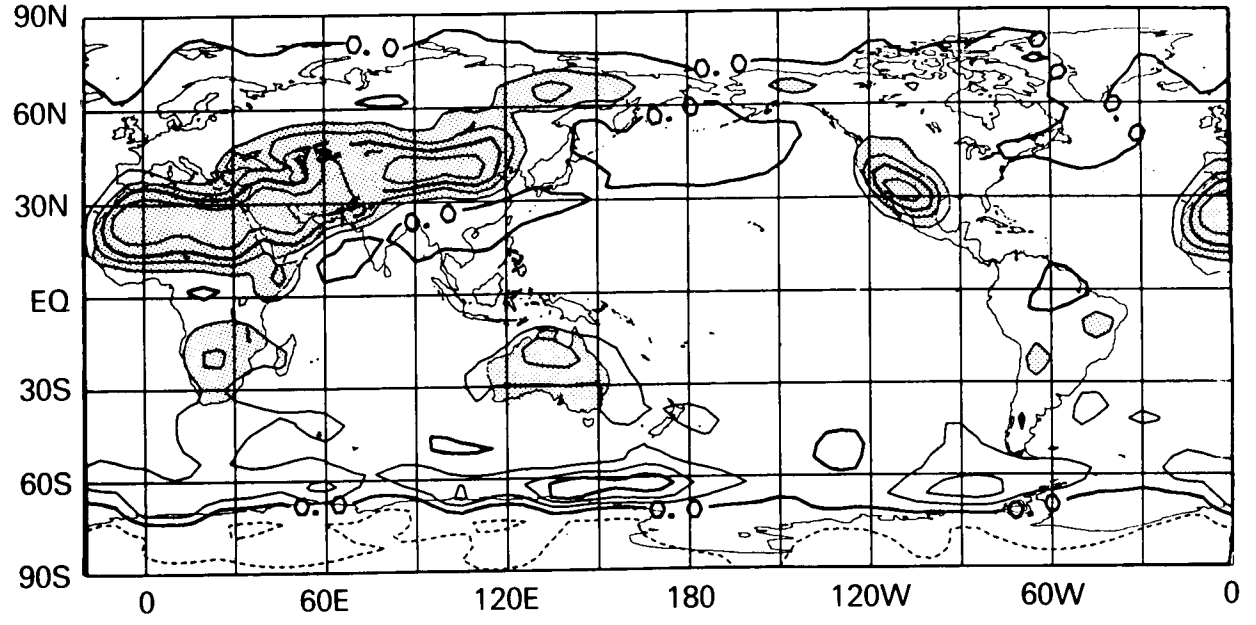

Figure 20b: The same as Fig. 20a except for Ctl–GCM.

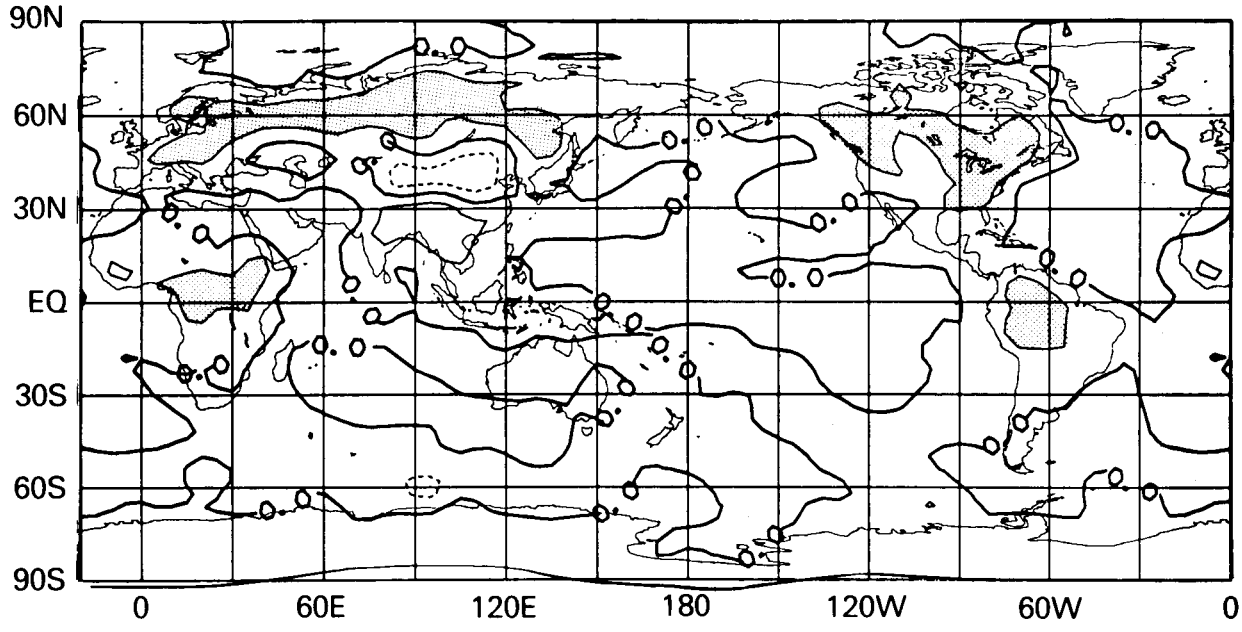

Figure 20c: The difference of the 30–day (June 15 – July 14) mean sensible heat fluxes for the summer (June 15 – July 14) simulations: SiB–GCM minus Ctl–GCM. The contour interval is 25 W/m^2. Land areas where SiB–GCM produces > 25 W/m^2 of sensible heat flux compared to Ctl–GCM have been shaded.

Figures 21a and 21b show the daytime PBL depth as simulated by SiB–GCM (Ctl–GCM). The PBL depth was derived by counting the number of layers where the 30–day mean heating rate generated by vertical diffusion exceeded 1 K/day. This definition was found to agree well with the conventional method of using potential temperature gradients.

Except for the deserts, the PBL depth in Ctl–GCM is calculated to be about 20 mb over the land which is unrealistically shallow; this is a direct result of the small sensible heat flux generated by Ctl–GCM. In SiB–GCM the PBL depth is more than 60 mb over most of the vegetated land and in the Amazon basin, the simulated depth of 100 mb agrees well with the observations of Martin et al. (1988). In both GCM's the PBL grew to 300 mb at some desert grid points. This very high value is consistent with the report of Blake et al. (1983) that the PBL depth in the Saudi Arabian desert could reach 350 mb.

In SiB–GCM, the daytime PBL in the SiB–GCM is more unstable than that of Ctl–GCM, and so momentum transport is more efficient in the former model. This results in a larger surface wind stress in SiB–GCM over land. Figures 22a and 22b show the zonally–averaged zonal surface wind stress in SiB–GCM (Ctl–GCM). The value over ocean is almost the same for both GCMs and agrees fairly well with that estimated from surface data by Hellerman and Rosenstein (1983). Over the continents, the SiB–GCM value is almost twice as large as the Ctl–GCM value.

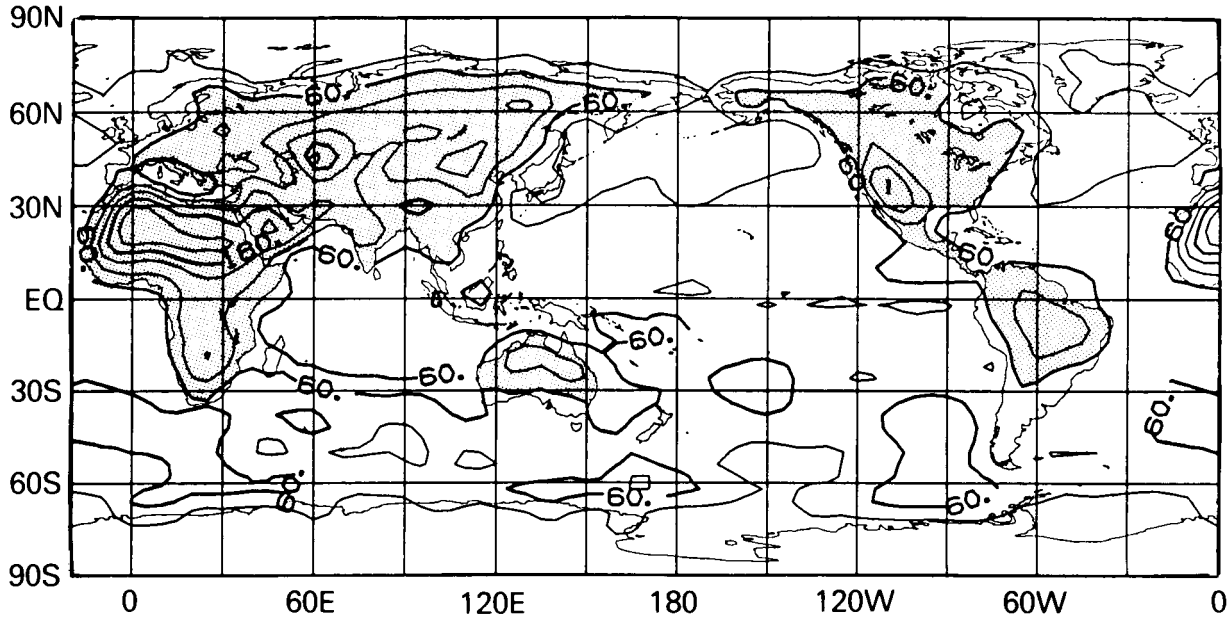

Figure 21a: Mean maximum PBL height in the SiB–GCM summer (June 15 — July 14) simulation The contour interval is 30 mb. Land areas where the mean maximum PBL height exceeds 60 mb have been shaded.

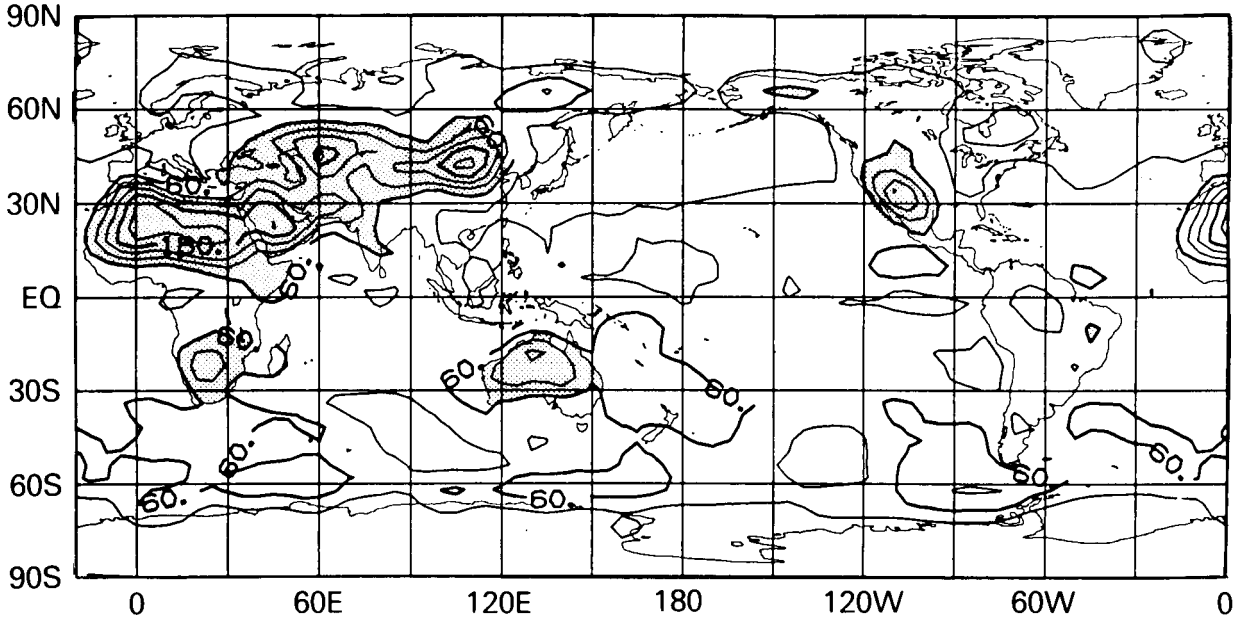

Figure 21b: The same as Fig. 21a except for Ctl–GCM.

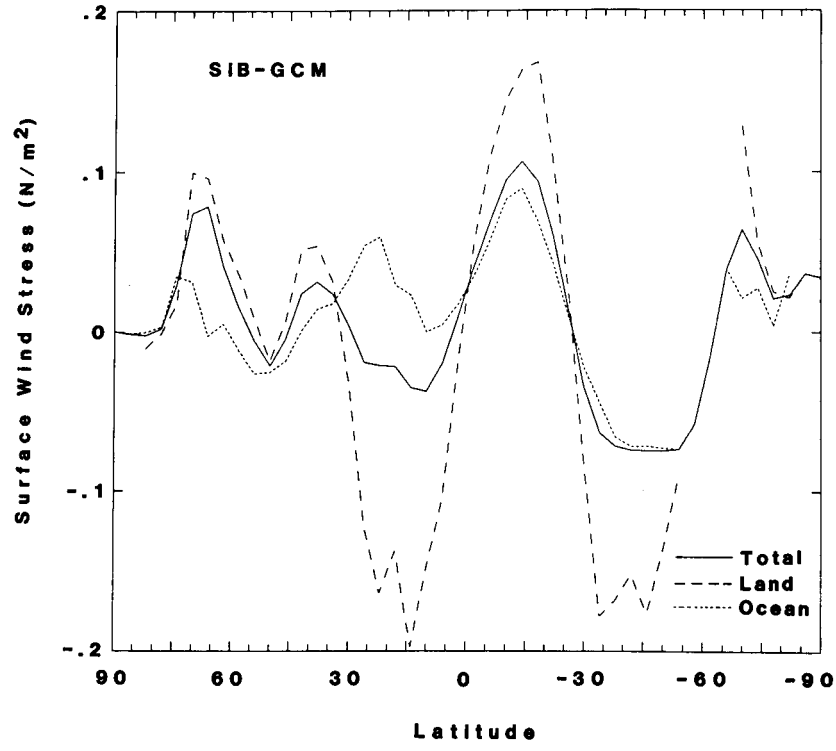

Figure 22a: Zonally averaged zonal wind stress in N/m^2 in the SiB–GCM summer (June 15 — July 14) simulation.

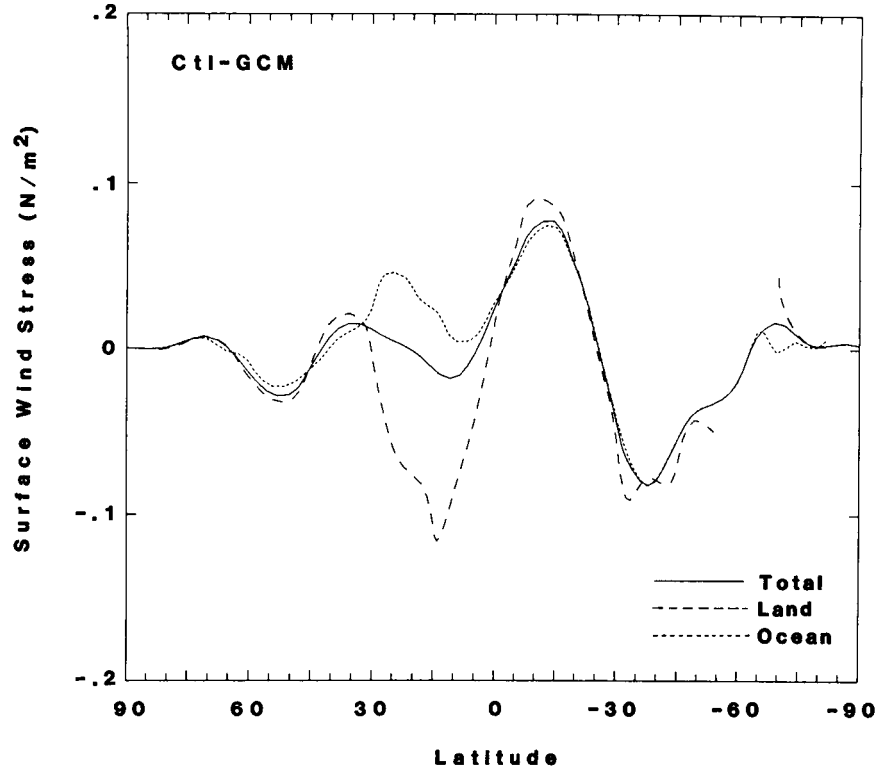

Figure 22b: The same as Fig. 22a except for Ctl–GCM.

4.3.2 Winter Case

In the winter simulation, the two 30–day runs were made with the surface drag parameterization of Deardorff (1972) which gave a slightly larger surface drag coefficient under stable and neutral conditions than the formulation based on the Monin–Obukhov model used in the summer simulations. This different formulation tended to reduce the Bowen ratio slightly, but the overall difference between the two GCMs was the same as in the summer simulation.

Figures 23, 24, and 25 show the differences between the latent heat flux, sensible heat flux and precipitation 30–day (December 15 – January 13) mean fields as calculated by SiB–GCM and Ctl–GCM for the 30–day winter simulation. The SiB–GCM enhances sensible heat flux by up to 50 W/m^2 with comparable decreases in the latent heat flux. The reduced sensible heat flux over Australia calculated by SiB–GCM is associated with its higher desert albedo values.

The simulated precipitation patterns from both GCM's are in good agreement with the climatology except in the Amazon basin. The climatological precipitation field exhibits one local maxima in the region; one in the northeast and another in the southeast of Brazil. The SiB–GCM is associated with decreased precipitation over land (through the reduction of evapotranspiration) but SiB did not change the basic precipitation pattern; it seems that other physics parameterizations in the GCM may be responsible for this problem.

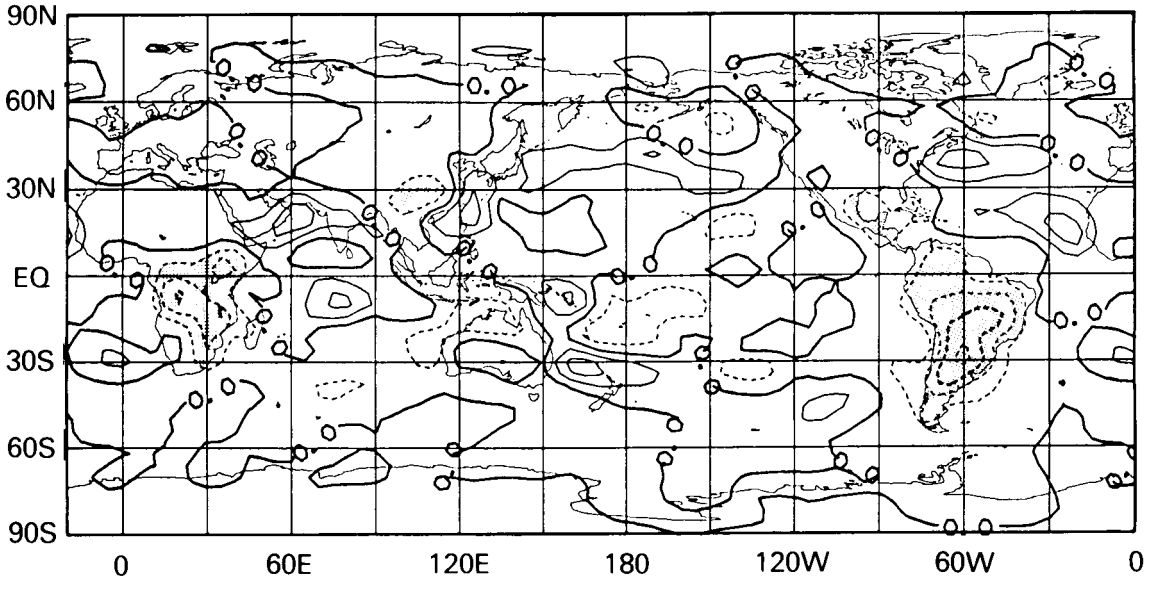

Figure 23: Difference field of latent heat flux as calculated by SiB–GCM and Ctl–GCM for the 30–day winter (December 15 – January 13) simulations: SiB–GCM minus Ctl–GCM. The contour interval is 25 W/m^2. Land areas where Ctl–GCM produces > 25 W/m^2 of latent heat flux compared to SiB–GCM have been shaded.

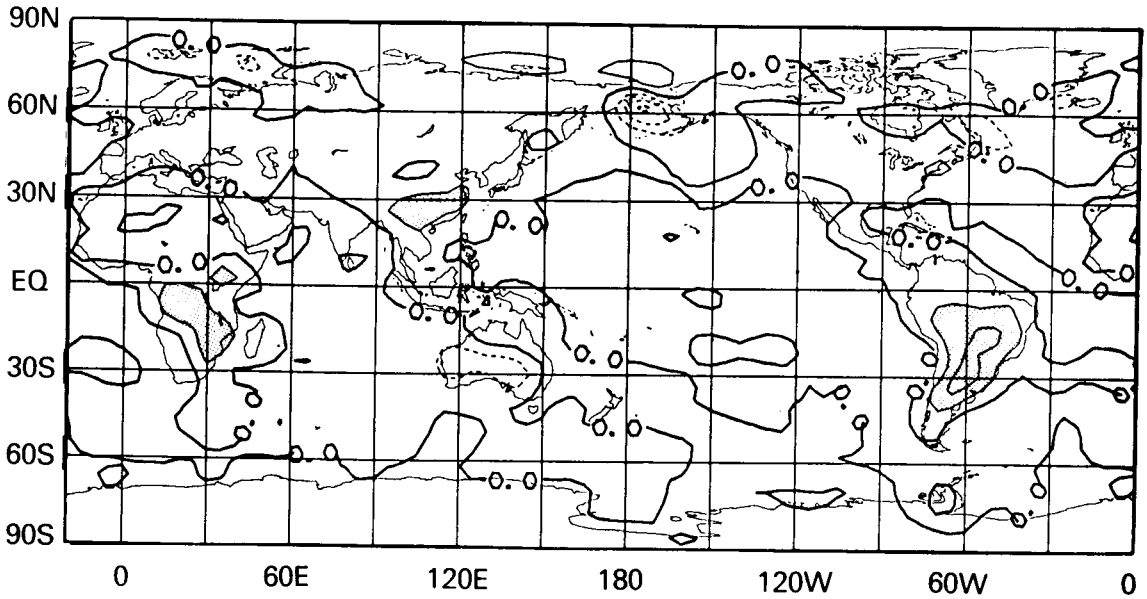

Figure 24: Difference field of sensible heat flux as calculated by SiB–GCM and Ctl–GCM for the 30–day winter (December 15 – January 13) simulations: SiB–GCM minus Ctl–GCM. The contour interval is 25 W/m^2. Land areas where SiB–GCM produces > 25 W/m^2 of sensible heat flux compared to Ctl–GCM have been shaded.

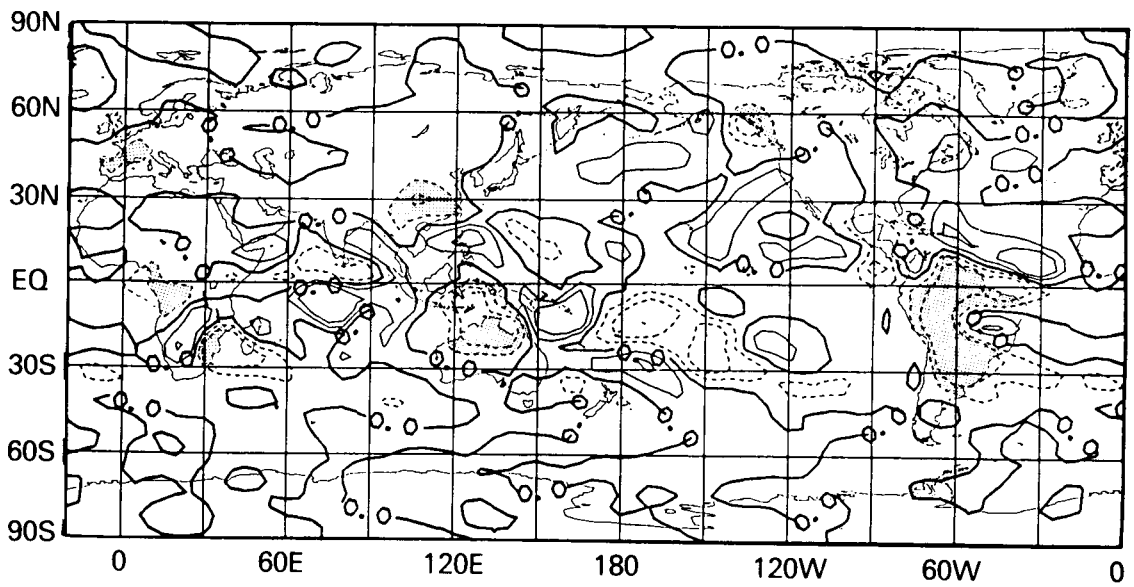

Figure 25: Difference field of mean daily precipitation rate (large–scale plus convective) as calculated by SiB–GCM and Ctl–GCM for the 30–day winter (December 15 – January 13) simulations: SiB–GCM minus Ctl–GCM. The contour interval is 1 mm/day. Land areas where Ctl–GCM produces more than 1 mm/day of precipitation than SiB–GCM have been shaded.

4.4 Impact on the Large Scale Atmosphere Circulation

The impact of SiB on the large scale atmospheric circulation is briefly discussed here. Clearly, the shortness of the simulation runs performed with SiB–GCM and Ctl–GCM and the uncertainties in the soil moisture initialization (see earlier sections and Appendix D) prevent us from drawing definitive conclusions. Longer runs, where the effects of the soil moisture initialization scheme can be disregarded, must be carried out to fully investigate the interactions between the surface energy balance and the large scale circulation.

4.4.1 Summer Case

Figures 26a and 26b show the 200 mb zonal winds for the first 30 days of the summer simulation by SiB–GCM (Ctl–GCM). The weakening of the tropospheric jet in SiB–GCM compared with Ctl–GCM is noticeable in the northern hemisphere. Wind speeds of more than 30 m/s are observed in the NMC analysis (Fig. 26c) and in the Ctl–GCM simulated field, but not in the SiB–GCM simulated field. Although not clearly visible in the maps, the jet stream has also shifted slightly northward in the SiB–GCM simulation.

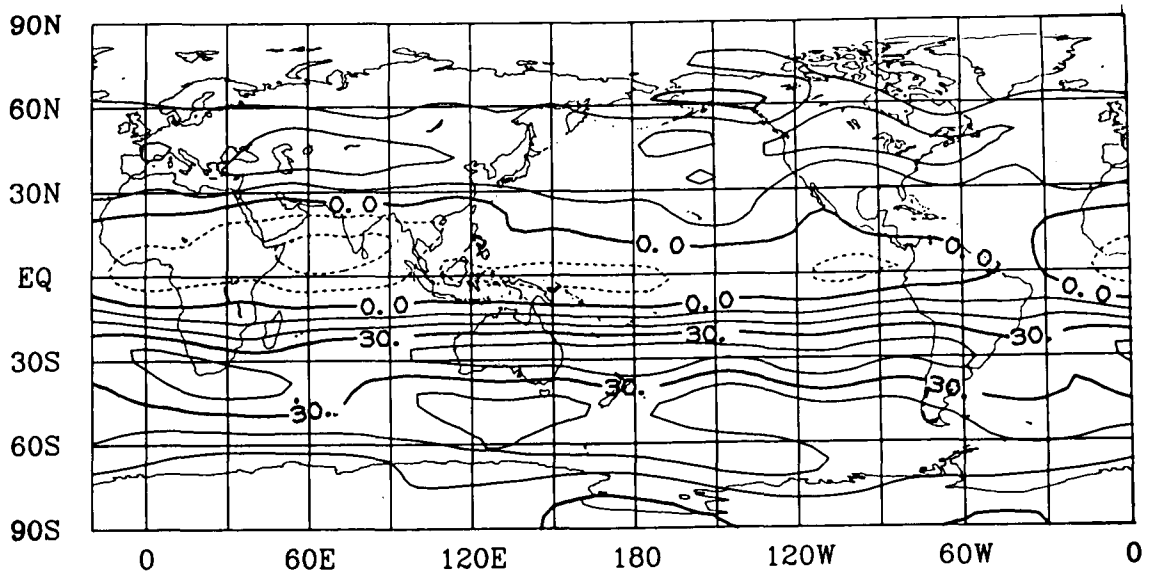

Figure 26a: Mean zonal wind at 200 mb in the SiB–GCM summer (June 15 — July 14) simulation for the first 30 days. The contour interval is 10 m/s.

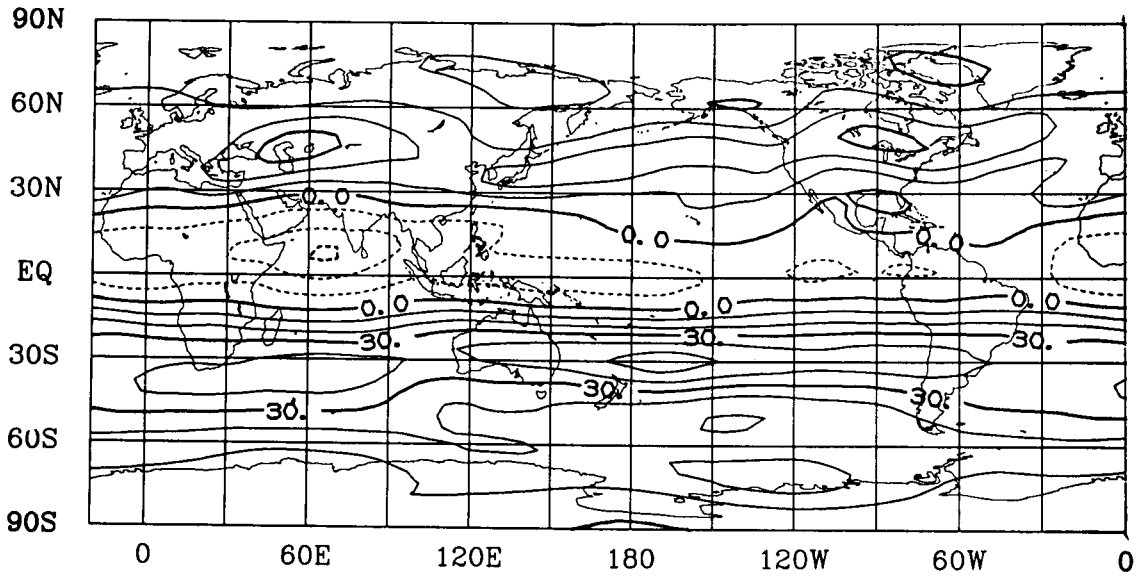

Figure 26b: The same as Fig. 26a except for Ctl–GCM.

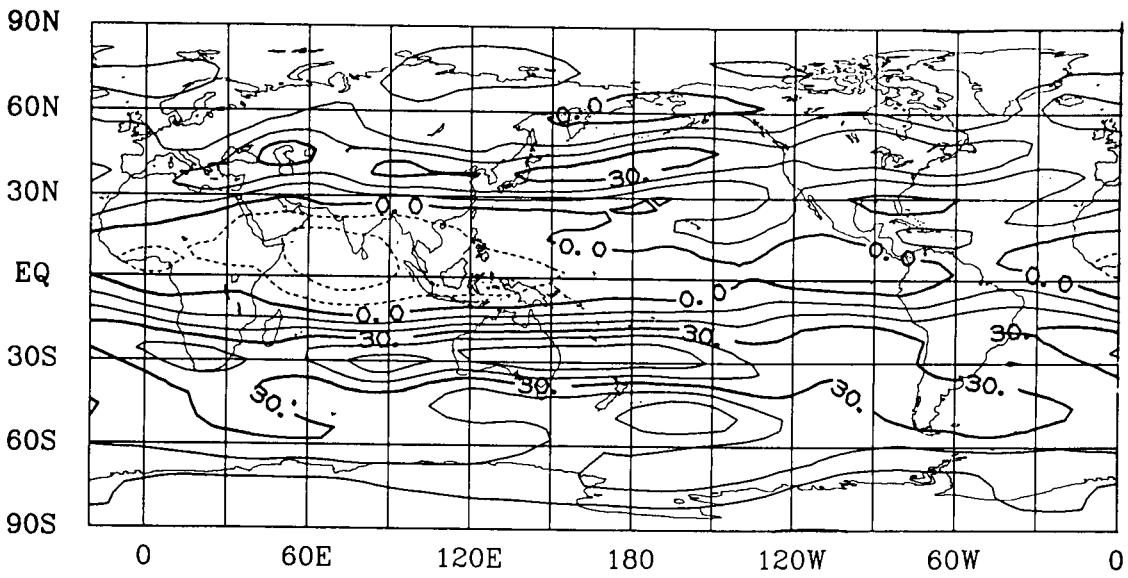

Figure 26c: Mean zonal wind at 200 mb from the NMC analysis for the period June 15 — July 14, 1986.

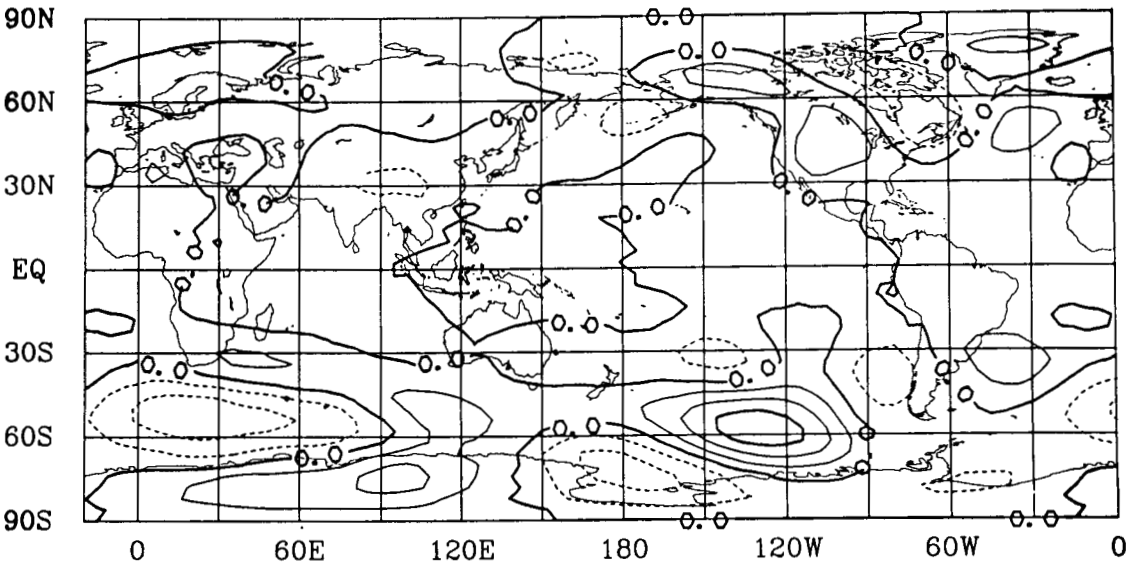

Figure 27a: Mean eddy geopotential height at 500 mb in the SiB–GCM for the summer (June 15 — July 14) simulation. The contour interval is 40 m.

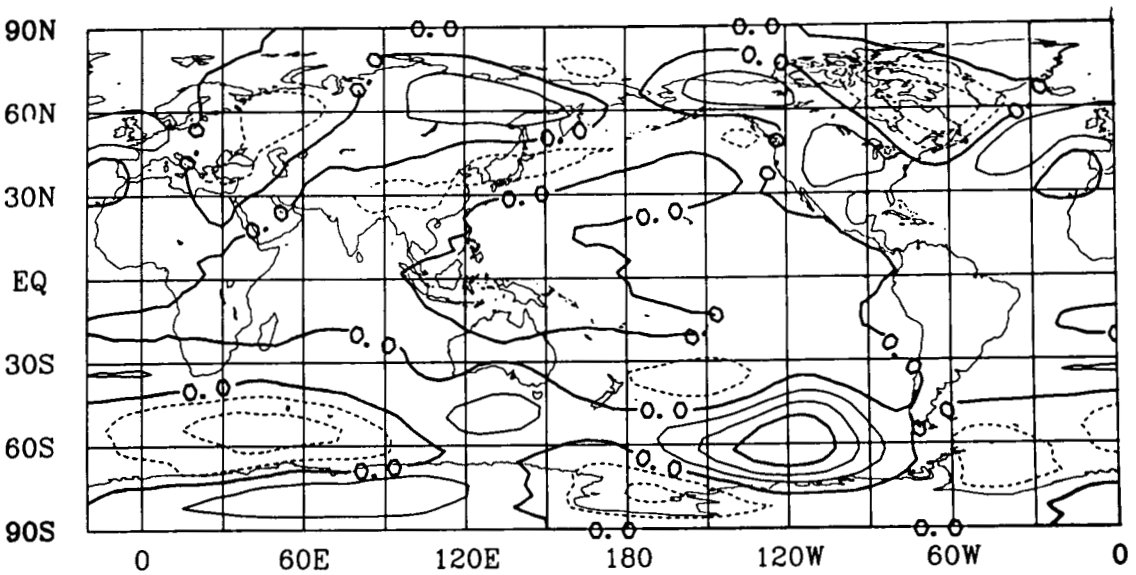

Figure 27b: The same as in Fig. 27a except for Ctl–GCM.

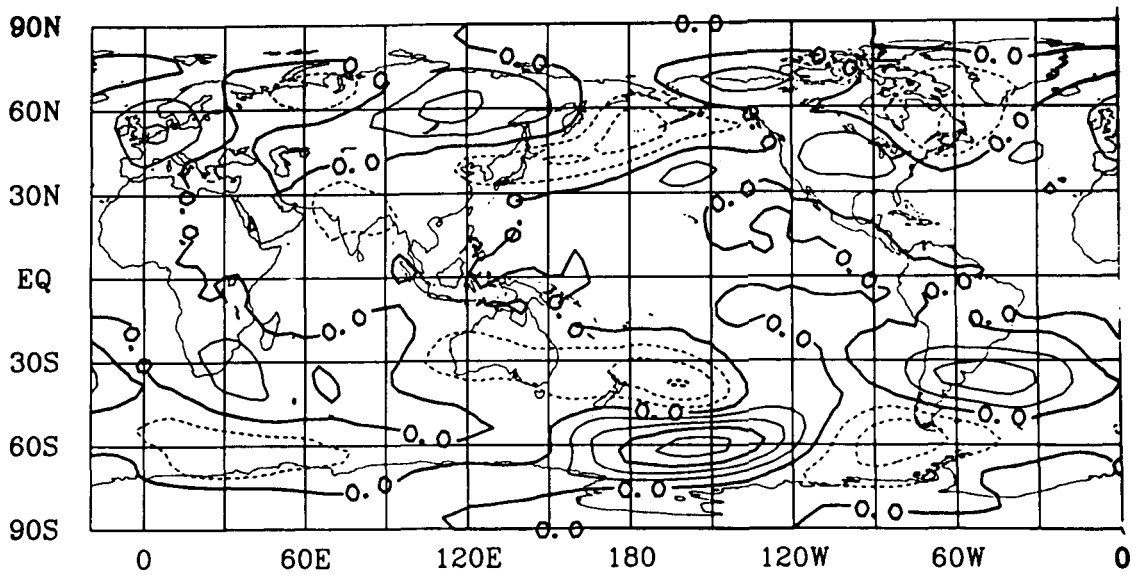

Figure 27c: Eddy geopotential height at 500 mb from NMC analyses averaged for the period June 15 — July 14, 1986. The contour interval is 40 m.

The 500 mb eddy geopotential height for the first 30 days of the summer simulation as simulated by SiB–GCM (Ctl–GCM) is shown in Fig. 27a (27b). When compared with the NMC analysis the simulations by both GCM's appear to be better in the northern rather than the southern hemisphere (Fig. 27c). The wavy pattern over the Eurasian continent in the SiB–GCM simulation is flatter than in the Ctl–GCM simulation while the trough to the north of the Caspian Sea is completely missed in the SiB–GCM simulation.

4.4.2 Winter Case

The simulation of the circulation in the northern hemisphere is very good in both GCM's when compared with the analyzed field. Ctl–GCM simulates the ridge around Lake Baikal better than SiB–GCM, but the ridge to the south of New Zealand seems to be better represented in SiB–GCM.

5. SUMMARY AND DISCUSSION

The Simple Biosphere Model (SiB) developed by Sellers et al. (1986) was implemented in a modified version of the NMC spectral model. The SiB–GCM was integrated for 50 days in a (boreal) summer simulation and for 30 days in a (boreal) winter simulation. The simulated surface and atmospheric fields were compared with those produced by the control GCM (Ctl–GCM) which has the same physics package as SiB–GCM except for the 'bucket' hydrological model and the three soil layers with predicted temperatures.

Ctl–GCM was found to give too much evaporation over the vegetated land; sometimes the latent heat flux was almost equivalent to the net radiation. On the other hand, SiB–GCM generated sensible and latent fluxes over the land which compared well

with observations. The improvement in the calculated Bowen ratio in SiB–GCM comes from the explicit treatment of transpiration control by stomatal resistance.

There is a secondary effect due to the generally higher land–surface albedos calculated by SiB–GCM as compared to the prescribed fields used in Ctl–GCM. This is thought to alter the total available energy by about 6% in vegetated areas with a similar impact on the evapotranspiration rate. The stomatal resistance effect, however, accounts for the rest of the reduction in evapotranspiration, typically 25% or greater over the moist vegetated regions. This result corresponds with those in the sensitivity study of Sellers and Dorman (1987).

The increase in the sensible heat flux (25–50 W/m^2) over the vegetated land calculated by SiB–GCM was associated with higher surface temperatures and larger and more realistic diurnal ranges in the surface and PBL temperatures. The daytime PBL depth was 60–100 mb over vegetated land in SiB–GCM compared with the unrealistic value of 20 mb calculated by Ctl–GCM. A deeper PBL and more active momentum exchange over the land led to an increase in the surface stress calculated by SiB–GCM.

The SiB–GCM June – July precipitation rate was 1 to 2 mm/day lower than in the Ctl–GCM run in the Amazon basin, the African tropics, North America, the Soviet Union and Europe. The monsoon rainbelt in China moved northward, but overall the precipitation there also decreased. This decrease in the precipitation rate corresponded roughly to the decrease in the time–averaged latent heat flux, i.e., about 25–50 W/m^2.

SiB–GCM still generated more rain than the climatological precipitation in some places over land. This may be due to inadequacies in the physical parameterizations in the GCM or it could be that SiB–GCM still calculates evapotranspiration rates that are too high because of problems in the soil moisture initialization. Over the central and eastern United States, the simulated horizontal moisture convergence in June–July was almost zero in both GCMs and was in good agreement with observations, but the evaporation rate and hence the precipitation rate in the region was far lower in SiB–GCM. This suggests that the excessive precipitation calculated over land by Ctl–GCM may be the result of an overestimation of the evaporation rate. An experiment was performed to explore this hypothesis by integrating SiB–GCM with decreased initial soil moisture in central and eastern U.S. (The soil moisture initialization was suspect as it is an uncertain part of any GCM model). The results showed that the simulated horizontal moisture convergence remained almost zero and the smaller evapotranspiration rate over land directly contributed to a reduction in the precipitation rate.

In the course of the 50–day simulation, soil wetness in SiB–GCM changed very slowly. This was partly due to the large soil moisture capacity in the SiB formulation and partly due to the small differences between evapotranspiration and precipitation.

In Ctl–GCM soil wetness was updated every day from values interpolated from monthly climatology. Over vegetated land in the Northern Hemisphere the soil moisture decreased rapidly over the June – August period. This brought about a gradual increase in the sensible heat flux and a decrease in the latent heat flux which led in turn to a reduced precipitation rate.

The realism of SiB–GCM and Ctl–GCM on smaller spatial scales was also scrutinized. The diurnal variation and the mean value of the albedo as calculated with SiB–GCM were found to be satisfactory when compared with observations while the albedos used in Ctl–GCM were generally too low. The interception loss fraction is difficult to verify, but at least in the Amazon basin the SiB–GCM value of 28% of the total latent

heat flux seems to be reasonable. Overall, SiB–GCM appears to give a more consistent and realistic simulation of hydrological processes and near–surface atmospheric conditions than Ctl–GCM.

It should also be noted that the differences between the values of sensible heat flux, evapotranspiration and precipitation calculated by the two models are maximized in the humid vegetated regions of the summer (growing season) hemisphere. Under the prevailing conditions of low relative humidity and high radiation loads the evaporation rate is very sensitive to the value of the stomatal resistance, which is around 100 s/m in SiB–GCM and effectively zero in Ctl–GCM.

A preliminary assessment of the impact of SiB–GCM on the large scale atmospheric circulation was also made. The large–scale circulation changed only slightly in the northern hemisphere winter simulation. This is understandable because of the small land area in the southern hemisphere and because the continents in the northern hemisphere receive little solar radiation in winter.

In the summer simulation there was some noticeable impact: the 200 mb jet stream and the wind speed at 850 mb were found to be unfavorably weakened in SiB–GCM which also failed to simulate the stationary trough in the 500 mb geopotential height. We do not yet understand the causality of this effect. Clearly, the above comments must be regarded as very preliminary in view of the shortness of the simulation runs (50 days or less) and the uncertainties in the soil moisture initialization.

In summary, the implementation of SiB in the GCM has improved the simulated partition of absorbed energy at the land surface. Generally, the explicit recognition of stomatal resistance terms in the SiB latent heat flux formulation has resulted in a reduction in the land surface evapotranspiration rate compared to the bucket model calculation. In the summer simulations, this led to approximately matching reductions in the continental precipitation rates in SiB–GCM. The reduction in evapotranspiration and rainfall rates over the land due to SiB seems to be supported by the available observations.

APPENDIX A

ANALYTIC FUNCTION FOR C_m AND C_h BASED ON MONIN–OBUKHOV SIMILARITY THEORY.

$$C_m = \frac{1}{F_m^2}, C_h = \frac{1}{F_m F_h} \tag{A.1}$$

where C_m, C_h are multiplied by the magnitude of the wind velocity to yield the drag coefficients for momentum transfer and heat/moisture transfer.

$$F_m^o = F_h^o = [\ln(z_r/z_o)/0.40] * 0.87581 - 1.5630 \tag{A.2}$$

stable region : Ri>0

$$F_m/F_m^o = F_h/F_h^o = \exp[-1.8900 + (1.8900)^2 + 5.0519x] \tag{A.3}$$

$$x = \ln(1.0 + 10.815\ Ri)$$

unstable region : Ri>0

$$F_m/F_m^o = \exp[\ 1.2270 - (1.2270)^2 + 1.2642x] \tag{A.4}$$

$$x = \ln(1.0 - 1.2743\ Ri)$$

$$F_h/F_h^o = \exp[1.3462 - (1.3462)^2 + 1.8380x] \tag{A.5}$$

$$x = \ln(1.0 - 3.4805\ Ri)$$

where F_m^o and F_h^o are the neutral values of F_m and F_h, z_r is the reference height, z_o is the roughness length and Ri is the Richardson number.

The curves derived using the original Monin–Obukhov formulation and those using the analytic function above are presented in Fig. A.1. In all cases the reference height z_r was set to 20 m or to half the height of the lowest model level.

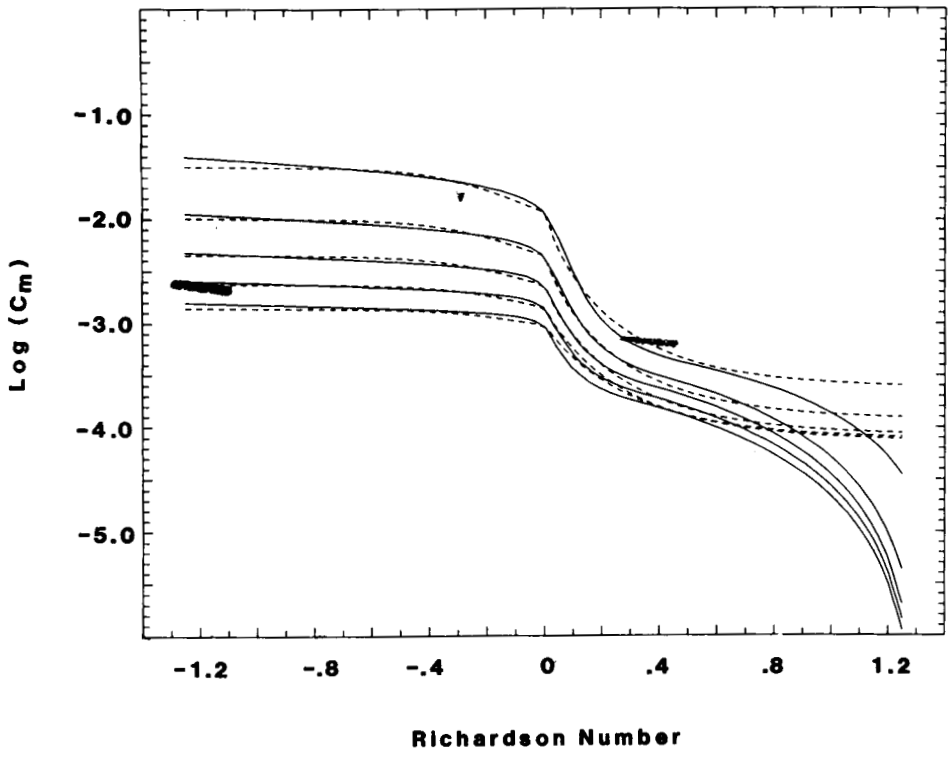

Figure A.1a: Surface drag coefficient for momentum transfer. The solid lines were derived from Monin–Obukhov Similarity theory and the dashed lines from the analytic function described in Appendix A. The range of the Richardson number is from −1.25 to 1.25. The roughness length, z_0, ranges from 100 cm (for the top line), 10 cm, 1 cm, 0.1 cm to 0.01 cm (for the bottom line).

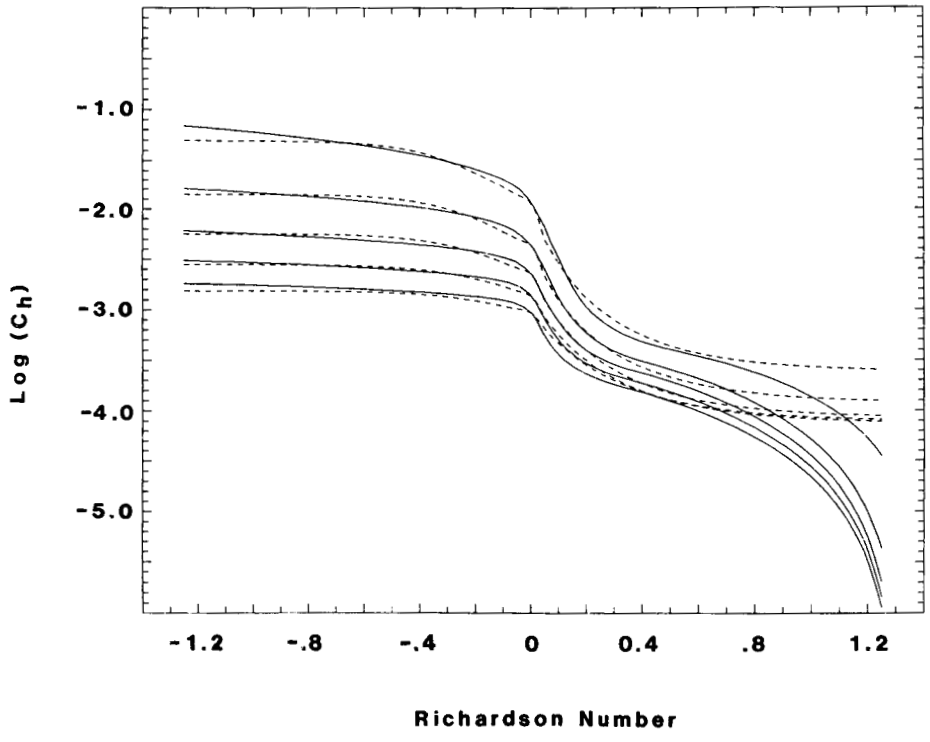

Figure A.1b: The same as Fig. A.1a except that the heat/moisture transfer coefficient is shown.

APPENDIX B

DERIVATION OF EFFECTIVE PBL MASS AND FORCING

The vertical diffusion tendencies for potential temperature, Θ , and specific humidity, q , are given by

$$\frac{\partial \Theta}{\partial t} = \frac{1}{\rho}\frac{\partial}{\partial z}\left[\rho K_h \frac{\partial \Theta}{\partial z}\right] \qquad \text{(B.1)}$$

$$\frac{\partial q}{\partial t} = \frac{1}{\rho}\frac{\partial}{\partial z}\left[\rho K_h \frac{\partial q}{\partial z}\right] \qquad \text{(B.2)}$$

where K_h is the vertical diffusion coefficient for heat and moisture transfer. The two equations are discretized in the vertical direction using σ –coordinates.

$$\frac{\partial \Theta_k}{\partial t} = A_k(\Theta_{k-1}-\Theta_k) - B_k(\Theta_k-\Theta_{k+1}) \quad ; \quad k = 1, 2, ..., 18 \qquad \text{(B.3)}$$

$$\frac{\partial q_k}{\partial t} = A_k(q_{k-1}-q_k) - B_k(q_k-q_{k+1}) \quad ; \quad k = 1, 2, ..., 12 \qquad \text{(B.4)}$$

where A_k and B_k are coefficients which arise from the vertical discretization scheme. If an implicit scheme with explicit coefficients is used

$$-A_k^*\dot{\Theta}_{k-1} + (1 + A_k^* + B_k^*)\dot{\Theta}_k - B_k^*\dot{\Theta}_{k+1} =$$

$$A_k\left[\Theta_{k-1}^{t-\Delta t} - \Theta_k^{t-\Delta t}\right] - B_k\left[\Theta_k^{t-\Delta t} - \Theta_{k+1}^{t-\Delta t}\right] \qquad \text{(B.5)}$$

$$\dot{\Theta}_k \equiv \frac{\Theta_k^{t+\Delta t} - \Theta_k^{t-\Delta t}}{2\Delta t}$$

$$A^* \equiv 2\Delta t A \ , \ B^* \equiv 2\Delta t B,$$

Then the system is solved by elimination.

APPENDIX C

TREATMENT OF SPATIALLY NON–UNIFORM PRECIPITATION IN SiB.

A simple scheme is used in SiB to account for the hydrological effects resulting from the spatial non–uniformity of convective precipitation. In nature, the net effect of the 'clumped' precipitation patterns typical of convective storms is to increase the area–averaged canopy throughfall and surface (infiltration excess) runoff rates relative to the equivalent rates produced by a spatially uniform rainfall fields. In most GCM's, a single (area–averaged) figure for convective precipitation is produced for each grid–area for each time step. In SiB, we assume that this rainfall amount is spatially distributed as shown in Fig. C.1 and given by Eq. C.1.

$$I_c(x) = a_c e^{-b_c x} + c_c \qquad (C.1)$$

$I_c(x)$ = relative amount of convective precipitation as a function of fractional area of grid area x, $(0<x<1)$, falling within a time step

a_c, b_c, c_c = constants

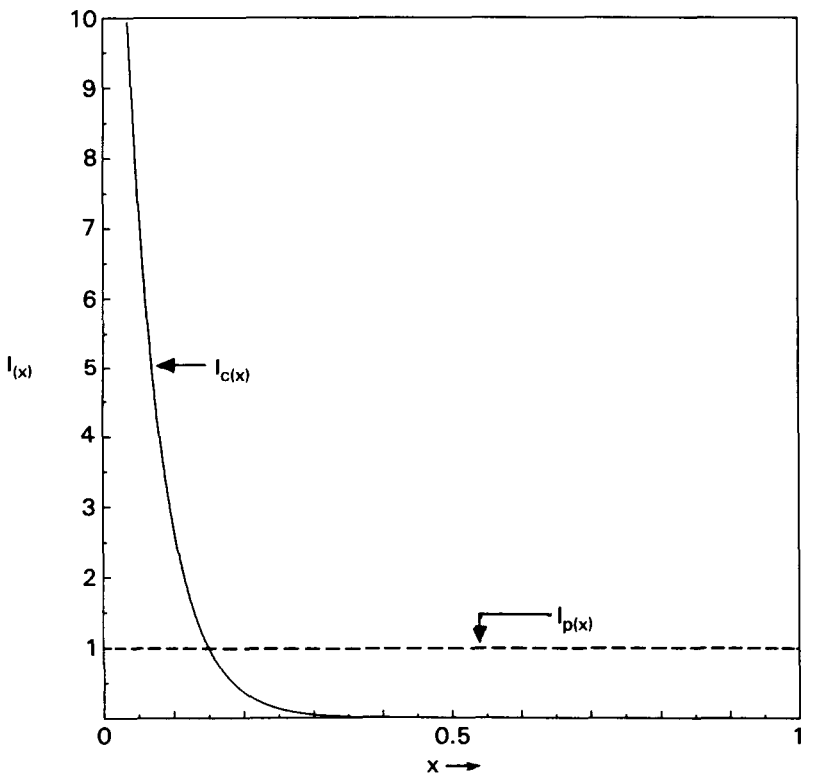

Figure C.1: Precipitation area–amount relationships used in SiB. The variable x refers to fraction of the grid area, the variable $I_{(x)}$ refers to the relative amount of precipitation. Note that the large scale precipitation, $I_{p(x)}$, is almost invariant over the grid area while convective precipitation, $I_{c(x)}$, is non–uniformly distributed.

The constants a, b, c were obtained by comparison with the data of Ruprecht and Gray (1976) and are normalized such that

$$\int_0^1 I_c(x)\, dx = 1 \qquad (C.2)$$

The values chosen for convective precipitation were $a_c = 20$, $b_c = 20$, $c_c = 0.206E{-}8$. For precipitation generated by large scale systems, the equivalent values are $a_p = 0.0001$, $b_p = 20$ and $c_p = 0.9999$ which means that in the interval $0 < x < 1$, $I_p(x) = 1$. Both types of precipitation (most models can produce both types simultaneously) can then be combined to give a single area–amount function by:

$$PI_{(x)} - (P_c\, a_c + P_p\, a_p)\, e^{-bx} + (P_c\, c_c + P_p\, c_p) \qquad (C.3)$$

P = total precipitation during a time step, mm $= P_c + P_p$

P_c, P_p = convective, large scale (uniform) precipitation rates during a time–step, respectively, mm

The term $PI_{(x)}$ can now be interpreted as an amount distribution which may be used to calculate throughfall rates and infiltration excess.

Firstly, the direct throughfall term in SiB is defined as that fraction of the rainfall that falls through holes and gaps in the vegetation canopy. (Such holes and gaps are assumed to be uniformly spread over the grid area.) The definition of this direct fraction is given in Sellers et al. (1986), Sec. 7(b); here it is referred to as G; $0 < G < 1$.

Then,

$$D_d = GP \qquad (C.4)$$

D_d = direct throughfall, mm

The amount of rainfall actually intercepted (though not necessarily retained) by the canopy is then given by

$$Y_{(x)} = (1{-}G)\, PI_{(x)} \qquad (C.5)$$

The proportion of the grid area for which the canopy has intercepted enough rainfall to equal or exceed its saturation limit, x_s, is then given by the solution to

$$Y_{(x_s)} = S_c - M_c \qquad (C.6)$$

S_c = canopy storage limit, mm

M_c = intercepted water stored on canopy at the beginning of the time step, mm

Combining (C.6) with (C.3) we have

$$x_s = -\frac{1}{b}\log\left[\frac{S_c - M_c}{a(1-G)P} - \frac{c}{a}\right] \qquad (C.7)$$

where $a \simeq (P_c a_c + P_p a_p)/P$ and so forth. Reference to Fig. (C.2) will show the physical significance of x_s and how it is used to calculate the canopy drainage term, D_c

$$D_c = \int_0^{x_s} Y(x)\,dx - (S_c - M_c)\,x_s$$

$$= P(1-G)\frac{a}{b}(1-e^{-bx_s}) + cx_s - (S_c - M_c)\,x_s \qquad (C.8)$$

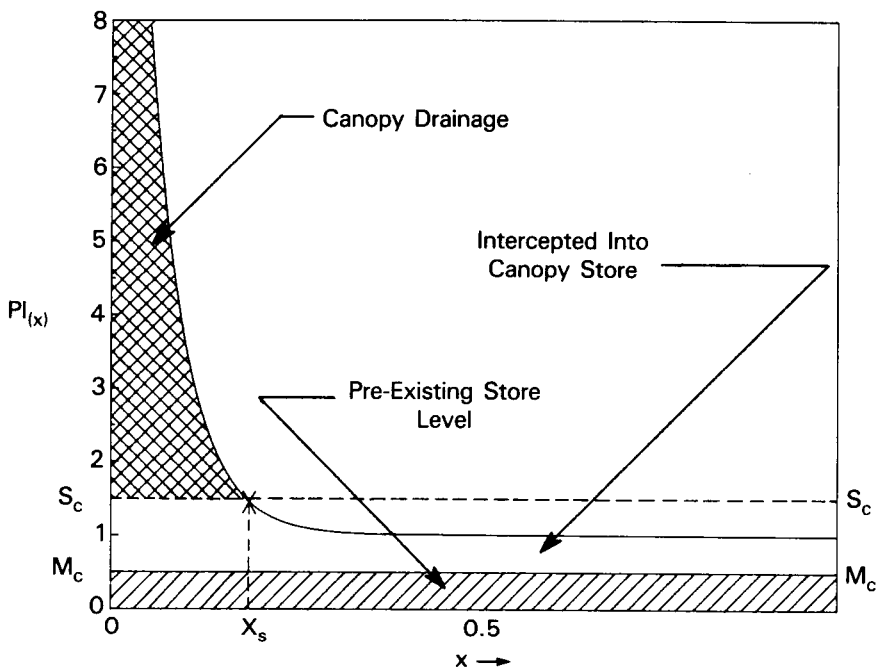

Figure C.2: Dynamics of precipitation interception by a vegetation canopy in SiB. The amount of water already stored in the canopy prior to rainfall interception, M_c, is considered to be uniformly distributed over the grid area (see hatched area). The integral of the water amount above M_c represents to total amount of water intercepted by the canopy. x_s is the proportion of the grid area where the intercepted rainfall plus the preexisting canopy water storage, M_c, exceeds the canopy storage limit S_c. All water above the S_c limit drains off the canopy, all below it is added to the canopy interception store.

Total throughfall to the ground, D, is then given by

$$D = D_d + D_c \qquad (C.9)$$

The amount of water remaining on the canopy, i.e., available for direct evaporation is given by:

$$M_{c_{t+1}} = M_{c_t} + P - D \qquad (C.10)$$

For the next time step, this water is assumed to be uniformly spread over the vegetation canopy in the grid area which is clearly inconsistent with the representation shown above and the illustration shown in Fig. (C.2). However, one can assume that the resulting errors are small as the non–uniformity of intercepted precipitation will only determine the *timing* of evaporation loss unless convective storms are immensely concentrated in time and space.

A similar calculation to that shown in (C.1) through (C.10) is performed for the ground cover so that an effective precipitation rate reaches the soil surface. With very heavy rainfall, the local infiltration capacity of the soil can be 'beaten' by the rainfall rate and (infiltration excess) overland flow can be generated. For the sake of simplicity, we assume the same area–amount relationship for the rainfall (in fact this would have been distorted by interception in the canopy, etc.). A soil hydraulic conductivity for the surface layer is calculated from Eq. 50 of Sellers et al. (1986) and this is used to calculate an equivalent depth of water that the soil can absorb during the time step.

$$P_i = K\Delta t \qquad (C.11)$$

P_i = amount of water that soil can absorb during the time step, mm
K = soil hydraulic conductivity, mm s^{-1}
Δt = time step duration, s

The fraction of the grid area giving rise to infiltration excess is calculated by

$$D_s I_{(x_i)} = P_i \qquad (C.12)$$

D_s = amount of throughfall and vegetation drainage reaching the soil surface, mm

The amount of infiltration excess is then simply given by

$$R_i = \int_0^{x_i} D_s I_{(x)}\, dx - P_i \qquad (C.13)$$

where the term inside the integral is similar to that in (C.8).

When snow falls, Eqs. C.1 to C.10 are used, but not C.11 to C. 13; that is, the snow can build up and fall off the vegetation, but accumulates on (and does not run off) the ground.

This scheme is in place in all current SiB implementations in GCMs.

APPENDIX D

INITIALIZATION OF GLOBAL SOIL MOISTURE FIELDS FOR THE SIMPLE BIOSPHERE MODEL (SiB)

It was recognized in Sellers et al. (1986) that SiB would be sensitive to the soil moisture initialization as this can have a marked effect on the calculated evapotranspiration rate and hence on all the components of the surface energy balance. Unfortunately, the soil moisture climatologies currently used by GCMs are not directly compatible with SiB as the formulations used to derive them are drastically different from the biophysically–based calculations used in SiB. This appendix reviews a methodology that can be used to transform the existing soil moisture fields into SiB–compatible soil moisture fields; the method requires no other data than the existing soil moisture climatology and the distributed SiB parameter set. For a number of reasons the methodology has severe limitations.

1. EXISTING SOIL MOISTURE CLIMATOLOGIES FOR GCM'S

The fields of soil moisture content used for the initialization of GCMs originate from two principal sources.

(i) Mintz and Serafini (in prep.). Mintz and Serafini used a simple water budget equation set to calculate time varying global soil moisture fields on a 4° by 5° grid.

The equations used were:

$$\frac{dS}{dt} = P - E \quad , S \leq S_{max} \tag{D.1}$$

$$E = \beta_{MS} E_p \tag{D.2}$$

$$\beta_{MS} = 1 - \exp^{-6.8(S/S_{max})} \tag{D.3}$$

S = available soil moisture, mm
S_{max} = maximum value of S; 150 mm
P = rainfall rate, mm/day
E = evapotranspiration rate, mm/day
β_{MS} = Mintz and Serafini Beta-function which regulates the evapotranspiration rate
E_p = potential evapotranspiration rate, mm/day.

The expression for β_{MS} was determined by Mintz and Serafini by curve–fit to the data of Nappo (1975) which were based on observations of soil moisture depletion by individual maize plants growing in pots. The potential evapotranspiration rate, E_p, was determined from the method of Thornthwaite (1948) and is principally a function of air temperature, T_a.

To calculate the time–varying fields of soil moisture, monthly mean values of P and T_a were obtained from Jaeger (1976) and the NCAR data archive respectively and were used to integrate Eq. (D.1) for each 4° by 5° grid area using a time step of one day. This procedure was repeated for 7 years of integration after which the difference between the values of S taken on the same calendar day of years 6 and 7 were less than 0.01 mm for every grid area. (The fields were initialized to zero on the first time step). These fields of soil moisture are currently used by the UCLA/GLA model and the GLA 4th–order model. In most GLA and UCLA/GLA GCM applications, the soil moisture fields are not updated prognostically, but from daily interpolations of the time–varying fields calculated by Mintz and Serafini (in preparation).

(ii) Geophysical Fluid Dynamics Laboratory (GFDL)

A similar scheme to that of Mintz and Serafini (in prep.) has been in use at GFDL and at the National Meteorological Center (NMC) for some years; see Gordon, (1986).

A long term integration of the GFDL Zodiac GCM was used to generate fields of S via Eq. (D.1). In this case, the fields of P and E used in (D.1) are produced from the model's own calculations where E is calculated by (D.2) with β_G given by

$$\beta_G = \frac{S}{0.75\ S_{max}} \qquad 0 \le \beta_G \le 1 \tag{D.4}$$

where

β_G = GFDL 'Beta–function'
S_{max} = 150 mm

The potential evaporation rate, E_p, is calculated as follows

$$E_p = \frac{e^*(T_s) - e_r}{r_a} \frac{\rho C_p}{\lambda \gamma} \tau \tag{D.5}$$

E_p = potential evaporation rate, mm/day
T_s = surface temperature, K
$e^*(T_s)$ = saturated vapor pressure of the lowest model layer, mb
r_a = aerodynamic resistance between the surface and the lowest model layer, s/m
ρ, C_p = the density, specific heat of air, kg/m and J/kg/K, respectively
γ = psychrometric constant, mb/K
λ = latent heat of evaporization, J/kg
τ = number of seconds in a day.

The fields generated from the long–term GCM integration have been used as a standard soil moisture initialization for the GFDL model and the NMC medium range forecast (MRF) model.

Recently, Willmott et al. (1985) performed another off–line analysis of the global soil moisture fields in a similar manner to that of Mintz and Serafini (in prep.). These fields (which are based on the β_{MS} function) are currently used in the University of Maryland's Center for Ocean–Land–Atmosphere version of the NMC MRF 86 model (Ctl–GCM) for initialization. For our purposes, however, we treat these fields as if they had been derived by the NMC bucket hydrological model (i.e., the β_G function) as regardless of how the initial fields are derived, they impact the circulation through the hydrological model in place in the GCM.

2. INCOMPATIBILITY OF EXISTING AND SiB MOISTURE CLIMATOLOGIES.

The existing soil moisture initialization fields cannot be used directly by SiB for the following reasons:

(i) The value of S_{max}, the total amount of available soil moisture, is fixed at 150 mm in the Mintz and Serafini and GFDL cases, but is variable in SiB depending on the biome. In SiB, for practical purposes the available soil moisture storage ranges from 60 mm in deserts to 415 mm in forested regions.

(ii) The fractional wetness, $W = S/S_{max}$, as given by the existing fields, cannot be used for initializing SiB because the extremely low values of W predicted by (D.1) and (D.2) are physically unrealistic. Both of the Beta–functions, β_{BS} and β_G, produce excessively high values of E/E_p when $W \leq 0.6$, see Sellers (1987). The main reason for this is that vegetation cannot extract water from the soil when W drops below about 0.3. Most observations and simulations; for example, see Sellers and Dorman (1987), indicate that the evapotranspiration rate of a vegetated surface is largely insensitive to W when W is greater than about 0.6, declines curvilinearly between 0.6 and about 0.3 and is near–zero thereafter.

(iii) The values of E_p as given by (D.4) and (D.5) will generally overestimate the stress–free evapotranspiration rate, see Sellers (1987) and Sellers et al. (1986). This effect is not likely to be so important as (i) and (ii).

In conclusion it would be unwise to use the Mintz–Serafini or the GFDL–generated fields of soil moisture for SiB initialization directly. This applies to both the absolute values, S, and the wetness fraction, W.

3. TRANSFORMING THE EXISTING SOIL MOISTURE FIELDS INTO SiB–COMPATIBLE SOIL MOISTURE FIELDS

The transformation scheme used to generate SiB soil moisture fields is simple, robust and does not require any more data than the existing fields themselves and the SiB parameter set. The scheme is based on two representations of the soil moisture depletion process, one of which is assumed to be effective for near saturated conditions (Sec. 4.1) and the other for very dry conditions (Sec. 4.2). A simple interpolation formula is used to combine the two methods to determine intermediate soil moisture contents (Sec. 4.3).

3.1 Soil moisture depletion under wet conditions

A given grid area is assumed to be saturated at time $t = 0$ and is then exposed to an evaporative demand, E_p. After a specified time T, the grid area would have soil moisture contents of S_{MS} or S_G, if the β_{MS} or β_G functions were applied, and a soil moisture content S_S if SiB were used. The values of S_{MS}, S_G and S_S could be then considered transforms of each other.

The process of integrating (D.1) over time is relatively straightforward. With the full version of SiB, however, the problem is more complex and so the SiB evapo–transpiration formulation had to be considerably simplified so that it could be applied to the existing fields. To this end, the following assumptions were made.

(i) The initial state of the Beta–function soil column is saturation; that is, $S = S_{max}$. The equivalent initial state assumed for the SiB soil column is the moisture content retained against gravitational drainage. This implies a soil moisture potential, ψ, of order –1, from which the appropriate soil moisture content can be estimated from

$$\psi = \psi_s W^{-B} \qquad \text{(D.6)}$$

where

ψ = soil moisture potential (m)
ψ_s = soil moisture potential (m) when $W = 1$
B = empirical coefficient

Both ψ_s and B are dependent on soil type in SiB. For a given SiB biome, (D.6) may be solved for $\psi = -1$ to give an estimate of W_0, the starting value of the SiB soil wetness when $t = 0$.

(ii) The value of E_p used in the Beta–function calculations is taken to be roughly equivalent to the unstressed evapotranspiration rate from the equivalent SiB grid area. This is a less defensible assumption as firstly, the evapotranspiration rate from a SiB grid area is dependent on the vegetation type, and secondly, the value of E_p used in the Beta–function is liable to be an over–estimate, see Sellers (1987).

The SiB calculation of the surface energy balance can now be drastically simplified to yield a formulation similar to a Beta–function. To do this, some further assumptions are made:

(iii) The ground and canopy surface temperatures are equal; $T_c = T_{gs}$

(iv) One vegetation layer is dominant.

(v) The leaf water potential is approximately equal to the soil moisture potential in the root zone, ψ.

(vi) Soil moisture stress, exercised through ψ, is the only significant stress operating on the vegetation's transpiration rate (see, Sellers et al. 1986).

(vii) The surface resistances are large compared to the aerodynamic resistances.

(viii) The air is relatively dry.

Incorporation of these assumptions into the SiB formulation yields

$$E_S \simeq \beta_S \, E_p \tag{D.7}$$

$$\beta_S = Vf(\psi) + (1-V)\, h_s \frac{r_{surf_o}}{r_{surf}} \tag{D.8}$$

E_S = SiB–derived evapotranspiration rate, mm/day

β_S = SiB–based Beta function

V = dominant vegetation layer cover fraction

h_s = soil air humidity, kg/kg.

r_{surf_o} = Soil surface resistance at saturation, s/m.

r_{surf} = Soil surface resistance, s/m

$f(\psi)$ = leaf water potential stress factor.

The leaf water potential stress factor, $f(\psi)$, is given by

$$f(\psi) = \frac{\psi-\psi_2}{\psi_1-\psi_2} \tag{D.9}$$

ψ_1, ψ_2 = leaf water potentials at which the stomata start to close and are completely closed, respectively, m.

$$0 < f(\psi) < 1$$

Where ψ is calculated from the empirical formulation of Clapp and Hornberger (1978), see Eq. (D.6).

The process of transforming the Beta–function fields is now fairly straightforward. The link between the Beta–function and SiB soil moisture contents is specified by the time, T, that each grid area is exposed to the same evaporative demand, E_p. To do this, the precipitation rate in (D.1) is ignored which yields

$$\frac{dS}{dt} = -\beta E_p \tag{D.10}$$

and

$$\int_{S_o}^{S_{MS,G,S}} \frac{dS}{\beta_{MS,G,S}} = -E_p \int_o^T dt \tag{D.11}$$

where

S_o = starting soil moisture content, mm

= S_{max} for Beta–function calculations, mm

= $\left[\frac{\psi_2}{-1}\right]^{1/B}$ for SiB calculations, mm

S = Soil moisture after time T, mm, where subscript refers to MS,G or SiB

The SiB transform of the Mintz–Serafini or GFDL soil moisture fields is simply achieved by assuming E_p is the same in both cases so that

$$\int_{S_o}^{S_{MS,G}} \frac{dS}{\beta_{MS,G}} = \int_{S_o}^{S_S} \frac{dS}{\beta_S} \tag{D.12}$$

In (D.12), the fields of $S_{MS,G}$ and S_o are known and the functions β_{MS}, β_G and β_S have been specified in (D.3), (D.4), and (D.7) respectively. (D.12) can therefore be solved quite easily for S_S, the SiB soil moisture value. The left hand side of (D.12) is solved analytically to yield:

$$\int_{S_o}^{S_{MS}} \frac{dS}{\beta_{MS}} = \frac{S_{max}}{6.8} \ln \left[\frac{e^{6.8 S_{MS}/S_{max}} - 1}{e^{6.8} - 1} \right] \tag{D.13}$$

and,

$$\int_{S_o}^{S_G} \frac{dS}{\beta_G} = 0.75 S_{max} \ln \left[\frac{0.75 S_{max}}{S_G} \right] + 0.25 S_{max}, \quad S_G < 0.75 S_{max}$$

$$= S_{max} - S_G \qquad S_G > 0.75 S_{max} \tag{D.14}$$

The integration of the right hand side of (D.12) is performed numerically to create a look–up table for each SiB biome. In the WETNESS program, soil moisture values from existing data sets are used to determine the left hand side of (D.12) for each grid area, using (D.13) and (D.14), and these are then used to obtain the corresponding values of S_S from the look up table.

3.2 Soil moisture depletion under dry conditions.

In dry areas, it is assumed that the soil moisture content has reached a quasi–equilibrium state which is characterized by the value of the Beta–function, β_{MS} or β_G. Under these conditions the soil moisture content for SiB, S_D, is determined from the matching SiB soil moisture availability value as given by (D.6).

$$S_D = S_{max} \left[\frac{\psi_s}{\psi} \right]^{1/B} \tag{D.15}$$

where ψ is determined from the solution of

$$\beta_S = \beta_{MS,G} \tag{D.16}$$

3.3 Interpolation of SiB soil moisture values for all wetness conditions.

It is assumed that the methods outlined in Secs. 4.1 and 4.2 are appropriate to wet and dry conditions respectively. A single value of $S_{S_{iB}}$ is calculated simply by taking the minimum of S_S and S_D.

$$S_{S_{iB}} = \text{Min}\,(S_S, S_D) \qquad \text{(D.17)}$$

4. SUMMARY

The method discussed above has a number of obvious shortcomings. It does serve, however, to give SiB–compatible soil moisture fields that will approximately reflect the evapotranspiration climatology of the region. The major features of the results from the procedure are as follows:

(i) In mid–latitude zones where SiB has deep soils, the method will yield relatively high values of wetness fraction for SiB. This is because the soil moisture deficit given by (D.12) is calculated in absolute terms.

(ii) Where the existing climatologies give very low values, i.e., $W \leq 0.1$, SiB will yield values of the order of $W = 0.25$, which is equivalent to unavailable soil moisture.

(iii) The maximum value of the initial SiB wetness fraction will be about $W = 0.80$.

All of the simplifications used to calculate the SiB fields ensure that a fairly high degree of uncertainty exists in these values. When a long integration with SiB is executed, the resultant fields of soil moisture will be used for future initializations.

APPENDIX E

INITIALIZATION OF SOIL TEMPERATURE

We have adopted a simple soil temperature initialization scheme for Ctl–GCM: the mean annual air surface temperature is used as the soil temperature at 500 cm depth, T_{g3}, the energy balance equation was then solved to obtain the ground surface temperatures for midday and night–time radiation conditions. These two surface temperatures were averaged to give the initial ground surface temperature, T_s. The deep soil temperatures T_{g1} and T_{g2} (at 10 cm and 50 cm respectively) were initialized as follows

$$T_{g1} = 0.99\ T_s + 0.01\ T_{g3} \qquad (E.1)$$
$$T_{g2} = 0.9\ T_s + 0.1\ T_{g3}$$

In SiB–GCM, T_{g3} was used as the initial estimate of deep soil temperature, T_d. SiB was then integrated for five time steps with noon time and zero solar radiation conditions while the atmospheric temperature and specific humidity were held constant. These two ground surface temperatures were averaged to give the initial surface temperature T_s. The deep soil temperature T_d was initialized as follows

$$T_d = 0.9\ T_s + 0.1\ T_{g3} \qquad (E.2)$$

As discussed in Sec. 4, this soil temperature initialization was found to be satisfactory and heat conduction in the soil was generally an insignificant part of the time–averaged surface energy balance.

ACKNOWLEDGEMENTS

The first author is grateful to the Japan Meteorological Agency and to the Center for Ocean–Land–Atmosphere Interactions (University of Maryland) for facilitating his visit to the University of Maryland. Thanks are also extended to Dr. Harshvardhan and Mr. Tom Corsetti for help with some of the radiation code, and to Jeff Dorman and Larry Marx for organizing the SiB vegetation parameter sets. Dr. Jim Shuttleworth provided the Amazon data sets which were used for comparisons with the 'point' flux estimates for Manaus, Amazonas in Secion 4. This research was supported by NSF grant ATM–8414660, NASA grants NAG5–492 and NAGW–557. Special thanks go to Marlene Schlichtig for typing and proofreading several drafts of the manuscript.

REFERENCES

Blake, D. W., T. N. Krishnamurti, S. V. Low–Nam and J. S. Fein, 1983: Heat low over the Saudi Arabian desert during may 1979 (Summer MONEX), *Mon. Wea. Rev.*, **111**, 1759–1774.

Budyko, M. I., 1974: ***Climate and Life***, Academic Press, N.Y., N.Y., USA, pp. 508.

Carson, D. J., 1981: Current parameterizations of land surface processes in atmospheric General Circulation Models. ***Proc. JSC Study Conference on Land–Surface Processes in Atmosphere General Circulation Models***, P. S. Eagleson, Ed., Cambridge University Press, 67–108.

Carson, D. J. and A. B. Sangster, 1981: The influence of land–surface albedo and soil moisture on general circulation model simulations. *Numerical Experimentation Programme Report*, **No. 2**, pp. 5.14–5.21.

Charney, J. G., W. J. Quirks, S. H. Chow and J. Kornfield, 1977: A comparative study of the effects of albedo change on drought in semi–arid regions. *J. Atmos. Sci.*, **34**, 1366–1385.

Chervin, R. M., 1979: Response of the NCAR general circulation model to changed land surface albedo. *Report of the JOC Study Conference on Climate Models: Performance, intercomparison and sensitivity studies*, **Vol., I**, pp. 563–581.

Clapp, R. B. and G. M. Hornberger, 1978: Empirical equations for some soil hydraulic properties. *Water Resour. Res.*, **14.4**, 601–604.

Davies, R., 1982: Documentation of the Solar Radiation Parameterization in the GLAS Climate Model. ***NASA Technical Memorandum 83961***, pp. 57.

Deardorff, J. W., 1972: Parameterization of the planetary boundary layer for use in General Circulation Models. *Mon. Wea Rev.*, **100**, 93–106.

Deardorff, J. W., 1977: Efficient prediction of ground surface temperature and moisture with inclusion of a layer of vegetation. *J. Geophys. Res.*, **83**, 1889–1903.

Dickinson, R. E., 1984: Modeling evapotranspiration for three–dimensional global climate models. Climate Processes and Climate Sensitivity. J. E. Hanson and T. Takahashi, Eds., American Geophysical Union. *Geophysical Monograph*, **29**, 58–72.

Dickinson, R. E. and A. Henderson–Sellers, 1988: Modelling tropical deforestation: A study of GCM land–surface parameterizations. *Quart. J. Roy. Meteor. Soc.*, **114**, 439–462.

Dorman, J. L. and P. J. Sellers, 1989: A global climatology of albedo, roughness length and stomatal resistance for atmospheric general circulation models as represented by the Simple Biosphere model (SiB). *J. Appl. Met.*, in press.

Esbensen, S. K. and Y. Kushnir, 1981: *The heat budget of the global ocean: An atlas based on estimates from surface marine observations.* Climate Research Institution, **Report No. 29**, Oregon State University, Corvallis, OR. 27 pp., 188 figures.

Farquhar, G. D. and T. D. Sharkey, 1982: Stomatal conductance and photosynthesis. *Ann. Rev. Pl. Physiol.*, **33**, 317–345.

Fels, S. B. and M. D. Schwarzkopf, 1975: The simplified exchange approximation: A new method for radiative transfer calculations. *J. Atmos. Sci.*, **32**, 1475–1488.

Franken, W., P. R. Leopoldo, E. Matsui, M. N. G. Ribeiro, 1982: Interceptacao das precipitacoes em floresta Amazonica de terra firme. *Acta Amazon*, **12**, 15–22.

Gordon, C. t., 1986: Boundary layer parameterizations and land surface processes in GFDL GCMs. *ISLSCP, Proceedings of an International Conference* **ESA SP–248, *ESA, PARIS, FRANCE, P. 29–37.***

Harshvardhan and T. G. Corsetti, 1984: Longwave radiation Parameterization for the UCLA/GLAS GCM. ***NASA Technical Memorandum 86072***, pp 65.

Hellerman, S. and M. Rosenstein, 1983: Normal monthly wind stress over the world ocean with error estimates. *J. Phys. Oceanogr.*, **13**, 1093–1104.

Jaeger, L., 1976: Monatskarten des Niederschlages fur die ganze Erde. *Berichte Deutscher Wetterdienst*, **18, Nr 139**, Offenbach, Germany.

Kinter III, J. L., J. Shukla, L. Marx and E. K. Schneider, 1988: A simulation of the winter and summer circulations with the NMC global spectral model. *J. Atmos. Sci.*, **45**, 2486–2522.

Kousky, V. E., 1980: Diurnal rainfall variations in Northeast Brazil. *Mon. Wea. Rev./*, **108**, 488–498.

Kuo, H. L., 1965: On the formation and intensification of tropical cyclones through latent heat release by cumulus convection. *J. Atmos. Sci.*, **22**, 40–63.

Lacis, A. A. and J. E. Hansen, 1974: A parameterization for the absorption of solar radiation in the earth's atmosphere. *J. Atmos. Sci.*, **31**, 118–133.

Luxmoore, R. J., 1983: Water budget of an eastern deciduous forest stand. *Soil Sci. Soc. Am. J.*, **47**, 785–791.

Manabe, S., 1969: The atmospheric circulation and hydrology of the Earth's surface. *Mon. Wea. Rev.*, **97**, 739–774.

Martin, C. L., D. Fitzjarrald, M. Garstang, A. P. Oliveira, S. Greco and E. Browell, 1988: Structure and growth of the mixing layer over the Amazonian rain forest, *J. Geophys. Res.*, (D2), 1361–1377.

Matthews, E., 1984: Global vegetation and land use: New high–resolution data bases for climate studies. *J. Clim. Appl. Met.*, **22**, 474–487.

McNaughton, K. G. and T. A. Black, 1973: A study of evapotranspiration from a Douglas fir forest using the energy balance approach. *Water Resour. Res.*, **9**, 1579–1590.

Mellor, G. L. and T. Yamada, 1982: Development of a turbulence closure model for geophysical fluid problems. *Rev. Geophys. Space Phys.*, **20**, 851–875.

Mintz, Y., 1984: The sensitivity of numerically simulated climates to land–surface conditions. ***The Global Climate***. J. Houghton, Ed., Cambridge University Press, 79–105.

Mintz, Y. and Y. Serafina (in prep.): global fields of monthly normal soil moisture, as derived from observed precipitation and an estimated potential evapotranspiration. Working draft, Goddard Laboratory of Atmospheres, NASA/GSFC, Greenbelt, Maryland, 20771. 10 pages and figures.

Miyakoda, K. and J. Sirutis, 1977: Comparative integrations of global spectral models with various parameterized processes of subgrid scale vertical transports. *Beitrage Phys. Atmos.*, **50**, 445–447.

Miyakoda, K. and J. Sirutis, 1986: Manual of E–physics. Manuscript, GFDL, Princeton, New Jersey.

Monteith, J. L., 1973: ***Principles of Environmental Physics***. Edward Arnold, Eds., London, pp. 242.

Oltman, R. E., H. O. R. Sternbert, F. C. Ames and L. C. Davis, Jr., 1964: Amazon river investigations reconnaissance measurements of July. *U.S. Geol. Surv. Circ.*, **486**, pp. 15.

Posey, J. W. and P. F. Clapp, 1964: Global distribution of normal surface albedo. *Geophisica International*, **4**, 33–48.

Randall, D. A., J. A. Abeles and T. G. Corsetti, 1985: Seasonal simulation of the planetary boundary layers and boundary–layer stratocumulus clouds with a general circulation model. *J. Atmos. Sci.*, **42**, 641–676.

Rasmusson, E. M., 1968: Atmospheric water vapour transport and the water balance of North America. Part II: Large–scale water balance investigations. *Mon. Wea. Rev.*, **96**, 720–734.

Rowntree, P. R., 1984: Review of general circulation models as a basis for predicting the effects of vegetation change on climate. *Proceedings of the U.N.U. Workshop on **Forests, Climate, and Hydrology – Regional Impacts.*** Oxford University Press, Oxford, March 1984.

Ruprecht, E. and W. M. Gray, 1976: Analysis of satellite–observed tropical cloud clusters II thermal moisture and precipitation fields. *Tellus*, **28**, 414–426.

Salati, E., 1987: The forest and the hydrological cycle. ***The Geophysiology of Amazonia.*** Eds: R. E. Dickinson, Wiley and Sons, New York, 273–296.

Sato, N., P. J. Sellers, D. A. Randall, E. K. Schneider, J. Shukla, J. L. Kinter III, Y.–T. Hou and E. Albertazzi, 1989: Implementing the Simple Biosphere Model (SiB) in a general circulation model: Methodology and Results. *NASA Contractor Report*, NASA HQ, Independence Ave., Washington, D. C. 20546, pp. 70 plus references and 27 figures.

Sela, J. G., 1980: Spectral modeling at the National Meteorological Center. *Mon. Wea. Rev.*, **108**, 1279–1292

Sellers, P. J., 1985: Canopy reflectance, photosynthesis and transpiration. *Intl. J. Rem. Sens.*, **6**, 1335–1372.

Sellers, P. J., Y. Mintz, Y. C. Sud and A. Dalcher, 1986: A simple biosphere model (SiB) for use within general circulation models. *J. Atmos. Sci.*, **43**, 505–531.

Sellers, P. J., 1987: Modeling effects of vegetation on climate. ***The Geophysiology of Amazonia.*** Eds: R. E. Dickinson, Wiley and Sons, New York, **Chapter 16**, 244–264.

Sellers, P. J. and J. L. Dorman, 1987: Testing the Simple Biosphere model (SiB) with point micrometeorological and biophysical data. *J. Clim. Appl. Met*, **26 (5)**,622–651

Sellers, W. D., 1965: ***Physical Climatology.*** The University of Chicago Press, Chicago, Illinois, USA pp. 271.

Shukla, J. and Y. Mintz, 1982: Influence of land–surface evapotranspiration on the earth's climate. *Science*, **215**, 1498–1501.

Shuttleworth, W. J., J. H. C. Gash, C. R. Lloyd, C. J. Moore, J. Roberts, A. O. Marques Filho, G. Fisch, V. P. Silva Filho, M. N. G. Ribeiro, L. C. B. Molion, L. A. De Sa, J. C. A. Nobre, O. M. R. Cabral, S. R. Patel and J. C. De Moraes, 1984a: Eddy correlation measurements of energy partition for Amazonian forest. *Quart. J. Roy. Meteor. Soc.*, **110**, 1143–1163.

Shuttleworth, W. J., J. H. C. Gash, C. R. Lloyd, C. J. Moore, J. Roberts, A. O. Marques Filho, G. Fisch, V. P. Silva Filho, M. N. G. Ribeiro, L. C. B. Molion, L. A. De Sa, J. C. A. Nobre, O. M. R. Cabral, S. R. Patel and J. C. De Moraes, 1984b: Observation of radiation exchange above and below Amazonian forest. *Quart. J. Roy. Meteor. Soc.*, **110**, 1163–1169.

Sud, Y. C. and M. J. Fennessy, 1982: A study of the influence of surface albedo on July circulation in semi–arid regions using the GLAS GCM. *J. Climatology*, **2**, 105–125.

Sud, Y. C. and W. E. Smith, 1985: The influence of surface roughness of deserts on the July circulation. *Bound.–Layer Met.*, **33**, 15–40.

Swift, Jr., L. W. and W. T. Swank, 1975: Simulation of evapotranspiration and drainage from mature and clear–cut deciduous forests and young pine plantation. *Water Resour. Res.*, **11**, 667–673.

Tenhunen, J. D., O. L. Large, J. Gerbel, W. Beyschlag and J. A. Weber, 1984: changes in photosynthetic capacity, carboxylation efficiency, and CO_2 compensation point associated with midday stomatal closure and midday depression of net CO_2 exchange of leaves of Querus suber. *PLANTA*, **162**, 193–203.

Tiedtke, M., 1984: The effect of penetrative cumulus convection on the large–scale flow in a general circulation model. *Beitr. Phys. Atmos.*, **57**, 216–239.

Thornthwaite, C. W., 1948: An approach toward a rational classification of climate. *Geographical Review*, **38**, 55–94.

van der Ploeg, R. R., G. Tassone and J. von Hoyningen–Heune, 1980: ***The Joint Measuring Campaign 1979 in Ruthe (West Germany) – Description of Preliminary data.*** European Econ. Comm., Joint Res. Cent., Ispra, Italy.

Walker, J. M. and P. R., Rowntree, 1977: The effect of soil moisture on circulation and rainfall in a tropical model. *Quart. J. Roy. Meteor. Soc.*, **103**, pp. 29–46.

Warrilow, D. A., 1986: ***The sensitivity of the UK Meteorological Office atmospheric general circulation model to recent changes in the parameterization of hydrology.*** ISLSCP, Proceedings of an International Conference. **ESA SP–248**, ESA, Paris, France, 143–150.

Willmott, C. J., C. M. Rowe and Y. Mintz, 1985: Climatology of the terrestrial seasonal water cycle. *J. Climatology*, **5**, 589–606.

Yamagishi, Y., 1980: Simulation of the air mass transformation process using a numerical model with detailed boundary layer parameterization. *J. Meteor. Soc. Japan*, **58**, 357–377.

NASA
National Aeronautics and Space Administration

Report Documentation Page

1. Report No.	2. Government Accession No.	3. Recipient's Catalog No.
NASA CR-185509		

4. Title and Subtitle

Implementing the Simple Biosphere Model (SiB) in a General Circulation Model: Methodologies and Results

5. Report Date

August 1989

6. Performing Organization Code

7. Author(s)

N. Sato, P. J. Sellers, D. A. Randall, E. K. Schneider, J. Shukla, J. L. Kinter III, Y.-T. Hou, and E. Albertazzi

8. Performing Organization Report No.

10. Work Unit No.

9. Performing Organization Name and Address

Center for Ocean-Land-Atmosphere Interactions
Department of Metephology
University of Maryland
College Park, MD 20742

11. Contract or Grant No.

NAGW-492 and NAGW-557

12. Sponsoring Agency Name and Address

National Aeronautics and Space Administration
Washington, DC 20546

13. Type of Report and Period Covered

Contractor Report

14. Sponsoring Agency Code

EEL

15. Supplementary Notes

Technical Monitor: G. Asrar
Code EEL, NASA Headquarters
Washington, DC 20546

16. Abstract

The Simple Biosphere Model (SiB)of Sellers et al (1986) was designed to simulate the interactions between the Earth's land surface and the atmosphere by treating the vegetation explicitly and realistically, thereby incorporating biophysical controls on the exchanges of radiation, momentum, sensible and latent heat between the two systems. This paper describes the steps taken to implement SiB in a modified version of the National Meteorological Center's spectral GCM. The coupled model (SiB-GCM) was used with a conventional hydrological model (Ctl-GCM) to produce summer and winter simulations. The same GCM was used with a conventional hydrological model (Ctl-GCM) to produce comparable 'control' summer and winter variations.

It was found that SiB-GCM produced a more realistic partitioning of energy at the land surface than Ctl-GCM. Generally, SiB-GCM produced more sensible heat flux and less latent heat flux over vegetated land than did Ctl-GCM and this resulted in the development of a much deeper daytime planetary boundary and reduced precipitation rates over the continents in SiB-GCM. In the summer simulation, the 200 mb jet stream and the wind speed at 850 mb were slightly weakened in the SiB-GCM relative to the Ctl-GCM results and equivalent analyses made from observations.

17. Key Words (Suggested by Author(s))	18. Distribution Statement
General Circulation Model (GCM) Biosphere-Atmosphere Interaction Planetary Boundary Layer (PBL)	Unclassified - Unlimited Subject Category 46

19. Security Classif. (of this report)	20. Security Classif. (of this page)	21. No. of pages	22. Price
Unclassified	Unclassified	76	A05

NASA FORM 1626 OCT 86

For sale by the National Technical Information Service, Springfield, VA 22161

NASA-Langley, 1989